arXiv:cond-mat/0409626v2 [cond-mat.mes-hall] 12 Nov 2004

Theory of solid state quantum information processing

Guido Burkard

IBM T. J. Watson Research Center, P. O. Box 218, Yorktown Heights, NY 10598, USA

Recent theoretical work on solid-state proposals for the implementation of quantum computation and quantum information processing is reviewed. The differences and similarities between microscopic and macroscopic qubits are highlighted and exemplified by the spin qubit proposal on one side and the superconducting qubits on the other. Before explaining the spin and supercondcuting qubits in detail, some general concepts that are relevant for both types of solid-state qubits are reviewed. The controlled production of entanglement in solid-state devices, the transport of carriers of entanglement, and entanglement detection will be discussed in the final part of this review.

Contents

I. Introduction 2
- A. What actually has to be achieved? DiVincenzo's criteria 3
  - 1. A scalable physical system with well characterized qubits 3
  - 2. The ability to initialize the state of the qubits 3
  - 3. Long relevant decoherence times, much longer than the gate operation times 3
  - 4. A universal set of quantum gates 4
  - 5. The ability to measure specific single qubits 4
- B. Microscopic vs. macroscopic solid-state qubits 5
- C. Scope of this review article 5

II. General concepts 5
- A. The Loss-DiVincenzo proposal 5
- B. QC with anisotropic couplings 6
  - 1. Ising and transverse (XY) coupling 6
  - 2. Anisotropy due to the spin-orbit coupling 7
- C. Universal QC with the exchange coupling 9
  - 1. Encoding 9
  - 2. One-qubit gates 10
  - 3. Two-qubit gates 10
  - 4. Protection against errors 11
  - 5. Related ideas 11
- D. Optimization of quantum circuits 11
  - 1. Serial pulse mode 12
  - 2. Parallel pulse mode 12
  - 3. Anisotropic systems 13
- E. Adiabaticity 13

III. Electron spins 14
- A. Quantum Dots 14
- B. Exchange in laterally coupled QDs 15
  - 1. The Heitler-London approach 16
  - 2. Limitations and extensions of HL 17
  - 3. The Hund-Mulliken approach and the Hubbard Limit 17
  - 4. Numerical work 18
  - 5. Measurements of QD exchange 19
- C. Exchange in vertically coupled QDs 19
  - 1. Perpendicular Magnetic Field $B_\perp$ 20
  - 2. In-plane magnetic field $B_\parallel$ 21
  - 3. Electrical switching of the interaction 22
- D. Single-qubit operations 22
- E. Semiconductor microcavities 24
  - 1. Single-qubit operations 24
  - 2. Two-qubit operations 24
  - 3. Measurement 26
  - 4. Related proposals 26
- F. Decoherence 26
  - 1. Phonons and the spin-orbit coupling 26
  - 2. Nuclear spins 27

IV. Superconducting micro-circuits 27
A. Overview 27
B. Decoherence, visibility, and leakage 28
1. Decoherence 28
2. Visibility 28
3. Leakage 29
C. Circuit theory 29
D. Flux qubits 29
1. The network graph 30
2. The tree of the network graph 30
3. The loop matrices 30
4. Current-voltage relations (CVRs) 31
5. The Hamiltonian 31
6. Leakage 33
7. The Delft qubit 33
E. Charge qubits 35
1. Graph theory 35
2. Single charge box 36
3. Flux-controlled Josephson junction 37
4. Inductively coupled charge boxes 38
F. Multiple sources of decoherence 39
1. Dissipative dynamics 39
2. Mixing Terms 40

V. Entanglement 42
A. Production of entangled electrons 42
1. Superconductor-normal junctions 42
2. Superconductor–Luttinger liquid junctions 43
3. Transport through quantum dots 44
4. Coulomb scattering in a 2D electron system 44
5. Entangled Electrons in a Fermi Sea 44
B. Detection of spin entanglement 46
1. Coupled quantum dots 46
2. Coupled dots with SC leads 47
3. Beam splitter shot noise 47
4. Lower bounds for entanglement 49
5. Proposed tests of Bell's inequalities 50
C. Production of entangled photons 51

References 53

I. INTRODUCTION

The capabilities of information processing devices are derived from their physical properties; in Landauer's words, "Information is physical" (Landauer, 1991). The pioneers of quantum information processing recognized that if a device was quantum mechanical, then it could have computational powers exceeding those of a classical machine. A sign for the superiority of quantum hardware is that typical simulations of quantum systems on classical computers appear to be computationally hard.

This article is intended to give an overview of the theory of solid-state quantum information processing. For a general introduction to quantum computation (QC) and quantum information, we refer the reader to (Nielsen and Chuang, 2000). Although the distinction between different quantum devices is probably less fundamental than that between quantum and classical devices, Landauer's motto can also be applied here. In other words, the specific physical properties of the quantum hardware *do* matter. Two rather different categories of this hardware are those involving atomic systems, e.g.,

- atoms in an ion trap,
- atoms in an optical lattice,
- ensemble of nuclear spins in a liquid,

and those involving solid-state systems, e.g.,

- spins of electrons in semiconductor quantum dots,
- nuclear spins of donor atoms in a semiconductor,

- superconducting microcircuits containing Josephson junctions.

This list is by no means complete; an informative collection of various proposals can be found in (Braunstein and Lo, 2000). While there have so far been more successful demonstrations involving atomic systems in the laboratory, many solid-state systems are scalable, i.e., one can fabricate systems with many quantum bits (qubits) using essentially the same fabrication technique that is proposed or used for a single qubit.

A. What actually has to be achieved? DiVincenzo's criteria

For the following discussion of attempts to implement a quantum computer (or parts of it) in solid-state systems, it may be useful to review what actually has to be achieved. An excellent summary of the criteria for the physical implementation of quantum computation are DiVincenzo's following "five requirements" (DiVincenzo, 1997, 2000).

1. A scalable physical system with well characterized qubits

A quantum bit, or qubit, is a suitable quantum-mechanical two-state system (see item I.A.3 for more about what it means for the qubit to be quantum mechanical). A pure state of the two-state system then takes the form

$$|\psi\rangle = \alpha|0\rangle + \beta|1\rangle, \tag{1}$$

where the amplitudes α and β are complex numbers such that $|\alpha|^2 + |\beta|^2 = 1$. The states $|0\rangle$ and $|1\rangle$ form an orthonormal basis of the Hilbert space $\mathcal{H}_2 = \mathrm{span}\{|0\rangle, |1\rangle\}$ of the qubit. A good example of a quantum two-state system is the spin 1/2 of an electron, where $|\uparrow\rangle \equiv |0\rangle$ and $|\downarrow\rangle \equiv |1\rangle$. The Hilbert space of the entire system then needs to be a tensor product of a large number n of such two-state systems,

$$\mathcal{H} = \mathcal{H}_2^{\otimes n} = \underbrace{\mathcal{H}_2 \otimes \mathcal{H}_2 \otimes \cdots \otimes \mathcal{H}_2}_{n\,\text{factors}}. \tag{2}$$

An excellent tutorial on the physical meaning of the tensor product in Eq. (2) and the difference between classical and quantum bits can be found in (Mermin, 2003). A system is *scalable* if it can be realized (in principle) for arbitrary n. Some early atomic qubit realizations are not (easily) scalable, and one of the biggest motivations for studying solid-state qubits is the hope that they will be scalable like conventional solid-state integrated circuits. A collection of identical particles, e.g., the Fermi sea of electrons in a metal, typically does not represent a set of *well characterized* qubits. The qubits need to be "labeled" in order to make them distinguishable, e.g., in an arrangement where single electrons sit on localized sites (quantum dots, donor levels of impurity atoms) and can be addressed, e.g., as "spin of the i-th dot".

2. The ability to initialize the state of the qubits

Before a quantum computation is started, a fresh register of qubits, e.g., in the state

$$|\psi\rangle = |0\rangle^{\otimes n} = \underbrace{|0\rangle \otimes |0\rangle \otimes \cdots \otimes |0\rangle}_{n\,\text{factors}}, \tag{3}$$

is required. This requirement looks more innocent than it actually is, since it is not always easy to create such low-entropy states, e.g., if the temperature is not sufficiently low. Suppling a quantum computer with fresh "zeros" is also essential for quantum error correction, where the entropy that accumulates due to decoherence is pumped out of the quantum memory (Nielsen and Chuang, 2000). For this purpose, it also matters *how fast* the fresh "zeros" can be supplied.

3. Long relevant decoherence times, much longer than the gate operation times

A decoherence time characterizes how long it takes until the quantum phase coherence of a system (e.g., a qubit) is lost due to its interaction with the environment. Frequently used figures of merit are the so-called energy-relaxation time T_1 and the decoherence time T_2 of a single qubit (the notation originates from the NMR literature). To illustrate the meaning of these two quantities, let us assume for the moment that $T_1 \gg T_2$ (this need not be the case; T_1 and T_2

can also be of the same order of magnitude). A pure state of a qubit, Eq. (1), has degraded to an incoherent mixture after a time of the order of T_2, described by the density matrix

$$\rho = |\alpha|^2|0\rangle\langle 0| + |\beta|^2|1\rangle\langle 1|. \tag{4}$$

An elementary introduction into the meaning of the density operator ρ can be found in quantum mechanics textbooks or in (Nielsen and Chuang, 2000). Note that, in the case where $|0\rangle$ and $|1\rangle$ are eigenstates with different energies, the processes involved in the decoherence of the qubit so far did not involve any energy exchange with the environment. Nevertheless, this loss of the phase information is sufficient to disrupt a quantum computation. After a time of the order of T_1, energy relaxation has taken place and the system is in the thermal equilibrium state $\rho = Z^{-1}\exp(-H/k_BT)$, with the partition sum $Z = \mathrm{Tr}\exp(-H/k_BT)$, the qubit Hamiltonian H, the temperature T, and Boltzmann's constant k_B. The requirement for quantum computation is that $T_2 \gg T_{\mathrm{op}}$ where T_{op} denotes the time to perform a typical operation from the universal set (see Eq. (6) below). In order to achieve quantum computations of arbitrary length with the help of quantum error correction, it is required that the error probability per gate $\epsilon \approx T_{\mathrm{op}}/T_2$ is below its threshold value $\epsilon_{\mathrm{thres}}$ for fault-tolerant quantum computation (Nielsen and Chuang, 2000). The number $\epsilon_{\mathrm{thres}}$ depends on the error-correcting codes used and the type of errors they have to protect against.

4. A universal set of quantum gates

It is required that there is a set $\mathcal{S}$ of unitary operators, called *gates* or *quantum gates*, operating on a bounded number of qubits at a time, from which all unitary operators U on any number of qubits can be composed by applying them in series,

$$U = U_k U_{k-1} \cdots U_2 U_1, \tag{5}$$

where $U_i \in \mathcal{S}$. It has been shown that there are universal sets consisting of quantum gates that operate only on one or two qubits (DiVincenzo, 1995), e.g., the union of one suitable two-qubit gate $U_{(2)}$ with the set of all operations on a single qubit,

$$\mathcal{S} = \{U_{(2)}\} \cup SU(2). \tag{6}$$

Examples of suitable two-quits gates $U_{(2)}$ are the CNOT gate, also known as quantum-XOR or simply XOR (Barenco *et al.*, 1995a), with the following matrix representation in $\mathcal{H}_2 \otimes \mathcal{H}_2$,

$$U_{XOR} = \begin{pmatrix} 1 & 0 & 0 & 0 \\ 0 & 1 & 0 & 0 \\ 0 & 0 & 0 & 1 \\ 0 & 0 & 1 & 0 \end{pmatrix}, \tag{7}$$

or the square-root of SWAP (Loss and DiVincenzo, 1998),

$$S = \begin{pmatrix} 1 & 0 & 0 & 0 \\ 0 & \frac{1-i}{2} & \frac{1+i}{2} & 0 \\ 0 & \frac{1+i}{2} & \frac{1-i}{2} & 0 \\ 0 & 0 & 0 & 1 \end{pmatrix}. \tag{8}$$

It should be added here that there are ways of achieving unitary gates by performing non-unitary operations on a larger Hilbert space. There have been several proposals for doing universal quantum computation by performing von Neumann measurements on a subset of the qubits of a large entangled state or cluster state (Leung, 2004; Nielsen, 2003; Raussendorf and Briegel, 2001). Another example where measurements are used to generate unitary gates is that of free-electron quantum computation (Beenakker *et al.*, 2004).

5. The ability to measure specific single qubits

At the end of a computation, the qubits (or, at least, a subset of them) need to be measured individually in some fixed basis, e.g., the computational basis given by the states $|0\rangle$ and $|1\rangle$. The observable that is measured in this procedure is the Pauli matrix

$$\sigma_z = \begin{pmatrix} 1 & 0 \\ 0 & -1 \end{pmatrix}. \tag{9}$$

B. Microscopic vs. macroscopic solid-state qubits

The existing and proposed solid-state qubits can roughly be grouped into two categories. The qubits of the first category, which we will label *microscopic*, are similar to the atomic qubits in the sense that they are based on quantum objects on the atomic scale whose states $|0\rangle$ and $|1\rangle$ are distinguishable only by measuring a microscopic observable, such as an angular momentum on the order of Planck's constant $\hbar$ or a magnetic dipole moment of the order of one Bohr magneton, μ_B. Electron and nuclear spin qubits, as well as the orbital state of an electron in a semiconductor quantum dot, fall under this category. The second category of qubits we call *macroscopic*, for their distinguishability under measurement of a macroscopic observable, such as a current carried by a large number of electrons, the magnetic field induced by such a current, or the position of an electron charge in a system with two macroscopically distinguishable sites. The typical examples in this category are the superconducting qubits (with exceptions).

C. Scope of this review article

This is not intended to be a comprehensive review of all theoretical work that has been done in the field of solid-state quantum computation. Besides the discussion of some general concepts that apply for a broad range of possible implementations in Sec. II, we concentrate on qubits based on the electron spin (Sec. III) in semiconductor structures (quantum dots) and on superconducting circuits (Sec. IV), representing an example of a microscopic and a macroscopic qubit.

Other solid-state proposals for quantum computation include quantum Hall systems (Privman *et al.*, 1998; Yang *et al.*, 2002), anyons in fractional quantum Hall systems (Kitaev, 2003), the nuclear spin of donors in a semiconductor (Kane, 1998), electron charge degrees of freedom in quantum dots (Barenco *et al.*, 1995b; Brum and Hawrylak, 1997; Landauer, 1996; Tanamoto, 2000; Zanardi and Rossi, 1998), "flying" electron spin qubits in surface acoustic waves (Barnes *et al.*, 2000) or ballistic quantum wires (Popescu and Ionicioiu, 2004), ferroelectrically coupled quantum dots (Levy, 2001), excitons (Biolatti *et al.*, 2000; Chen *et al.*, 2001; Troiani *et al.*, 2000), SiGe quantum dots (Vrijen *et al.*, 2000), paramagnetic impurities in semiconductor quantum wells (Bao *et al.*, 2003), Si-based solid-state NMR (Ladd *et al.*, 2002), and electrons on the surface of liquid He (Platzman and Dykman, 1999).

II. GENERAL CONCEPTS

A. The Loss-DiVincenzo proposal

The underlying idea of this proposal is that the spins of single electrons confined in semiconductor quantum dots (e.g., in a two-dimensional semiconductor heterostructure) are to be used as qubits (Loss and DiVincenzo, 1998). The required coupling between the qubits in this case is provided by the tunneling between adjacent quantum dots, giving rise to a nearest-neighbor exchange coupling. The resulting spin Hamiltonian is that of the Heisenberg model,

$$H(t) = \sum_{\langle i,j \rangle} J_{ij}(t) \mathbf{S}_i \cdot \mathbf{S}_j + \mu_B \sum_i g_i \mathbf{B}(\mathbf{r}_i) \cdot \mathbf{S}_i, \tag{10}$$

where $\mathbf{S}_i$ denotes the spin operator of the electron in the i-th quantum dot and J_{ij} the exchange energy between spins i and j.

It has to be noted, however, that this proposal for exchange-based QC extends far beyond electron spins in quantum dots. Subsequent proposals for QC, using the nuclear spins of donor atoms buried in a silicon substrate (Kane, 1998), or using electron spins in SiGe quantum dots (Vrijen *et al.*, 2000), electrons trapped by surface acoustic waves (Barnes *et al.*, 2000), and spins of paramagnetic impurities (Bao *et al.*, 2003), rely on the same type of interaction.

In Eq. (10), we have also taken into account the Zeeman coupling to an external magnetic field $\mathbf{B}$ which may be spatially varying. It may also be that the Lande g-factor g_i is also be site-dependent in some semiconductor heterostructures. The Bohr magnetic moment is denoted by μ_B. Structures with two coupled quantum dots where the electron number could be controlled one-by-one down to a single electron per dot have recently been demonstrated in GaAs-AlGaAs heterostructures (Elzerman *et al.*, 2003), see Fig. 6.

In the "idle" phase, i.e., when no quantum gates are performed on the register, the exchange coupling would be switched off $J_{ij} = 0$ between all dots i and j. In order to perform an elementary two-qubit gate between dots i and j, the exchange coupling between dots i and j is temporarily switched on, while leaving the other exchange couplings off.

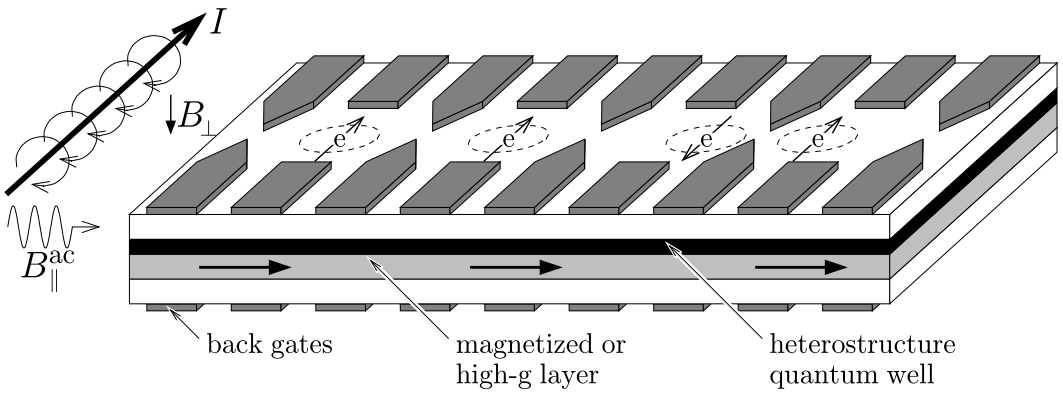


FIG. 1 Schematics of a quantum-dot array for quantum computing according to (Loss and DiVincenzo, 1998). Quantum dots (dashed circles) are defined in a two-dimensional semiconductor heterostructure with metal gates (shown schematically in grey) and host one (excess) electron (e) with a spin 1/2 each. By controlling the gate voltages, the coupling of adjacent quantum dots is switched on and off for quantum gate operations.

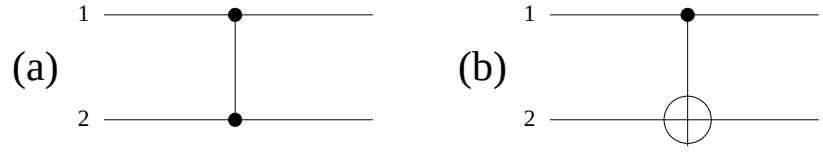


FIG. 2 Circuit notation of two examples of two-qubit gates that are universal for quantum computation when combined with single-qubit gates. (a) The 'square-root-of-swap' (S) gate, (b) the XOR gate.

Several non-overlapping pairs of qubits can be coupled simultaneously in this way. A pulse $J_{ij}(t)$ with the property

$$\frac{1}{\hbar}\int J_{ij}(t')dt' = \frac{\pi}{2} \pmod{2\pi} \tag{11}$$

generates the above-mentioned square-root of SWAP gate (up to an unimportant global phase factor $e^{-i\pi/8}$ which we omit below),

$$S \simeq \exp\left(\frac{i}{\hbar}\int dt' H(t')\right) = \exp\left(i\frac{\pi}{2}\mathbf{S}_i\cdot\mathbf{S}_j\right). \tag{12}$$

The quantum gate S can be combined with single-spin rotations

$$U_i(\boldsymbol{\phi}) = \exp(i\boldsymbol{\phi}\cdot\mathbf{S}_i), \tag{13}$$

to produce a controlled phase flip (CPF) (Loss and DiVincenzo, 1998),

$$U_{CPF} = e^{-i\frac{\pi}{2}}e^{i\frac{\pi}{2}S_1^z}e^{-i\frac{\pi}{2}S_2^z}Se^{i\pi S_1^z}S, \tag{14}$$

which, up to a basis change, equals the quantum XOR gate:

$$U_{XOR} = VU_{CPF}V^\dagger, \tag{15}$$

$$V = \exp(-i\pi S_2^y/2). \tag{16}$$

The effect of an inhomogeneous external magnetic field on the exchange interaction and the robustness of the procedure described here are discussed in (de Sousa *et al.*, 2001).

B. QC with anisotropic couplings

1. Ising and transverse (XY) coupling

Both for photon-mediated spin-spin coupling in a semiconductor microcavity (Imamoğlu *et al.*, 1999) and for inductively coupled superconducting qubits (Makhlin *et al.*, 1999, 2001), which will both be further discussed in

Secs. III.E and IV below, the coupling takes an anisotropic form instead of being described by the isotropic Heisenberg Hamiltonian Eq. (10). In both cases, the form of the coupling turns out to be that of the XY (transverse) spin Hamiltonian,

$$H_{XY} = J\sum_{i,j}(S_i^x S_j^x + S_i^y S_j^y) = \frac{J}{2}\begin{pmatrix} 0 & 0 & 0 & 0 \\ 0 & 0 & 1 & 0 \\ 0 & 1 & 0 & 0 \\ 0 & 0 & 0 & 0 \end{pmatrix}, \tag{17}$$

where we chose the S^z basis of the two interacting qubits for the matrix representation of H_{XY}.

It is known that any generic two-qubit Hamiltonian gives rise to a universal set of gates when combined with single-qubit operations. In two notable cases of anisotropic spin couplings, the Ising and the XY interactions, it is known how the CPF and XOR gates can be constructed. In the case of a system described by the Ising Hamiltonian $H_I = JS_1^z S_2^z$ and a homogeneous magnetic field in z direction, there is a particularly simple realization of the CPF gate with constant parameters, namely $U_{\rm CPF} = \exp(i\pi(1 - 2S_1^z - 2S_2^z + 4S_1^z S_2^z)/4)$ (Loss and DiVincenzo, 1998).

For the transverse spin-spin coupling of Eq. (17), we find that a useful two-qubit gate, such as the conditional-phase-flip (CPF) operation, can be carried out by combining H_{XY} with one-bit rotations. The unitary evolution operator generated by the Hamiltonian of Eq. (17) is

$$U_{XY}(\phi) \;=\; T\exp\left[i\int dt H_{XY}\right] = \exp\left[i\phi(S_i^x S_j^x + S_i^y S_j^y)\right] \tag{18}$$

where $\phi = \int dt J(t)$. The CPF gate ($U_{\rm CPF}$) can be realized by the sequence of operators (Burkard *et al.*, 1999b; Imamoğlu *et al.*, 1999)

$$U_{\rm CPF} = e^{i\pi/4} e^{i\pi \mathbf{n}_i\cdot\boldsymbol{\sigma}_i/3} e^{i\pi \mathbf{n}_j\cdot\boldsymbol{\sigma}_j/3} U_{XY}(\pi/2) e^{i\pi\sigma_z^i/2} U_{XY}(\pi/2) e^{i\pi\sigma_y^i/4} e^{i\pi\sigma_y^j/4} \tag{19}$$

where $\boldsymbol{\sigma}$ denotes the vector Pauli operator, where $\mathbf{S} = \boldsymbol{\sigma}/2$, and $\mathbf{n}_i = (1,1,-1)/\sqrt{3}$ and $\mathbf{n}_j = (-1,1,1)/\sqrt{3}$. The XOR gate can be realized by combining the CPF operation with single-qubit rotations as in Eqs. (15) and (16).

While it is impossible to generate the CNOT gate with a single use of the XY Hamiltonian (Burkard *et al.*, 1999b), it is possible to generate a different universal quantum gate with the XY interaction in a single pulse; the CNOT + SWAP (CNS) gate $U_{\rm CNS} = U_{\rm SWAP}U_{\rm XOR}$, is generated as (Schuch and Siewert, 2003)

$$U_{\rm CNS} = H_1 U_{XY}(\pi) e^{-i\pi\sigma_z^i/4} e^{-i\pi\sigma_z^j/4} H_2, \tag{20}$$

where H_i is the Hadamard gate

$$H = \frac{1}{\sqrt{2}}\begin{pmatrix} 1 & 1 \\ 1 & -1 \end{pmatrix}, \tag{21}$$

applied to qubit i.

Gate errors due to unwanted inhomogeneous magnetic fields during an otherwise isotropic coupling, effectively creating an anisotropy, have been studied and quantified in (Hu and Das Sarma, 2003).

2. Anisotropy due to the spin-orbit coupling

The exchange interaction, Eq. (10), between electron spins in tunnel-coupled sites (such as quantum dots) can acquire anisotropic terms due to spin-orbit coupling during tunneling between the sites (Kavokin, 2001). Surprisingly, it turns out that the first-order effect of the spin-orbit coupling during quantum gate operations can be eliminated

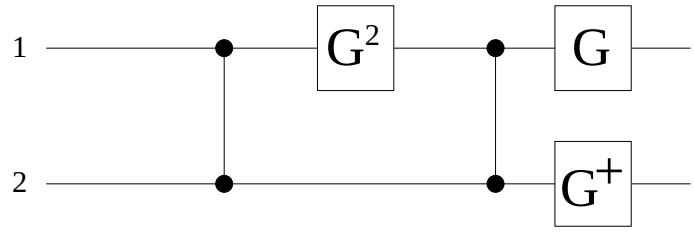


FIG. 3 A circuit representation for the conditional phase flip (CPF), Eq. (14). The single qubit rotations are $G = e^{i\frac{\pi}{2}S^z}$, $G^\dagger = e^{-i\frac{\pi}{2}S^z}$, and $G^2 = e^{i\pi S^z}$. The CPF is related to the XOR gate Eq. (7) by the basis transformation Eq. (15).

by using time-symmetric pulse shapes for the coupling between the spins (Bonesteel *et al.*, 2001). A related, but independent, result shows that the spin-orbit effects *exactly* cancel in the gate sequence on the right hand side of Eq. (14) required to produce the quantum XOR gate, provided that the pulse form for the spin-orbit and the exchange couplings are identical (Burkard and Loss, 2002). The XOR gate being universal when complemented with single-qubit operations, this result implies that the spin-orbit coupling can be dealt with in any quantum computation. In any real implementation, there will be some (small) discrepancy between the pulse shapes for the exchange and the spin-orbit coupling; however, one can choose two pulse shapes which are very similar. It was shown that the cancellation still holds to a very good approximation in such a case, i.e. the effect of the spin-orbit coupling will still be strongly suppressed (Burkard and Loss, 2002). There is also an effect of dipolar interactions between adjacent spins, providing another anisotropic coupling; this coupling can also be treated as an anisotropic contribution to Eq. (10) and therefore cancels out in the gate sequence Eq. (14) for the same reasons as the spin-orbit interaction.

The spin-orbit coupling for a conduction-band electron is given by the following Hamiltonian (Gantmakher and Levinson, 1987), being linear in the 2D momentum operator p_i, $i = x, y$ ([100] orientation of the 2D plane),

$$H_{\rm so} = \sum_{i,j=x,y} \beta_{ij}\sigma_i p_j, \tag{22}$$

where the constants β_{ij} depend on the strength of the confinement in z-direction and are of the order $(1 \div 3)\cdot 10^5\,$cm/s for GaAs heterostructures. Combining the isotropic Heisenberg coupling (10) with the anisotropic exchange between two localized spins $\mathbf{S}_1$ and $\mathbf{S}_2$ one obtains the Hamiltonian (Burkard and Loss, 2002)

$$H(t) = J(t)\left(\mathbf{S}_1\cdot\mathbf{S}_2 + \mathcal{A}(t)\right), \tag{23}$$

where the anisotropic part is given by the expression (Kavokin, 2001),

$$\mathcal{A}(t) = \boldsymbol{\beta}(t)\cdot(\mathbf{S}_1\times\mathbf{S}_2) + \gamma(t)(\boldsymbol{\beta}(t)\cdot\mathbf{S}_1)(\boldsymbol{\beta}(t)\cdot\mathbf{S}_2), \tag{24}$$

and $\beta_i = \sum_j \beta_{ij}\langle\psi_1|ip_j|\psi_2\rangle$ is the spin-orbit field, $|\psi_i\rangle$ the ground state in site (dot) $i = 1, 2$, and $\gamma \approx O(\beta^0)$. As was discussed in Sec. II.A, for $\mathcal{A} = 0$, the quantum XOR gate can be obtained by applying $H(t)$ twice, together with single-spin rotations, see Eqs. (14) and (16). Moreover, if $\mathcal{A} = 0$, then $H(t)$ commutes with itself at different times and the time-ordered exponential

$$U(\varphi) = T\exp\left(-i\int_{-\tau_s/2}^{\tau_s/2} H(t)\,dt\right) \tag{25}$$

is a function of the integrated interaction strength only, $\varphi = \int_{-\tau_s/2}^{\tau_s/2} J(t)dt$. In particular, $U(\varphi = \pi/2) = U_{\rm sw}^{1/2} = S$ is the "square-root of swap" gate.

The interesting situation is of course $\mathcal{A} \neq 0$. If in this case, $\boldsymbol{\beta}$ and γ (and thus $\mathcal{A}$) are time-independent, then $H(t)$ *still* commutes with itself at different times and one can find a fixed coordinate system in which $\boldsymbol{\beta}$ is parallel to the z axis. In this basis, the anisotropic term Eq. (24) can be expressed as

$$\mathcal{A} = \beta(S_1^x S_2^y - S_1^y S_2^x) + \delta S_1^z S_2^z, \tag{26}$$

with $\delta = \gamma\beta^2$. In the singlet-triplet basis with basis vectors $\{|T_+\rangle = |\uparrow\uparrow\rangle, |S\rangle = (|\uparrow\downarrow\rangle - |\downarrow\uparrow\rangle)/\sqrt{2}, |T_0\rangle = (|\uparrow\downarrow\rangle + |\downarrow\uparrow\rangle)/\sqrt{2}, |T_-\rangle = |\downarrow\downarrow\rangle\}$ the gate sequence Eq. (14), including the anisotropy Eq. (24), yields the unitary operation

$$U_g = \mathrm{diag}(ie^{-i\varphi(1+\delta)}, 1, 1, -ie^{-i\varphi(1+\delta)}), \tag{27}$$

where $\mathrm{diag}(x_1, \ldots, x_4)$ denotes the diagonal matrix with diagonal entries $x_1, \ldots, x_4$. Note that the pulse strength φ and the spin-orbit parameters only enter U_g in the $S^z = \pm 1$ subspaces. Moreover, the terms linear in $\boldsymbol{\beta}$ have canceled out exactly in U_g. With the choice $\varphi = \pi/2(1+\delta)$, one obtains the conditional phase flip gate $U_g = U_{CPF} = \mathrm{diag}(1, 1, 1, -1)$, being equivalent to the XOR up to the basis change, Eq. (16). Therefore, the anisoptropic terms $\mathcal{A} = $ const. in the spin Hamiltonian cancel exactly in the gate sequence Eq. (15) for the quantum XOR.

We briefly discuss what happens if, as can be expected in real systems, the anisotropic terms in the Hamiltonian H are not exactly proportional to $J(t)$, i.e. if $\mathcal{A}(t)$ is time-dependent. Generally, both $\boldsymbol{\beta}$ and γ depend on time. In this more general case, we cannot exactly eliminate the effect of the anisotropy because of the time-ordering in Eq. (25) and since the Hamiltonian cannot be expected to commute with itself at different times, $[H(t), H(t')] \neq 0$. The estimated gate errors $\epsilon = ||U_g - U_{CPF}||^2$ due to the anisotropy in the case where $\mathcal{A}(t)$ is only weakly time-dependent are $\epsilon \leq \Delta^2$ where we use $\Delta\beta(t) = \beta(t) - \beta_0$ and

$$\Delta = (|\varphi|\beta_0/2)\max_{|t|\leq\tau_s/2}|(J(t)/J_0)(\beta(t)/\beta_0 - 1)|, \tag{28}$$

where J_0 stands for the average exchange coupling, $J_0 = \varphi/\tau_s \neq 0$. It can be shown (Burkard and Loss, 2002) that for tunnel-coupled quantum dots, it is possible to choose a weakly time-dependent $\mathcal{A}$ by using Eq. (52) for the exchange coupling and the result

$$b(d,q) \equiv |J(d,q)\boldsymbol{\beta}(d,q)| = b_0\sqrt{q}d\exp(-2qd^2), \tag{29}$$

where $b_0 = a/a_B^0$, $a_B^0 = \sqrt{\hbar/m\omega_0}$, and where a is a constant depending on the spin-orbit parameter (for a 5 nm wide [100] GaAs quantum well $a \approx 2$ meV nm), $q = \omega/\omega_0$. The minimal value of the quantum dot confinement energy ω is denoted by ω_0. A possible model for the switching process is the use of a time-dependent confinement strength $q(t) = \omega(t)/\omega_0 = \cosh^2(\alpha t/\tau_s)$ (where *alpha* is a number of order 1, e.g., $\alpha = 4$). This pulse shape has favorable adiabatic properties (Burkard *et al.*, 1999a; Schliemann *et al.*, 2001b), as detailed in Sec. II.E, and leads to a pulsed exchange interaction $J(t) = J(d, q(t))$ and spin-orbit field $b(t) = b(d, q(t))$, where $-\tau_s/2 \leq t \leq \tau_s/2$. The resulting error was estimates in (Burkard and Loss, 2002) as $\Delta \approx 7 \cdot 10^{-3}$, leading to gate errors occurring at a rate $\epsilon \approx 4\Delta^2 \approx 2 \cdot 10^{-4}$ being around the currently known threshold for fault tolerant quantum computation (Preskill, 1998a,b). The error ϵ can be further reduced by performing the gates more slowly, with a long period of constant $\mathcal{A}$ between the rise and fall of the pulses.

C. Universal QC with the exchange coupling

In some situations, a local controllable field $\mathbf{B}_i$ or g-factor g_i in the Hamiltonian Eq. (10) and thus the single-qubit operations $SU(2)$ in the universal set Eq. (6) may be more costly to implement than the tunable exchange coupling generating the spin-spin coupling $U_{(2)}$ (note, however, that there exist all-electric switching schemes using g-factor modulation, see Sec. III.D). A scheme has been developed in which the Heisenberg interaction alone suffices to exactly implement any quantum computer circuit, at a price of a factor of three in additional qubits and about a factor of ten in additional two-qubit operations. However, the Heisenberg interaction by itself is not a universal gate (Barenco *et al.*, 1995a), in the sense that it cannot generate any arbitrary unitary transformation on a collection of spin-1/2 qubits. This is why in Eq. (6), the Heisenberg interaction needs to be combined with some other means of applying independent one-qubit gates. The Heisenberg interaction alone does not give a universal quantum gate because it has too much symmetry: it commutes with the operators S^2 and S_z, where the total spin is defined as

$$\mathbf{S} = \sum_{i=1}^{n} \mathbf{S}_i, \tag{30}$$

and therefore it can only rotate among states with the same S, S_z quantum numbers.

1. Encoding

The exchange coupling is thus not universal in the full Hilbert space; but, by working exclusively in one symmetry sector of the Hilbert space with fixed S, S_z quantum numbers, the exchange coupling can be made universal. This restriction is achieved by defining coded qubit states, ones for which the spin quantum numbers always remain the same (Bacon *et al.*, 2000; Kempe *et al.*, 2001; Viola *et al.*, 2000). The smallest number of spins 1/2 for which two orthogonal states with identical S, S_z exist is three. The space of three-spin states with spin quantum numbers $S = 1/2$, $S_z = +1/2$ is two-dimensional and will serve to represent our coded qubit. An explicit choice for the basis states of this qubit are

$$|0_L\rangle = |S\rangle|\uparrow\rangle, \tag{31}$$

$$|1_L\rangle = \sqrt{2/3}|T_+\rangle|\downarrow\rangle - \sqrt{1/3}|T_0\rangle|\uparrow\rangle, \tag{32}$$

where $|S\rangle = \sqrt{1/2}(|\uparrow\downarrow\rangle - |\downarrow\uparrow\rangle)$ is the singlet state of spins 1 and 2 (see Fig. 4a) of the three-spin block, and $|T_+\rangle = |\uparrow\uparrow\rangle$ and $|T_0\rangle = \sqrt{1/2}(|\uparrow\downarrow\rangle + |\downarrow\uparrow\rangle)$ are triplet states of these two spins. While in principle this solves the problem of exchange-only QC, in practice we would like to know what the overhead in terms of qubits (for coding) and gates (for operating on encoded qubits with the exchange interaction) will be, and how a universal set of operations on the encoded qubits can be achieved (DiVincenzo *et al.*, 2000). It has also been found that the anisotropic XY interaction (17) alone is sufficient for quantum computation (Kempe and Whaley, 2002), a result which was later generalized to large class of anisotropic exchange Hamiltonians (Vala and Whaley, 2002). An encoding involving two spins per qubit has also been demonstrated for universal quantum logic starting from locally alternating g-factors (Levy, 2002) and from a homogeneous magnetic field combined with anisotropic exchange interactions (Wu and Lidar, 2002a,b; Wu *et al.*, 2004).

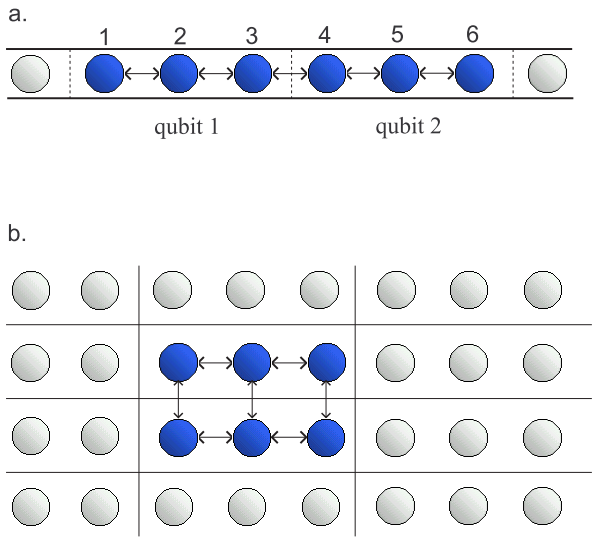


FIG. 4 Possible layouts of spin-1/2 devices. a) One-dimensional layout. We consider two different assumptions about how the exchange interactions can be turned on and off in this layout: 1) At any given time each spin can be exchange-coupled to at most one other spin (we refer to this as "serial operation" in the text), 2) All exchange interactions can be turned on simultaneously between any neighboring pair of spins in the line shown ("1D parallel operation"). b) Possible two-dimensional layout with interactions in a rectangular array. We imagine that any exchange interaction can be turned on between neighboring spins in this array ("2D parallel operation"). Of course other arrangements are possible, but these should be representative of the constraints that will be faced in actual device layouts.

2. One-qubit gates

A one-qubit gate on a single three-spin block is performed as follows. The Hamiltonian H_{12} generates a rotation $U_{12} = \exp(i/\hbar \int J\vec{S}_1 \cdot \vec{S}_2 dt)$ which is just a z-axis rotation (in Bloch-sphere notation) on the coded qubit, while H_{23} produces a rotation about an axis in the x-z plane, at an angle of 120^o from the z-axis. Since simultaneous application of H_{12} and H_{23} can generate a rotation around the x-axis, three steps of 1D parallel operation (defined in Fig. 4a) permit any one-qubit rotation, using the classic Euler-angle construction. In serial operation, it can be found numerically that four steps are always adequate when only nearest-neighbor interactions are possible (e.g. the sequence H_{12}-H_{23}-H_{12}-H_{23} shown in Fig. 5a, with suitable interaction strengths), while three steps suffice if interactions can be turned on between any pair of spins (e.g. H_{12}-H_{23}-H_{13}, see Fig. 5b).

3. Two-qubit gates

The implementation of two-qubit gates for universal QC with the exchange interaction on two three-spin code blocks is less intuitive that the corresponding task for one-qubit gates. Much of the difficulty of these searches arises from the fact that while the four basis states $|0_L, 1_L\rangle|0_L, 1_L\rangle$ have total spin quantum numbers $S = 1$, $S_z = +1$, the complete space with these quantum numbers for six spins has nine states, and exchanges involving these spins perform rotations in this full nine-dimensional space. Numerical searches for the implementation of two-qubit gates using a simple minimization algorithm (DiVincenzo *et al.*, 2000) aided by the two-qubit gates invariants (Makhlin, 2002) have resulted in a sequence for an encoded CNOT operation that is depicted in Fig. 5. The solution shown in Fig. 5c appears to be optimal for serial operation and happens to involve only nearest neighbors in the 1D arrangement of Fig. 4a. There also are (apparently) optimal numerical solutions for parallel operation mode. For the 1D layout of Fig. 4a, the simplest solution found involves 8 clock cycles with just 8*4 different interaction-time parameters (H_{12} can always be zero in this implementation). For the 2D parallel mode of Fig. 4b, a solution was found using just 7 clock cycles (7*7 interaction times).

In the present scheme, quantum computation would proceed as follows. In the beginning, all the computational qubits would be set to the $|0_L\rangle$ state which is easily obtained using the exchange interaction: if a strong H_{12} is turned on in each coded block and the temperature made lower than the strength J of the interaction, these two spins will equilibrate to their ground state, which is the singlet state. The third spin in the block should be in the $|\uparrow\rangle$ state, which can be achieved by also placing the entire system in a moderately strong magnetic field B, such that $k_B T << g\mu_B B < J$ (it can be shown that in a slightly more general scheme involving both the $S_z = +1$ and $S_z = -1$ subspaces, the last step can be omitted). After the computation, with the one- and two-qubit gates implemented according to the schemes mentioned above, the final qubit measurement, we note that determining whether the spins 1 and 2 of the block are in a singlet or a triplet suffices to perfectly distinguish (DiVincenzo *et al.*, 1999) $|0_L\rangle$ from $|1_L\rangle$ (again, the state of the third spin does not enter).

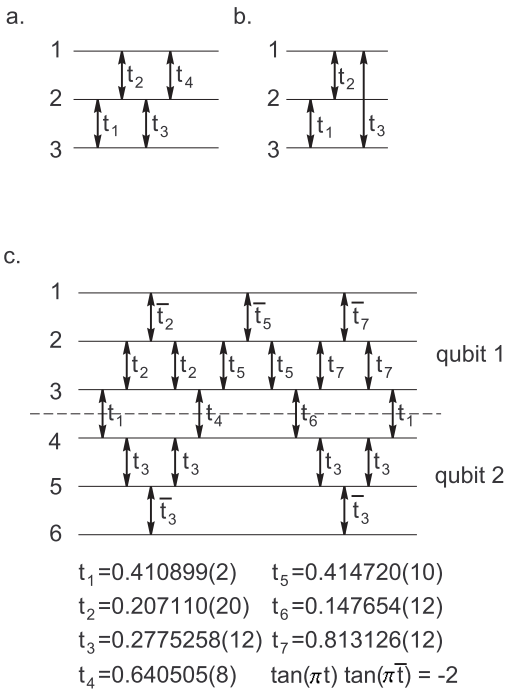


FIG. 5 Circuits for implementing single-qubit and two-qubit rotations using serial operations. a) Single-qubit rotations by nearest-neighbor interactions. Four exchanges (double-headed arrows) with variable time parameters τ_i are always enough to perform any such rotation, one of the two possible layouts is shown. b) Non-nearest neighbor interactions. Only three interactions are needed, one of the possible layouts is shown. c) Circuit of 19 interactions that produce a cNOT between two coded qubits (up to one-qubit gates before and after). The durations of each interaction are given in units such that for $t = 1/2$ the rotation $U_{ij} = \exp(iJt\vec{S}_i \cdot \vec{S}_j/\hbar)$ is a SWAP, interchanging the quantum states of the two spins i, j. The $\bar{t}_i$ parameters are not independent, they are related to the t_is as indicated. The uncertainty of the final digits of these times are indicated in parentheses. With these uncertainties, the absolute inaccuracy of the matrix elements of the two-qubit gate rotations achieved is no greater than 6×10^{-5}. Further fine tuning of these time parameters would give the cNOT to any desired accuracy. In a practical implementation, the exchange couplings $J(t)$ would be turned on and off smoothly; then the time values given here provide a specification for the integrated value $\int J(t)dt$. The functional form of $J(t)$ is irrelevant, but its integral must be controlled to the precision indicated.

4. Protection against errors

Codes of the type of Eqs. (31) and (32) have first been introduced as a computational basis in *decoherence-free subspaces*, i.e., subspaces of a Hilbert space which are protected against errors with a certain type of symmetry (Bacon *et al.*, 2000; Kempe *et al.*, 2001; Lidar *et al.*, 1999, 1998; Zanardi and Rasetti, 1997). Moreover, it has been suggested that the logical subspace may be energetically separated from the remaining Hilbert space and thus protected against errors in a system where a certain combination of exchange couplings always remains switched on (Bacon *et al.*, 2001; Weinstein and Hellberg, 2004).

5. Related ideas

Encoded qubits of a different kind, so-called spin-cluster qubits (Meier *et al.*, 2003a,b), have been proposed in order to relax the requirements for control on the single-spin level while inheriting the favorable single-spin properties such as long decoherence time and fast gate operating time. Spin cluster qubits are finite spin chains with Heisenberg or anisotropic (XY and Ising-like) antiferromagnetic exchange interaction that can have uniform or nonuniform interaction constants.

The use of many-electron QDs for exchange-based quantum computations has been analyzed in (Vorojtsov *et al.*, 2004). A particular implementation of three-spin QDs encoding one qubit has been put forward in (Kyriakidis and Penney, 2004).

D. Optimization of quantum circuits

A quantum gate operating on n qubits can be represented as a $2^n \times 2^n$ unitary matrix. Any quantum computation or algorithm can be split up into a series of elementary gate operations drawn from a universal set involving only one or two qubits, as in Eq. (6). This is the quantum circuit representation of quantum algorithms (or, unitary operations). For a simple example, see Fig. 3 for a circuit representations of CPF in terms of sqrt-of-SWAP gates. However, quantum circuits are in general not the most efficient way of implementing a quantum computation (Burkard *et al.*, 1999b). There are a number of related but different approaches using, e.g., genetic algorithms and chirped Gaussian pulses (Sanders *et al.*, 1999) or control theory (Khaneja *et al.*, 2001).

If one is interested in optimizing the switching time τ_s for a desired unitary U, with a given Hamiltonian, e.g., the spin Hamiltonian Eq. (10), one can depart from the circuit representation of the unitary by allowing arbitrary time dependent parameters $\vec{p}(t)$ in the Hamiltonian. In the case of the spin Hamiltonian (10), we have $\vec{p} = (J, \mathbf{B}_1, \mathbf{B}_2, \ldots)$.

We will only demonstrate this optimization in the case of a simple two-qubit unitary, the XOR (CNOT) gate. The optimization method can in principle be applied to unitaries of any size; note, however, that the optimization as an arbitrary classical computational task is typically a hard computation in itself.

1. Serial pulse mode

We first restrict ourselves to a special class of parameter functions $\vec{p}(t)$, in which at every time t, only one component of $\vec{p}(t)$ is non-zero. If we further restrict ourselves to parameter functions in which the duration of the J-pulses with $\vec{p} = (J, 0, 0, \ldots)$ are $\pi/2$ pulses generating the sqrt-of-swap S, then we are back to the circuit model with the universal set Eq. (6) and $U_{(2)} = S$. In this case we can optimize circuits, e.g., to have as few instances of S as possible. E.g., it turns out that the use of two S for a CPF as in the sequence Eq. (14), and therefore, for XOR, is optimal. Such minimal requirements for the implementation of a unitary U can be proven by analyzing the set $\mathcal{P}(U)$ of product states $\left\{|\Psi\rangle \in \mathcal{H} = \mathcal{H}_2^{\otimes M} \middle| |\Psi\rangle = |\phi_1\rangle \otimes \cdots \otimes |\phi_M\rangle; |\phi_i\rangle \in \mathcal{H}_2 \right\}$ which are mapped back onto product states by U (Burkard *et al.*, 1999b). An alternative method for determining whether a Hamiltonian generates a gate in a single pulse involves the invariants under addition of single-qubit gates (Makhlin, 2002).

2. Parallel pulse mode

In the case where several or all parameters $\vec{p}$ can be changed simultaneously, we expect that a given quantum gate, say XOR, can be performed faster than by changing only one parameter at a time as in the serial pulse mode. The unitary time evolution operator after time t is the following functional in $\vec{p}$,

$$U_t[\vec{p}(\tau)] = T \exp\left(\frac{i}{\hbar}\int_0^t H(\vec{p}(\tau))\, d\tau\right), \tag{33}$$

where T denotes the time-ordering. For a given quantum gate U_g, the integral equation $U_t[\vec{p}(\tau)] = U_g$ has to be solved for the functions $\vec{p}(\tau)$. An *optimal* solution is given by a set of bounded functions $|p_i(\tau)| < M_i$ requiring minimal time t for a fixed set of bounds M_i. In order to simplify the problem, one can restrict the problem to piecewise-constant functions,

$$\begin{aligned} U_N(\vec{p}^{(1)}, ..., \vec{p}^{(N)}; \phi) &= e^{i\phi} U_N(\vec{p}^{(N)}) \cdots U_2(\vec{p}^{(2)}) U_1(\vec{p}^{(1)}), \\ U_k(\vec{p}^{(k)}) &= \exp\left\{ itH(\vec{p}^{(k)}) \right\}. \end{aligned} \tag{34}$$

For each of the N time intervals, one has the freedom to choose a new set of parameters $\vec{p}^{(k)} = (J, \mathbf{B}_1, \mathbf{B}_2)$. The discretized problem can now be treated both analytically and numerically (Burkard *et al.*, 1999b).

One finds analytically that CPF can be implemented in a single step by fixing $N = 1$, i.e., all parameters in Eq. (10) simultaneously non-zero but constant,

$$U_{CPF} = \exp\left[itH(J, \mathbf{B}_1, \mathbf{B}_2)\right], \tag{35}$$

The parameters are (in units of $2\pi\hbar/t$),

$$\begin{aligned} J = k - n - 2m - \frac{1}{2} \ , \qquad & \phi = -\pi(n + \frac{1}{2}) \\ \mathbf{B}_1 = \frac{1}{2}(0, 0, n + \frac{1}{2} + \sqrt{k^2 - J^2}) \ , \qquad & \mathbf{B}_2 = \frac{1}{2}(0, 0, n + \frac{1}{2} - \sqrt{k^2 - J^2}), \end{aligned} \tag{36}$$

where n, and m are arbitrary integers, and k is an integer satisfying $2|k| \geq |n + 2m + \frac{1}{2}|$. In the specific case where all constraints are equal to M, we find that the solution for $k = 1$, $m = n = 0$,

$$J = \frac{1}{2}, \quad B_1^z = \frac{1}{4}(1 + \sqrt{3}), \quad B_2^z = \frac{1}{4}(1 - \sqrt{3}), \quad \phi = -\frac{\pi}{2} \tag{37}$$

has the shortest switching time,

$$t_{\mathrm{CPF},p} = \frac{2\pi\hbar}{4M}(1 + \sqrt{3}) = 0.683\frac{2\pi\hbar}{M}, \tag{38}$$

less than half the time which is used for the serial pulse quantum circuit Eq. (14), $t_{\mathrm{CPF},s} = 1.5 \cdot 2\pi\hbar/M$. Numerically, one finds that XOR requires at least $N = 2$ steps,

$$U_{\mathrm{XOR}} = e^{i\phi} e^{i\phi} \exp\left[itH(\vec{p}^{(2)})\right] \exp\left[itH(\vec{p}^{(1)})\right], \tag{39}$$

with the parameter values (in units of $2\pi\hbar/t$)

k	$J^{(k)}$	$B_{1x}^{(k)}$	$B_{2x}^{(k)}$	$B_{1y}^{(k)}$	$B_{2y}^{(k)}$	$B_{1z}^{(k)}$	$B_{2z}^{(k)}$
1	0.187	−0.025	0.464	0.205	0.195	−0.420	0.395
2	0.617	−0.220	0.345	−0.384	0.244	0.353	0.108

(40)

and the global phase $\phi = -0.8481 \cdot \pi$, where the time t has to be chosen such that none of the parameters exceeds the bound M. The total switching time for equal bounds is in this case $t_{\mathrm{XOR},p} = (0.4643{+}0.6170)2\pi\hbar/M = 1.0813{\cdot}2\pi\hbar/M$, compared to $t_{\mathrm{XOR},s} = 2 \cdot 2\pi\hbar/M$ for the serial switching.

3. Anisotropic systems

Parallel switching is also possible with the XY dynamics Eq. (17). It can be shown that U_{CPF} requires two pulses,

$$U_{CPF} = e^{i\phi}\, U_2 U_1, \tag{41}$$

$$\text{where} \qquad U_k = \exp\left[2\pi i H_{XY,B}(J^{(k)}, B_x^{(k)}, B_z^{(k)})\right], \quad k = 1, 2.$$

Note that all magnetic fields can be chosen homogeneous ($\mathbf{B}_1^{(k)} = \mathbf{B}_2^{(k)} \equiv \mathbf{B}^{(k)}$) and perpendicular to the y-axis ($B_y = 0$). Here we give one possible realization which is found numerically ($\phi = -3\pi/4$):

k	$J^{(k)}$	$B_x^{(k)}$	$B_z^{(k)}$
1	0.7500	**0.7906**	0.5728
2	**0.5000**	0.0000	0.2500

(42)

The total switching time for CPF, assuming equal bounds $M_J = M_B \equiv M$ for J and B, is $t_{\mathrm{CPF},p}^{XY} = 1.291 \cdot 2\pi\hbar/M$, compared to $t_{\mathrm{CPF},s}^{XY} = 2.167 \cdot 2\pi\hbar/M$ for the serial pulse sequence defined in Eq. (19).

In order to produce the XOR gate Eq. (7) we can implement the basis change Eq. (15) using the single-qubit rotation V. This procedure requires a total of four steps for the XOR gate. Another way of achieving XOR is the following sequence which we found numerically and which takes only three steps:

$$U_{XOR} = \exp(3i\pi/4) U_3 U_2 U_1, \tag{43}$$

with the following parameters:

k	$J^{(k)}$	$B_{1x}^{(k)}$	$B_{2x}^{(k)}$	$B_{1y}^{(k)}$	$B_{2y}^{(k)}$	$B_{1z}^{(k)}$	$B_{2z}^{(k)}$
1	1.802	0.615	**2.045**	0.020	0.316	0.794	0.130
2	**3.344**	0.348	0.718	0.259	0.493	1.583	1.062
3	**1.903**	1.193	0.705	0.413	−0.305	0.589	0.604

(44)

The total switching time of $t_{\mathrm{XOR},p}^{XY} = 7.29 \cdot 2\pi\hbar/M$ (compared to $2.67 \cdot 2\pi\hbar/M$ using CPF and a basis change) indicates that Eq. (44) is not an optimal solution.

E. Adiabaticity

Quantum gates are generated by controlling the parameters in the Hamiltonian Eq. (10), $J_{ij}(t)$ and $\mathbf{B}_i(t)$ (or $g_i(t)$), as a function of time. E.g., the exchange coupling J depends on time via some physically controlled quantity, such as an electric gate voltage $v(t)$, i.e., $J(t) = J(v(t))$ (similarly for the effective g-factor $g(t)$). According to Eq. (11), only the time integral $\int_0^\tau J(v(t))dt$ needs to assume a certain value (modulo 2π) in order to generate the

correct quantum gate and the pulse form of $v(t)$ does not matter. However, the exchange interaction $J(t)$ needs to be switched *adiabatically* in order to avoid unwanted excitations in the system. The adiabaticity condition is (Burkard *et al.*, 2000a, 1999a,b) $|\dot{v}/v| \ll \delta\varepsilon/\hbar$, where $\delta\varepsilon$ is the energy scale on which excitations may occur. Here, $\delta\varepsilon$ denotes the energy-level separation of a single dot, i.e., the smaller of either the single-electron level spacing or the on-site Coulomb energy U required to add a second electron to a dot. A rectangular pulse leads to excitation of higher levels, whereas an adiabatic pulse with amplitude v_0 is e.g. given by $v(t) = v_0\,\mathrm{sech}(t/\Delta t)$ where Δt controls the width of the pulse. We need to use a switching time $\tau_s > \Delta t$, such that $v(t = \tau_s/2)/v_0$ becomes vanishingly small. We then have $|\dot{v}/v| = |\tanh(t/\Delta t)|/\Delta t \leq 1/\Delta t$, so we need $1/\Delta t \ll \delta\varepsilon/\hbar$ for adiabatic switching. The Fourier transform $v(\omega) = \Delta t v_0 \pi\,\mathrm{sech}(\pi\omega\Delta t)$ has the same shape as $v(t)$ but width $2/\pi\Delta t$. In particular, $v(\omega)$ decays exponentially in the frequency ω, whereas it decays only with $1/\omega$ for a rectangular pulse.

Adiabatic switching of the exchange coupling in two coupled quantum dots and the error probability for different pulse forms have been studied numerically in (Schliemann *et al.*, 2001b). Furthermore, corrections to the fully adiabatic result have been investigated (Requist *et al.*, 2004).

III. ELECTRON SPINS

Being a natural two-level system, the spin 1/2 of the electron represents an ideal candidate for a qubit. On the one hand, the electron spin is typically quite well isolated from charge degrees of freedom (not completely, though, due to, e.g., the spin-orbit coupling). In some situations, electron spin decoherence times in solids appear to be relatively long, exceeding microseconds (Awschalom and Kikkawa, 1999; Kikkawa and Awschalom, 1998; Kikkawa *et al.*, 1997). On the other hand, single spins in solid-state structures are not readily available and controllable. However, large experimental efforts are currently made to isolate and control single spins in solid-state structures. The spin-based proposals for quantum information processing which will be discussed below are all based on artificial nano- or micrometer-scale semiconductor structures, such as quantum dots (QDs) or microcavities.

A. Quantum Dots

In (Loss and DiVincenzo, 1998), a quantum register is proposed in which single electrons are trapped in quantum dots (QDs) that are arranged in an array or lattice in a semiconductor structure, e.g., as in Fig. 1. Electrically defined QDs in two-dimensional semiconductor heterostructures (typically, GaAs) are well-studied objects (Kouwenhoven *et al.*, 2001) in which charge transport has attracted much attention (Averin and Nazarov, 1992; Kouwenhoven *et al.*, 1997a; van der Wiel *et al.*, 2003). In recent years, the controlled storage of a *single* electron—and thus a spin 1/2 or qubit—in a QD has been achieved (Ciorga *et al.*, 2000; Elzerman *et al.*, 2003). Structures in which two QDs, each containing a well-controlled number of electrons (down to a single electron), are adjacent and tunnel-coupled, have been fabricated and studied (Elzerman *et al.*, 2003). In Fig. 6, we show an electron micrograph of a structure of the type that was used in (Elzerman *et al.*, 2003). The tunneling of electrons between the two dots is predicted to give rise to the spin exchange coupling $J\mathbf{S}_1 \cdot \mathbf{S}_2$ in Eq. (10). In the next section, we are going to outline a theory of this spin exchange mechanism.

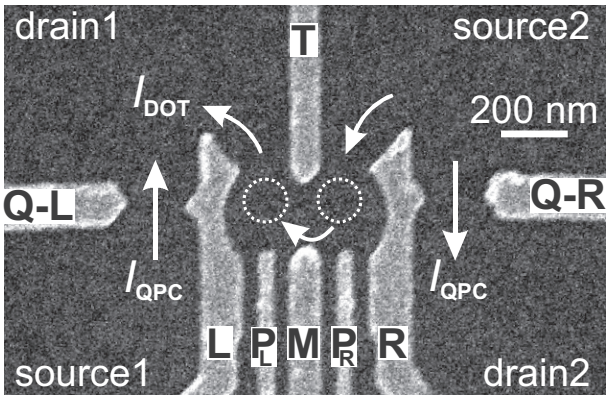


FIG. 6 Electron micrograph of a structure comprising two QDs, defined by metal electrodes (bright structures) on the surface of a GaAs/AlGaAs heterostructure (Courtesy of J. Elzerman, TU Delft). The charge on the dots is controlled in steps of single electron charges, down to one electron per dot, by tuning the voltage applied to the plunger gates $\mathrm{P_{L,R}}$ and is monitored by measuring the conductance of (i.e., the currents I_{QPC} through) the quantum point contacts (QPCs) Q-R and Q-L. Conductance spectroscopy was performed by measuring the current I_{dot} (Elzerman *et al.*, 2003).

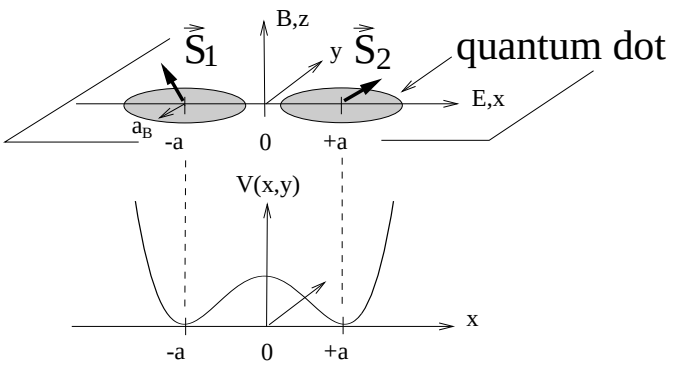


FIG. 7 Two coupled QDs with one valence electron per dot. Each electron is confined to the xy plane. The spins of the electrons in dots 1 and 2 are denoted by $\mathbf{S}_1$ and $\mathbf{S}_2$. The magnetic field B is perpendicular to the plane, i.e. along the z axis, and the electric field E is in-plane and along the x axis. The quartic potential is given in Eq. (48) and is used to model the coupling of two harmonic wells centered at $(\pm a, 0, 0)$. The exchange coupling J between the spins is a function of B, E, and the inter-dot distance $2a$.

B. Exchange in laterally coupled QDs

Due to the Coulomb interaction and the Pauli exclusion principle, the ground state of two coupled electron sites (atoms, QDs) in the absence of a magnetic field is a spin singlet (a highly entangled spin state), while the spin triplet states (one of them entangled) are typically separated by some energy gap J. This energy gap is called *exchange coupling*, as it arises from virtual electron exchange between the two sites due to the interaction. The virtual electron exchanges are allowed for opposite spins (spin singlet, $S = 0$) but forbidden by the Pauli principle for parallel spins (spin triplet, $S = 1$), therefore the energy of the singlet is lowered by the interaction.

We now introduce a model for the two laterally coupled QDs containing one (conduction band) electron each (Burkard *et al.*, 1999a). The two-dot system is shown schematically in Fig. 7. It is essential that the electrons are allowed to tunnel between the dots, and that the total wave function of the coupled system must be antisymmetric. It is this fact which introduces correlations between the spins via the charge (orbital) degrees of freedom. The electronic Hamiltonian in the effective-mass approximation for the coupled system is then given by

$$H = \sum_{i=1,2} h(\mathbf{r}_i, \mathbf{p}_i) + C + H_{\rm Z} = H_{\rm orb} + H_{\rm Z}, \tag{45}$$

where the single-particle Hamiltonian,

$$h(\mathbf{r}_i, \mathbf{p}_i) = \frac{1}{2m}\left(\mathbf{p}_i - \frac{e}{c}\mathbf{A}(\mathbf{r}_i)\right)^2 + ex_iE + V(\mathbf{r}_i), \tag{46}$$

describes the electron dynamics confined to the xy-plane and

$$C = \frac{e^2}{\kappa\,|\mathbf{r}_1 - \mathbf{r}_2|}, \tag{47}$$

represents the Coulomb interaction (unscreened in this case where the dot diameter is small or comparable to the screening length). The electrons have an effective mass m ($m = 0.067\,m_e$ in GaAs) and carry a spin-1/2 $\mathbf{S}_i$. The dielectric constant in GaAs is $\kappa = 13.1$. We allow for a magnetic field $\mathbf{B} = (0, 0, B)$ applied along the z-axis and which couples to the electron charge via the vector potential $\mathbf{A}(\mathbf{r}) = \frac{B}{2}(-y, x, 0)$. We also allow for an electric field E applied in-plane along the x-direction, i.e. along the line connecting the centers of the dots. The coupling of the dots (which includes tunneling) can be modeled by a quartic potential,

$$V(x, y) = \frac{m\omega_0^2}{2}\left(\frac{1}{4a^2}\left(x^2 - a^2\right)^2 + y^2\right), \tag{48}$$

which separates (for x around $\pm a$) into two harmonic wells of frequency ω_0, one for each dot, in the limit of large inter-dot distance, i.e. for $2a \gg 2a_{\rm B}$, where a is half the distance between the centers of the dots, and $a_{\rm B} = \sqrt{\hbar/m\omega_0}$ is the effective Bohr radius of a single isolated harmonic well. This choice for the potential is motivated by the experimental fact (Kouwenhoven *et al.*, 1997b; Tarucha *et al.*, 1996) that the spectrum of single dots in GaAs is well described by a parabolic confinement potential, e.g. with $\hbar\omega_0 = 3\,$meV (Kouwenhoven *et al.*, 1997b; Tarucha *et al.*, 1996). We note that in this simplified model, increasing (decreasing) the inter-dot distance is physically equivalent to raising (lowering) the inter-dot barrier, which can be achieved experimentally by e.g. applying a gate voltage between

the dots (Livermore *et al.*, 1996; Waugh *et al.*, 1995). Thus, the effect of such gate voltages is described in this model simply by a change of the inter-dot distance $2a$.

The magnetic field B also couples to the electron spins via the Zeeman term $H_{\rm Z} = g\mu_{\rm B}\sum_i \mathbf{B}_i \cdot \mathbf{S}_i$, where g is the effective g-factor ($g \approx -0.44$ for GaAs), and $\mu_{\rm B}$ the Bohr magneton. The ratio between the Zeeman splitting and the relevant orbital energies is small for all B-values of interest here; indeed, $g\mu_{\rm B}B/\hbar\omega_0 \lesssim 0.03$, for $B \ll B_0 = (\hbar\omega_0/\mu_{\rm B})(m/m_e) \approx 3.5\,{\rm T}$, and $g\mu_{\rm B}B/\hbar\omega_{\rm L} \lesssim 0.03$, for $B \gg B_0$, where $\omega_{\rm L} = eB/2mc$ is the Larmor frequency, and where we used $\hbar\omega_0 = 3\,{\rm meV}$. Thus, we can safely ignore the Zeeman splitting when we discuss the orbital degrees of freedom and include it later into the effective spin Hamiltonian.

1. The Heitler-London approach

We consider first the Heitler-London (HL) approximation (also known as valence orbit approximation), and then refine this approach by including hybridization as well as double occupancy in a Hund-Mulliken approach, which will finally lead us to an extension of the Hubbard description. We will see, however, that the qualitative features of J as a function of the control parameters are already captured by the simplest HL approximation for the artificial hydrogen molecule described by Eq. 45.

The HL approximation is borrowed from molecular physics. In the present case, think of a hydrogen molecule H_2. The HL approach starts from single-dot ground-state (s wave) orbital wavefunctions $\varphi(\mathbf{r})$ and combines them into the (anti-) symmetric two-particle orbital state vector

$$|\Psi_\pm\rangle = \frac{|12\rangle \pm |21\rangle}{\sqrt{2(1 \pm S^2)}}, \tag{49}$$

the positive (negative) sign corresponding to the spin singlet (triplet) state, and $S = \int d^2r \varphi^*_{+a}(\mathbf{r})\varphi_{-a}(\mathbf{r}) = \langle 2|1\rangle$ denoting the overlap of the right and left orbitals. A non-vanishing overlap implies that the electrons tunnel between the dots (see also Sec. III.B.3). Here, $\varphi_{-a}(\mathbf{r}) = \langle \mathbf{r}|1\rangle$ and $\varphi_{+a}(\mathbf{r}) = \langle \mathbf{r}|2\rangle$ denote the one-particle orbitals centered at $\mathbf{r} = (\mp a, 0)$, and $|ij\rangle = |i\rangle|j\rangle$ are two-particle product states. The exchange energy is then obtained through $J = \epsilon_{\rm t} - \epsilon_{\rm s} = \langle\Psi_-|H_{\rm orb}|\Psi_-\rangle - \langle\Psi_+|H_{\rm orb}|\Psi_+\rangle$. The single-dot orbitals for harmonic confinement in two dimensions in a perpendicular magnetic field are the Fock-Darwin states (Darwin, 1930; Fock, 1928), which are the usual harmonic oscillator states, magnetically compressed by a factor $b = \omega/\omega_0 = \sqrt{1 + \omega_{\rm L}^2/\omega_0^2}$, where $\omega_{\rm L} = eB/2mc$ denotes the Larmor frequency. The ground state (energy $\hbar\omega = b\hbar\omega_0$) centered at the origin is

$$\varphi(x, y) = \sqrt{\frac{m\omega}{\pi\hbar}} e^{-m\omega\left(x^2+y^2\right)/2\hbar}. \tag{50}$$

Shifting the single particle orbitals to $(\pm a, 0)$ in the presence of a magnetic field we obtain $\varphi_{\pm a}(x, y) = \exp(\pm iya/2l_B^2)\varphi(x \mp a, y)$, where the phase factor involving the magnetic length $l_B = \sqrt{\hbar c/eB}$ is due to the gauge transformation $\mathbf{A}_{\pm a} = B(-y, x \mp a, 0)/2 \to \mathbf{A} = B(-y, x, 0)/2$. We obtain (Burkard *et al.*, 1999a)

$$J = \frac{2S^2}{1 - S^4}\left(\langle 12|C + W|12\rangle - \frac{{\rm Re}\langle 12|C + W|21\rangle}{S^2}\right), \tag{51}$$

where the overlap becomes $S = \exp(-m\omega a^2/\hbar - a^2\hbar/4l_B^4 m\omega)$. Evaluation of the matrix elements of C and W yields

$$J = \frac{\hbar\omega_0}{\sinh\left(2d^2(2b - \frac{1}{b})\right)}\left[c\sqrt{b}\Big(e^{-bd^2}{\rm I}_0(bd^2) - e^{d^2(b-1/b)}{\rm I}_0(d^2\{b - \frac{1}{b}\})\Big) + \frac{3}{4b}\left(1 + bd^2\right)\right], \tag{52}$$

where we introduce the dimensionless distance $d = a/a_{\rm B}$, and $\rm I_0$ is the zeroth order Bessel function. The first and second terms in Eq. (52) are due to the Coulomb interaction C, where the exchange term enters with a minus sign. The parameter $c = \sqrt{\pi/2}(e^2/\kappa a_{\rm B})/\hbar\omega_0$ (≈ 2.4, for $\hbar\omega_0 = 3\,{\rm meV}$) is the ratio between Coulomb and confining energy. The last term comes from the confinement potential W. The result $J(B)$ is plotted in Fig. 8 (dashed line). Note that typically $|J/\hbar\omega_0| \lesssim 0.2$. Also, we see that $J > 0$ for $B = 0$, which must be the case for a two-particle system that is time-reversal invariant (Mattis, 1988). The most remarkable feature of $J(B)$, however, is the change of sign from positive to negative at $B = B_*^{\rm s}$, which occurs over a wide range of parameters c and a. This singlet-triplet crossing occurs at about $B_*^{\rm s} = 1.3\,{\rm T}$ for $\hbar\omega_0 = 3\,{\rm meV}$ ($c = 2.42$) and $d = 0.7$. The transition from antiferromagnetic ($J > 0$) to ferromagnetic ($J < 0$) spin-spin coupling with increasing magnetic field is caused by the long-range Coulomb interaction, in particular by the negative exchange term, the second term in Eq. (52). As $B \gg B_0$ ($\approx 3.5\,{\rm T}$ for

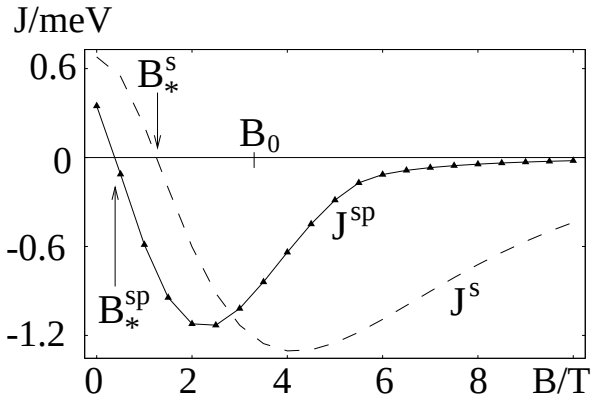


FIG. 8 Exchange energy J in units of meV plotted against the magnetic field B (in units of Tesla), as obtained from the s-wave Heitler-London approximation (dashed line), Eq. (52), and the result from the improved sp-hybridized Heitler-London approximation (triangles) which is obtained numerically as explained in the text. Note that the qualitative behavior of the two curves is similar, i.e. they both have zeroes, the s-wave approximation at $B_*^{\rm s}$, and the sp-hybridized approximation at $B_*^{\rm sp}$, and also both curves vanish exponentially for large fields. $B_0 = (\hbar\omega_0/\mu_{\rm B})(m/m_e)$ denotes the crossover field to magnetically dominated confining ($B \gg B_0$). The curves are given for a confinement energy $\hbar\omega_0 = 3\,$meV (implying for the Coulomb parameter $c = 2.42$), and inter-dot distance $a = 0.7\,a_{\rm B}$.

$\hbar\omega_0 = 3\,$meV), the magnetic field compresses the orbits by a factor $b \approx B/B_0 \gg 1$ and thereby reduces the overlap of the wavefunctions, $S^2 \approx \exp(-2d^2(2b-1/b))$, exponentially strongly. Similarly, the overlap decays exponentially for large inter-dot distances, $d \gg 1$. Note however, that this exponential suppression is partly compensated by the exponentially growing exchange term $\langle 12|C|21\rangle/S^2 \propto \exp(2d^2(b-1/b))$. As a result, the exchange coupling J decays exponentially as $\exp(-2d^2 b)$ for large b or d, as shown in Fig. 9b for $B = 0$ ($b = 1$). Thus, the exchange coupling J can be tuned through zero and then suppressed to zero by a magnetic field in a very efficient way.

2. Limitations and extensions of HL

We note that the HL approximation breaks down explicitly (i.e. J becomes negative even when $B = 0$) for certain inter-dot distances if the interaction becomes too strong (c exceeds ≈ 2.8).

The HL method can be improved by taking into account more than one single-dot orbital. Admixture of higher orbitals can be taken into account using a variational approach; the orbitals obtained in this way are termed *hybridized* orbitals, in analogy to hybridized molecular orbitals in chemistry. Some results obtained with sp-hybridized QD orbitals are plotted in Fig. 8.

Another limitation of the HL approximation its restriction to quantum dots that are occupied with a single electron. Even with a single orbital, the Pauli principle allows for the presence of a second electron with opposite spin on a QD orbital. While this admixture of double occupancy is suppressed by the repulsive Coulomb interaction between electrons, it nevertheless plays a relevant role.

3. The Hund-Mulliken approach and the Hubbard Limit

The Hund-Mulliken (HM) approximation (also known as molecular orbit approximation (Mattis, 1988)) extends the HL approach by including also the two doubly occupied states, which both are spin singlets (Burkard *et al.*, 1999a). This extends the orbital Hilbert space from two to four dimensions. First, the single particle states have to be orthonormalized, leading to the states $\Phi_{\pm a} = (\varphi_{\pm a} - g\varphi_{\mp a})/\sqrt{1-2Sg+g^2}$, where S again denotes the overlap of φ_{-a} with φ_{+a} and $g = (1-\sqrt{1-S^2})/S$. Then, diagonalization of

$$H_{\rm orb} = 2\epsilon + \begin{pmatrix} U & X & -\sqrt{2}t_{\rm H} & 0 \\ X & U & -\sqrt{2}t_{\rm H} & 0 \\ -\sqrt{2}t_{\rm H} & -\sqrt{2}t_{\rm H} & V_+ & 0 \\ 0 & 0 & 0 & V_- \end{pmatrix} \tag{53}$$

in the space spanned by $\Psi^{\rm d}_{\pm a}(\mathbf{r}_1,\mathbf{r}_2) = \Phi_{\pm a}(\mathbf{r}_1)\Phi_{\pm a}(\mathbf{r}_2)$, $\Psi^{\rm s}_{\pm}(\mathbf{r}_1,\mathbf{r}_2) = [\Phi_{+a}(\mathbf{r}_1)\Phi_{-a}(\mathbf{r}_2) \pm \Phi_{-a}(\mathbf{r}_1)\Phi_{+a}(\mathbf{r}_2)]/\sqrt{2}$ yields the eigenvalues $\epsilon_{\rm s\pm} = 2\epsilon + U_{\rm H}/2 + V_+ \pm \sqrt{U_{\rm H}^2/4 + 4t_{\rm H}^2}$, $\epsilon_{\rm s0} = 2\epsilon + U_{\rm H} - 2X + V_+$ (singlet), and $\epsilon_{\rm t} = 2\epsilon + V_-$ (triplet), where the quantities are given in (Burkard *et al.*, 1999a). The exchange energy then becomes

$$J = \epsilon_{\rm t} - \epsilon_{\rm s-} = V - \frac{U_{\rm H}}{2} + \frac{1}{2}\sqrt{U_{\rm H}^2 + 16t_{\rm H}^2}. \tag{54}$$

In the standard Hubbard approach for short-range Coulomb interactions (and without B-field) (Mattis, 1988) J reduces to $-U/2 + \sqrt{U^2+16t^2}/2$, where t denotes the hopping matrix element, and U the on-site repulsion. Thus,

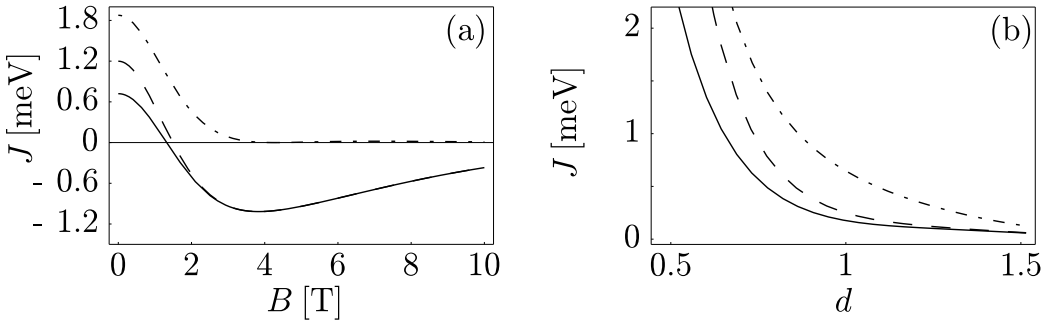


FIG. 9 The exchange coupling J obtained from HM (full line), Eq. (54), and from the extended Hubbard approximation (dashed line), Eq. (55). For comparison, we also plot the usual Hubbard approximation where the long-range interaction term V is omitted, i.e. $J = 4t_{\rm H}^2/U_{\rm H}$ (dashed-dotted line). In (a), J is plotted as a function of the magnetic field B at fixed inter-dot distance ($d = a/a_{\rm B} = 0.7$), and for $c = 2.42$, in (b) as a function of inter-dot distance $d = a/a_{\rm B}$ at zero field ($B = 0$), and again $c = 2.42$. For these parameter values, the s-wave Heitler-London J, Eq. (52), and the HM J (full line) are almost identical.

$t_{\rm H}$ and $U_{\rm H}$ are the extended hopping matrix element and the on-site repulsion, resp., renormalized by long-range Coulomb interactions. The remaining two singlet energies $\epsilon_{\rm s+}$ and $\epsilon_{\rm s0}$ are separated from $\epsilon_{\rm t}$ and $\epsilon_{\rm s-}$ by a gap of order $U_{\rm H}$ and are therefore neglected for the study of low-energy properties. Typically, the "Hubbard ratio" $t_{\rm H}/U_{\rm H}$ is less than 1, e.g., if $d = 0.7$, $\hbar\omega_0 = 3\,$meV, and $B = 0$, we obtain $t_{\rm H}/U_{\rm H} = 0.34$, and it decreases with increasing B. Therefore, we are in an *extended* Hubbard limit, where J takes the form

$$J = \frac{4t_{\rm H}^2}{U_{\rm H}} + V. \tag{55}$$

The first term has the form of the standard Hubbard approximation (Fradkin, 1991) but with $t_{\rm H}$ and $U_{\rm H}$ being renormalized by long-range Coulomb interactions. The second term V is new and accounts for the difference in Coulomb energy between the singly occupied singlet and triplet states $\Psi_{\pm}^{\rm s}$. It is precisely this V that makes J negative for high magnetic fields, whereas $t_{\rm H}^2/U_{\rm H} > 0$ for all values of B (see Fig. 9a). Thus, the usual Hubbard approximation (i.e. without V) would not give reliable results, neither for the B-dependence (Fig. 9a) nor for the dependence on the inter-dot distance a (Fig. 9b). Since only the singlet space has been enlarged, it is clear that we obtain a lower singlet energy $\epsilon_{\rm s}$ than that from the s-wave Heitler-London calculation, but the same triplet energy $\epsilon_{\rm t}$, and therefore $J = \epsilon_{\rm t} - \epsilon_{\rm s}$ exceeds the s-wave Heitler-London result, Eq. (52). However, the on-site Coulomb repulsion $U \propto c$ strongly suppresses the doubly occupied states $\Psi_{\pm a}^{\rm d}$ and already for the value of $c = 2.4$ (corresponding to $\hbar\omega_0 = 3$meV) we obtain almost perfect agreement with the s-wave Heitler-London result (Fig. 8). For large fields, i.e. $B \gg B_0$, the suppression becomes even stronger ($U \propto \sqrt{B}$) because the electron orbits become compressed with increasing B and two electrons on the same dot are confined to a smaller area leading to an increased Coulomb energy. Being a completely orbital effect, the exchange interaction between spins of course competes with the Zeeman coupling H_Z of the spins to the magnetic field. In our case, however, the Zeeman energy H_Z is small and exceeds the exchange energy (polarizing the spins) only in a narrow window (about 0.1 T wide) around $B_*^{\rm sp}$ and again for high fields ($B > 4\,$T).

4. Numerical work

While the calculation discussed in Sec. III.B.3 above take only the ground-state orbital in each QD into account, the HM, like the HL, approximation can be refined to include more orbital levels of the QDs. Such extended calculations are usually done numerically, and are very closely related to Hartree-Fock (HF) calculations. Note, however, that HF is not sufficient for the purpose of calculating a spin exchange coupling, since it is not capable of including entangled (quantum correlated) states such as the spin singlet or $m = 0$ triplet. This is typically remedied by invoking the so-called configuration-interaction method which includes linear superpositions of HF states. Numerical studies of the double-dot system with one (Hu and Das Sarma, 2000) and three (Hu and Das Sarma, 2001) electrons per QD showed good agreement with the somewhat more crude approximations discussed above.

At finite magnetic field, the exchange coupling Eq. (52) can be tuned through zero by changing electrostatic properties (QD size, distance, electric field). It has been confirmed both numerically and in actual experiment

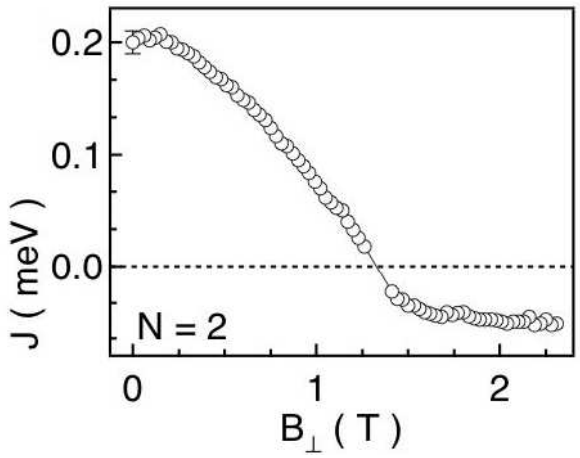


FIG. 10 The exchange coupling J measured as a function of the applied magnetic field $B_\perp$ using conductance spectroscopy in a two-electron dot system defined in a GaAs/AlGaAs heterostructure. There are signatures that a double has been formed although a single dot structure was used in the experiment (Zumbühl *et al.*, 2004). The shape of the dot is not circular, but somewhat elongated. The dot spectra appear to be consistent with a parabolic potential with harmonic energies $\hbar\omega_a = 1.2\,\mathrm{meV}$ and $\hbar\omega_b = 3.3\,\mathrm{meV}$, corresponding to a spatial elongation of $\sqrt{\omega_b/\omega_a} \sim 1.6$. (Figure courtesy of D. M. Zumbühl, Harvard University).

(Kyriakidis *et al.*, 2002) that singlet-triplet crossings can be induced in a single QD by changes in the dot potential at constant magnetic field.

5. Measurements of QD exchange

Signatures of singlet-triplet crossings have been observed using transport spectroscopy in lateral GaAs quantum dot structures (Zumbühl *et al.*, 2004) (see Fig. 10). Although a single dot structure was used, there are signatures that a double dot was formed in the experiment (Engel *et al.*, 2004).

These data seem to be in rather good qualitative agreement with theory (Burkard *et al.*, 1999a), bearing in mind that the absolute magnitude of the exchange coupling J strongly depends on the inter-dot distance which is a free parameter of the theory. Similar double-dot experiments with the double-dot systems shown in Fig. 6 are in preparation.

C. Exchange in vertically coupled QDs

While lateral QDs are adjacent to each other in a two-dimensional electron gas, vertically coupled QDs are stacked on top of each other in a three-dimensional semiconductor structure. Vertical coupling occurs both in QDs etched out of multilayer structures and electrically gated (Austing *et al.*, 1998) and in self-assembled QDs originating from the Stranski-Krastanov growth (Fafard *et al.*, 1999; Fricke *et al.*, 1996; Luyken *et al.*, 1998). A system of vertically coupled QDs is shown schematically in Fig. 11. There are a number of works on the exchange coupling between spins located in this type of coupled QDs (Burkard *et al.*, 2000c; Imamura *et al.*, 1998, 1996, 1999; Oh *et al.*, 1996; Tokura *et al.*, 1999). This Section in devoted to the exchange coupling between spins in vertically coupled dots under the influence of both in-plane magnetic and electric fields, $B_\parallel$ and $E_\parallel$, and perpendicular fields $B_\perp$, $E_\perp$ (Burkard *et al.*, 2000c). Electronic spectra and charge densities for two electrons in a system of vertically tunnel-coupled QDs at zero magnetic field, $\mathbf{B} = 0$, were calculated in (Bryant, 1993). Singlet-triplet crossings in the ground state of single (Wagner *et al.*, 1992; Wojs *et al.*, 1996) and coupled dots with two (Oh *et al.*, 1996) to four (Imamura *et al.*, 1998,

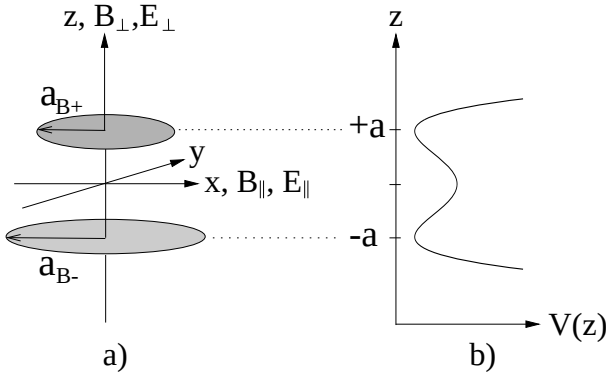


FIG. 11 (a) Sketch of the vertically coupled double quantum-dot system. The two dots may have different lateral diameters, a_{B+} and a_{B-}. We consider magnetic and electric fields applied either in-plane ($B_\parallel$, $E_\parallel$) or perpendicularly ($B_\perp$, $E_\perp$). (b) The model potential for the vertical confinement is a double well, which is obtained by combining two harmonic wells at $z = \pm a$.

1996, 1999; Tokura *et al.*, 1999) electrons in vertically coupled dots in the presence of a magnetic field perpendicular to the growth direction ($B_\perp$ in Fig. 11) have been predicted. In order to apply the HL and HM methods introduced in Sec. III.B to vertically coupled QDs, a Hamiltonian of the same form as Eq. (45) can be used, but with the single-particle Hamiltonian replaced by (Burkard *et al.*, 2000c)

$$h(\mathbf{r},\mathbf{p}) = \frac{1}{2m}\left(\mathbf{p} - \frac{e}{c}\mathbf{A}(\mathbf{r})\right)^2 + ezE + V_l(\mathbf{r}) + V_v(\mathbf{r}). \tag{56}$$

Also note that $\mathbf{r}$ is a three-dimensional vector here, as opposed to a two-dimensional vector in Sec. III.B. The potential V_l in h describes the lateral confinement, whereas V_v models the vertical double-well structure. For the lateral confinement the parabolic potential

$$V_l(x,y) = \frac{m}{2}\omega_z^2 \begin{cases} \alpha_{0+}^2(x^2+y^2), & z>0, \\ \alpha_{0-}^2(x^2+y^2), & z<0, \end{cases} \tag{57}$$

is chosen, where we have introduced the anisotropy parameters $\alpha_{0\pm}$ determining the strength of the vertical relative to the lateral confinement. In the presence of a magnetic field $B_\perp$ perpendicular to the 2DES, the one-particle problem has the Fock-Darwin states (Darwin, 1930; Fock, 1928) as an exact solution. Furthermore, it has been shown experimentally (Fricke *et al.*, 1996) and theoretically (Wojs *et al.*, 1996) that a two-dimensional harmonic confinement potential is a reasonable approximation to the real confinement potential in a lens-shaped SAD. In describing the confinement V_v along the inter-dot axis, a (locally harmonic) double well potential of the form (see Fig. 11b)

$$V_v = \frac{m\omega_z^2}{8a^2}\left(z^2-a^2\right)^2, \tag{58}$$

can be used; in the limit of large inter-dot distance $a \gg a_\mathrm{B}$, the potential V_v in the vicinity of $z \approx \pm a$ becomes a harmonic well of frequency ω_z. Here a is half the distance between the centers of the dots and $a_B = \sqrt{\hbar/(m\omega_z)}$ is the vertical effective Bohr radius. For most vertically coupled dots, the vertical confinement is determined by the conduction band offset between different semiconductor layers; therefore in principle a square-well potential would be a more accurate description of the real potential than the harmonic double well (note however, that the required conduction-band offsets are not always known exactly). There is no qualitative difference between the results presented below obtained with harmonic potentials and the corresponding results obtained using square-well potentials (Seelig, 1999).

1. Perpendicular Magnetic Field $B_\perp$

For a magnetic field $B = B_\perp$ (cf. Fig. 11) and $E = 0$, one obtains the ground-state Fock-Darwin (Darwin, 1930; Fock, 1928) solution

$$\varphi_{\pm a}(x,y,z) = \left(\frac{m\omega_z}{\pi\hbar}\right)^{3/4}\sqrt{\alpha_\pm}\, e^{-m\omega_z\left(\alpha_\pm\left(x^2+y^2\right)+(z\mp a)^2\right)/2\hbar}, \tag{59}$$

corresponding to the ground-state energy $\epsilon_\pm = \hbar\omega_z(1+2\alpha_\pm)/2$. In Eq. (59) we have introduced $\alpha_\pm(\mathrm{B}) = \sqrt{\alpha_{0\pm}^2 + \omega_L(B)^2/\omega_z^2} = \sqrt{\alpha_{0\pm}^2 + B^2/B_0^2}$, with $\omega_L(B) = eB/2mc$ the Larmor frequency and $B_0 = 2mc\omega_z/e$ the magnetic field for which $\omega_z = \omega_L$. The parameters $\alpha_\pm(B)$ describe the compression of the one-particle wave function perpendicular to the magnetic field. The HL with this Hamiltonian yields

$$\begin{aligned} J \;=\; & \frac{2S^2}{1-S^4}\hbar\omega_z\Bigg[c\sqrt{\mu}\, e^{2\mu d^2}\left(1-\mathrm{erf}\left(d\sqrt{2\mu}\right)\right) - \frac{c}{\pi}\frac{\alpha_+ + \alpha_-}{\sqrt{1-(\alpha_+ + \alpha_- - 1)^2}}\arccos(\alpha_+ + \alpha_- - 1) \\ & + \frac{1}{4}\left(\alpha_{0+}^2 - \alpha_{0-}^2\right)\left(\frac{\alpha_+ - \alpha_-}{\alpha_+\alpha_-}\right)(1-\mathrm{erf(d)}) + \frac{3}{4}\left(1+d^2\right)\Bigg], \end{aligned} \tag{60}$$

where $\mathrm{erf}(x)$ denotes the error function. We have introduced the dimensionless parameters $d = a/a_B$ for the inter-dot distance, and $c = \sqrt{\pi/2}(e^2/\kappa a_\mathrm{B})/\hbar\omega_z$ for the Coulomb interaction. Note that $\alpha_\pm$, $\mu = 2\alpha_+\alpha_-/(\alpha_+ + \alpha_-)$, and the overlap

$$S = 2\frac{\sqrt{\alpha_+\alpha_-}}{\alpha_+ + \alpha_-}\exp(-d^2), \tag{61}$$

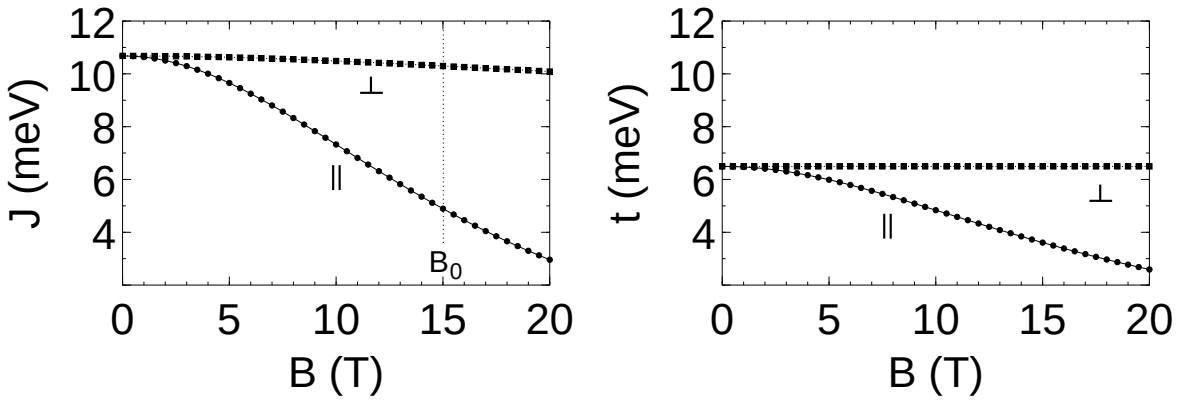


FIG. 12 Exchange energy J (left graph) and single-electron tunneling amplitude t (right graph) as a function of the applied magnetic field for two vertically coupled small (height 6 nm, width 12 nm) InAs ($m = 0.08m_e$, $\kappa = 14.6$) self-assembled QDs in a center-to-center distance of 9 nm ($d = 1.5$). The box-shaped symbols correspond to the magnetic field $B_\perp$ applied in z direction, the circle symbols to the field $B_\parallel$ in x direction. The plotted results were obtained using the HM method and are reliable up to a field $B_0 \approx 15$ T where higher levels start to become important.

depend on the magnetic field B. The first term in the square brackets in Eq. (60) is an approximate evaluation of the direct Coulomb integral $\langle 12|C|12\rangle$ for $d \gtrsim 0.7$ and for magnetic fields $B \lesssim B_0$. The second term in Eq. (60) is the (exact) exchange Coulomb integral $\langle 12|C|21\rangle/S^2$, while the last two terms stem from the potential integrals, which were also evaluated exactly. If the two dots have the same size, the expression for the exchange energy Eq. (60) can be simplified considerably.

For two vertically coupled dots of equal size, we set $\alpha_{0+} = \alpha_{0-} \equiv \alpha_0$ in Eq. (60) and using Eq. (61), we obtain

$$J = \frac{\hbar\omega_z}{\sinh(2d^2)}\left[c\sqrt{\alpha}e^{2\alpha d^2}\left(1-\mathrm{erf}\left(d\sqrt{2\alpha}\right)\right) - \frac{c}{\pi}\frac{2\alpha}{\sqrt{1-(2\alpha-1)^2}}\arccos(2\alpha-1) + \frac{3}{4}\left(1+d^2\right)\right], \tag{62}$$

where $\alpha = \sqrt{\alpha_0^2 + B^2/B_0^2}$. As before, the first term in Eq. (62) is the direct Coulomb term, while the second term (appearing with a negative sign) is the exchange Coulomb term. Finally, the potential term in this case equals $W = (3/4)(1+d^2)$ and is due to the vertical confinement only. For two dots of equal size neither the prefactor $2S^2/(1-S^4)$ nor the potential term depends on the magnetic field. Since the direct Coulomb term depends on $B_\perp$ only weakly, the field dependence of the exchange energy is mostly determined by the exchange Coulomb term. The exchange coupling can also be calculated using the HM method (Burkard *et al.*, 2000c).

The dependence of the exchange energy J on an electric field $E_\perp$ applied in parallel to the magnetic field, i.e. perpendicular to the xy plane, withing the HL approximation, was found to be

$$J(B, E_\perp) = J(B,0) + \hbar\omega_z \frac{2S^2}{1-S^4}\frac{3}{2}\left(\frac{E_\perp}{E_0}\right)^2, \tag{63}$$

where $E_0 = m\omega_z^2/ea_B$. The growth of J is thus proportional to the square of the electric field $E_\perp$, if the field is not too large. This result is supported by a HM calculation, yielding the same field dependence at small electric fields, whereas if $eE_\perp a$ is larger than U_H, double occupancy must be taken into account. The electric field causes the exchange J at a constant magnetic field B to cross through zero from $J(E=0,B) < 0$ to $J > 0$. This effect is signaled by a change in the magnetization M (Burkard *et al.*, 2000c).

2. In-plane magnetic field $B_\parallel$

In this section we consider two dots of equal size in a magnetic field $B_\parallel$ which is applied along the x-axis, i.e. *in-plane* (see Fig. 11). Since the two dots have the same size, the lateral confining potential Eq. (III.B) reduces to $V(x,y) = m\omega_z^2\alpha_0^2(x^2+y^2)/2$, where the parameter α_0 describes the ratio between the lateral and the vertical confinement energy. The vertical double-dot structure is modeled using the potential Eq. (58). The situation for an in-plane field is a bit more complicated than for a perpendicular field, because the planar and vertical motion do not separate. In order to find the ground-state wave function of the one-particle Hamiltonian $h^0_{\pm a}$, an approximate

variational method can be applied (Burkard *et al.*, 2000c) with the result

$$\varphi_{\pm a} = \left(\frac{m\omega_z}{\pi\hbar}\right)^{\frac{3}{4}} (\alpha_0\alpha\beta)^{\frac{1}{4}} \exp\left[-\frac{m\omega_z}{2\hbar}\left(\alpha_0 x^2 + \alpha y^2 + \beta(z \mp a)^2\right) \pm i\frac{ya}{2l_B^2}\right], \tag{64}$$

where the parameters $\alpha(B) = \sqrt{\alpha_0^2 + (B/B_0)^2}$ and $\beta(B) = \sqrt{1 + (B/B_0)^2}$, describing the wave-function compression in y and z direction, respectively, have been introduced.

The resulting exchange coupling J in this case is

$$J(B,d) = J_0(B,d) - \hbar\omega_z \frac{4S^2}{1-S^4}\frac{\beta-\alpha}{\alpha} d^2 \left(\frac{B}{B_0}\right)^2, \tag{65}$$

where J_0 denotes the expression from Eq. (51). The variation of the exchange energy J as a function of the magnetic field B is, through the prefactor $2S^2/(1-S^4)$, determined by the overlap $S(B,d) = \exp[-d^2(\beta(B)+(B/B_0)^2)/\alpha(B)]$, depending exponentially on the in-plane field, while for a perpendicular field the overlap is independent of the field (for two dots of equal size), see Eq. (61). The HL result can again be improved by performing a molecular-orbital (HM) calculation of the exchange energy, which we plot in Fig. 12 (left graph, circle symbols).

3. Electrical switching of the interaction

Operating a coupled quantum dot as a quantum gate requires the ability to switch on and off the interaction between the electron spins on neighboring dots. A simple method of achieving a high-sensitivity switch for vertically coupled dots involves a horizontally applied electric field $E_\parallel$. The idea is to use a pair of QDs with different lateral sizes, e.g. a small dot on top of a large dot ($\alpha_{0+} > \alpha_{0-}$, see Fig. 11). Note that only the radius in the xy plane has to be different, while it can be assumed that the dots have the same height. Applying an in-plane electric field $E_\parallel$ in this case causes a shift of the single-dot orbitals by $\Delta x_\pm = eE_\parallel/m\omega_z^2\alpha_{0\pm}^2 = E_\parallel/E_0\alpha_{0\pm}^2$, where $E_0 = \hbar\omega_z/ea_B$, see Fig. 13. It is clear that the electron in the larger dot moves further in the (reversed) direction of the electric field ($\Delta x_- > \Delta x_+$), since its confinement potential is weaker. As a result, the mean distance between the two electrons changes from $2d$ to $2d'$, where

$$d' = \sqrt{d^2 + \frac{1}{4}\left(\Delta x_- - \Delta x_+\right)^2} = \sqrt{d^2 + A^2\left(\frac{E_\parallel}{E_0}\right)^2}, \tag{66}$$

with $A = (1/\alpha_{0-}^2 - 1/\alpha_{0+}^2)/2$. Using Eq. (61), we find that the wavefunction overlap scales as $S \propto \exp(-d'^2) \propto \exp[-A^2(E_\parallel/E_0)^2]$. Due to this high sensitivity, the electric field is an ideal "switch" for the exchange coupling J which is (asymptotically) proportional to S^2 and thus decreases exponentially on the scale $E_0/2A$. Note that if the dots have exactly the same size, then $A = 0$ and the effect vanishes. An estimate of J as a function of $E_\parallel$ can be obtained by substituting d' from Eq. (66) into the HL result, Eq. (60). A plot of $J(E_\parallel)$ obtained in this way is shown in Fig. 13 for a specific choice of GaAs dots. Note that this procedure is not exact, since it neglects the tilt of the orbitals with respect to their connecting line. Exponential switching is highly desirable for quantum computation, because in the "off" state of the switch, fluctuations in the external control parameter (e.g. the electric field $E_\parallel$) or charge fluctuations cause only exponentially small fluctuations in the coupling J. If this were not the case, the fluctuations in J would lead to uncontrolled coupling between qubits and therefore to multiple-qubit errors. Such correlated errors cannot be corrected by known error-correction schemes, which are designed for uncorrelated errors (Preskill, 1998b).

D. Single-qubit operations

Single-qubit operations with the Hamiltonian Eq. (10) require a time-varying Zeeman coupling $(g\mu_B\mathbf{S}\cdot\mathbf{B})(t)$ (Burkard *et al.*, 1999a; Loss and DiVincenzo, 1998), which can be controlled by changing the magnetic field $\mathbf{B}$ or the g-factor g. Effective magnetic fields/g-factors can be produced by coupling the spin via exchange to a ferromagnet (Loss and DiVincenzo, 1998) or to polarized nuclear spins (Burkard *et al.*, 1999a). We review here how the g-factor of an electron in a semiconductor heterostructure can be modulated by shifting its orbital between layers of host material with different g-factors (DiVincenzo *et al.*, 1999; DiVincenzo and Loss, 1999).

The spin-orbit coupling can leads to large deviations of the Landé g-factor (both in the positive and negative direction) in bulk semiconductors from the free-electron value $g_0 = 2.0023$. The effective g-factors in these materials

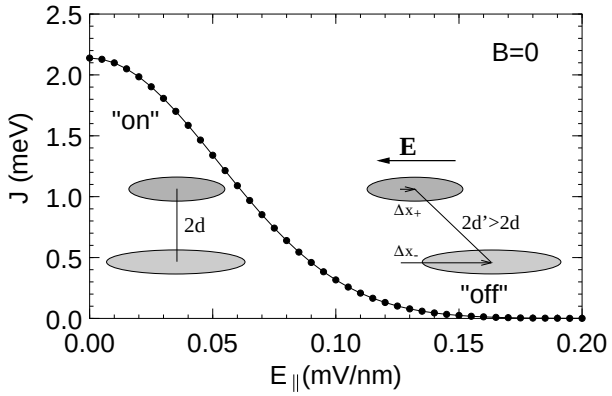


FIG. 13 Controlled switching of the exchange coupling J between dots of different size by means of an in-plane electric field $E_\parallel$ at zero magnetic field, $B = 0$. The coupling is "on" at $E = 0$. When $E_\parallel$ is applied, the larger dot is shifted to the right by Δx_-, whereas the smaller dot is shifted by $\Delta x_+ < \Delta x_-$, where $\Delta x_\pm = E_\parallel/E_0\alpha_{0\pm}^2$ and $E_0 = \hbar\omega_z/ea_B$. With $E_\parallel$ increasing, J decreases exponentially, $J \approx S^2 \approx \exp[-2A^2(E_\parallel/E_0)^2]$. The parameters used for this plot are $\hbar\omega_z = 7\,\mathrm{meV}$, $d = 1$, $\alpha_{0+} = 1/2$ and $\alpha_{0-} = 1/4$, yielding $E_0 = \hbar\omega_z/ea_B = 0.56\,\mathrm{mV/nm}$ and $A = (\alpha_{0+}^2 - \alpha_{0-}^2)/2\alpha_{0+}^2\alpha_{0-}^2 = 6$. The coupling J decreases exponentially on the scale $E_0/2A = 0.047\,\mathrm{mV/nm}$ for the electric field.

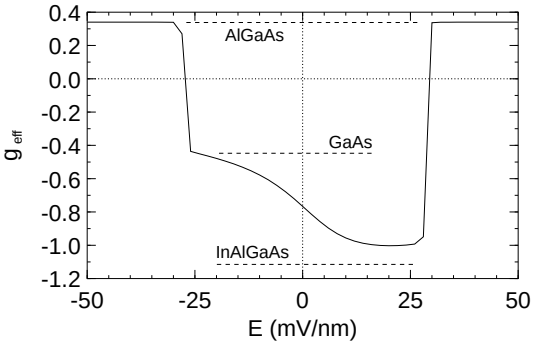


FIG. 14 Effective g-factor g_{eff} of electrons confined in a $\mathrm{Al}_x\mathrm{Ga}_{1-x}\mathrm{As}$–GaAs–$\mathrm{In}_y\mathrm{Al}_x\mathrm{Ga}_{1-x-y}\mathrm{As}$–$\mathrm{Al}_x\mathrm{Ga}_{1-x}\mathrm{As}$ heterostructure ($x = 0.3$, $y = 0.1$) as a function of the applied electric field E in growth direction. The widths of the quantum well and the barriers are $w = w_{\mathrm{B}} = 10\,\mathrm{nm}$. The g-factors which are used for the materials are indicated with dashed horizontal lines.

range from large negative to large positive numbers. In confined structures such as quantum wells, wires, and dots, the g-factor is modified with respect to the bulk value and sensitive to an external bias voltage (Ivchenko *et al.*, 1997). In the case of a layered structure, the effective g-factor of electrons can be varied by electrically shifting their equilibrium position from one layer (with g-factor g_1) to another (with another g-factor $g_2 \neq g_1$). The bulk g-factors of the layer materials and linear interpolations between them, have been used here as an approximation which becomes increasingly inaccurate as the layers become thinner (Kiselev *et al.*, 1998).

Let us assume that by replacing some fraction y of Ga atoms in the upper half of a AlGaAs-GaAs-AlGaAs quantum well by In atoms (we have used $y = 0.1$) we obtain the following layered heterostructure:

$$\mathrm{Al}_x\mathrm{Ga}_{1-x}\mathrm{As}\text{–GaAs–}\mathrm{In}_y\mathrm{Al}_x\mathrm{Ga}_{1-x-y}\mathrm{As}\text{–}\mathrm{Al}_x\mathrm{Ga}_{1-x}\mathrm{As},$$

where x denotes the Al content in the barriers (typically around 30%). In such a structure, the effective g-factor can be modified by changing the vertical position of the electrons via top or back gates. If the electron is mostly in a pure GaAs environment, then its effective g-factor will be around the GaAs bulk value ($g_{\mathrm{GaAs}} = -0.44$) whereas if the electron is in the InAlGaAs region, the g-factor will be more negative due to the large negative InAs value ($g_{\mathrm{InAs}} = -15$). The one-dimensional problem of one electron in such a structure has been analyzed numerically. When the effective mass $m(z)$ is spatially varying, the Hamiltonian in the effective mass approximation can be written as

$$\left[-\frac{d}{dz}\frac{\hbar^2}{2m(z)}\frac{d}{dz} + V(z)\right]\Psi(z) = E\Psi(z). \tag{67}$$

This problem can be discretized in real space and subsequently diagonalized numerically (DiVincenzo *et al.*, 1999). Finally, the effective g-factor is calculated by averaging the local g-factor $g(z)$ over the electronic density in the ground-state (see Fig. 14),

$$g_{\mathrm{eff}} = \int dz g(z)|\Psi(z)|^2. \tag{68}$$

The option of performing single-qubit rotations by electrostatically controlling the g-factor makes all-electric control of a spin-based quantum computer (an array of QDs as in Fig. 1) possible and thus offers a way around the problematic local magnetic field implementation of single-qubit gates. Another method to circumvent single-spin operations completely (however, at a higher cost of gates and exchange operations) is the exchange-only architecture outlined in Sec. II.C.

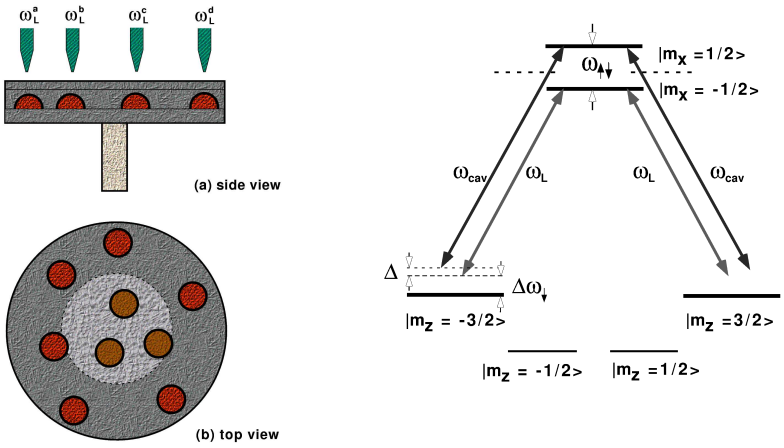


FIG. 15 Left: QDs embedded inside a microdisk structure, from (Imamoğlu *et al.*, 1999). Each QD is addressed selectively by a laser field from a fiber-tip. The laser frequencies are chosen to select out the pair of QDs that will participate in gate operation. All dots strongly couple to a single cavity-mode. Right: Energy levels of a III-V (or II-VI) semiconductor QD. It is assumed that confinement along the z-direction is strongest.

E. Semiconductor microcavities

Here, we present a modification of the Loss-DiVincenzo scheme (Sec. II.A) for QC based on QD electron spins. In contrast to the original scheme (Loss and DiVincenzo, 1998), where the spins are coupled via direct exchange, this coupling which is mediated through a single microcavity mode and uses laser fields to mediate coherent interactions between distant QD spins (Imamoğlu *et al.*, 1999).

The cavity scheme is shown in Fig. 15: the doped QDs are embedded in a microdisk structure with diameter $d \simeq 2\,\mu$m and thickness $d \simeq 0.1\,\mu$m. Experiments have shown that InAs self-assembled QDs can be embedded in microdisk structures with a cavity quality factor $Q \simeq 12000$ (Gerard and Gayral, 1999). It is assumed that the QDs are designed such that the quantum confinement along the z-direction is the strongest. The in-plane confinement is also assumed to be large enough to guarantee that the electron will always be in the ground-state orbital. Because of the strong z-axis confinement, the lowest energy eigenstates of such a III-V or II-VI semiconductor QD consist of $|m_z = \pm 1/2\rangle$ conduction-band states and $|m_z = \pm 3/2\rangle$ valence-band states. The QDs are doped such that each QD has a full valence band and a single conduction band electron: we assume that a uniform magnetic field along the x-direction (B_x) is applied, so the QD qubit is defined by the conduction-band states $|m_x = -1/2\rangle = |\downarrow\rangle$ and $|m_x = 1/2\rangle = |\uparrow\rangle$ (Fig. 15, right).

1. Single-qubit operations

Single-bit operations are carried out in this scheme by applying two laser fields $E_{L,x}(t)$ and $E_{L,y}(t)$ with Rabi frequencies $\Omega_{L,x}$ and $\Omega_{L,y}$, and frequencies $\omega_{L,x}$ and $\omega_{L,y}$ (polarized along the x and y directions, respectively) that exactly satisfy the Raman-resonance condition between $|\downarrow\rangle$ and $|\uparrow\rangle$. The laser fields are turned on for a short time duration that satisfies a π/r-pulse condition, where r is any real number. The process can be best understood as a Raman π/r-pulse for the *hole* in the conduction band state. The laser field polarizations should have non-parallel components in order to create a non-zero Raman coupling (if there is no heavy-hole light-hole mixing). These arbitrary single-bit rotations can naturally be carried out in parallel. In addition, the QDs that are not doped by a single electron never couple to the Raman fields and can safely be ignored.

2. Two-qubit operations

Two-qubit operations are mediated by virtual photons that are emitted to and reabsorbed from the microcavity field. It is assumed that the x-polarized cavity-mode with energy $\omega_{\rm cav}$ ($\hbar = 1$) and a laser field (assumed to be y-polarized) establish the Raman transition between the two conduction-band states, in close analogy with the atomic

cavity-QED schemes (Pellizzari *et al.*, 1995). The Hamiltonian for a single QD is written as $H = H_0 + H_{\rm int}$, with

$$H_0 = \sum_{\sigma=\uparrow,\downarrow,\pm 3/2} \omega_\sigma e^\dagger_\sigma e_\sigma + \omega_{\rm cav} a^\dagger_{\rm cav} a_{\rm cav} + \omega_L a^\dagger_L a_L, \tag{69}$$

where $e_\uparrow$, $e_\downarrow$ annihilate an electron with spin $\uparrow$, $\downarrow$ along the x direction in the conduction band and $e_{\pm 3/2}$ annihilates an electron with spin $\pm 3/2$ along the z direction in the valence band, cf. Fig. 15 (right). The interaction can be written as

$$H_{\rm int} = g\left(a^\dagger_+ e^\dagger_{-3/2} e_{-1/2} - a^\dagger_- e^\dagger_{3/2} e_{1/2} + h.c.\right), \tag{70}$$

where the operators for the circularly polarized light are expressed in terms of the x-polarized cavity mode and the y-polarized laser field, $a_\pm = (a_{\rm cav} \pm i a_L)/\sqrt{2}$, and the conduction-band operators in the z basis can be expressed in terms of those in the x basis, $e_{\pm 1/2} = (e_\downarrow \pm e_\uparrow)/\sqrt{2}$. With $\omega_{-3/2} = \omega_{3/2} \equiv \omega_v$ and the definition $e_v = (e_{-3/2} - e_{3/2})/2$, the following result for the cavity Hamiltonian is obtained,

$$H_{\rm int} = g\left(a^\dagger_{\rm cav} e^\dagger_v e_\uparrow + e^\dagger_\uparrow e_v a_{\rm cav}\right) - ig\left(a^\dagger_L e^\dagger_v e_\downarrow - e^\dagger_\downarrow e_v a_L\right). \tag{71}$$

The valence band states are eliminated by a Schrieffer-Wolff transformation (Madelung, 1978; Schrieffer and Wolff, 1966), $H_{\rm eff} = e^{-S} H e^S$, with

$$S = \frac{g}{\Delta\omega_\uparrow}\left(a^\dagger_{\rm cav} e^\dagger_v e_\uparrow - e^\dagger_\uparrow e_v a_{\rm cav}\right) - i\frac{g}{\Delta\omega_\downarrow}\left(a^\dagger_L e^\dagger_v e_\downarrow + e^\dagger_\downarrow e_v a_L\right), \tag{72}$$

where $\Delta\omega_\uparrow = \omega_\uparrow - \omega_v - \omega_{\rm cav}$ and $\Delta\omega_\downarrow = \omega_\downarrow - \omega_v - \omega_L$. Neglecting all terms $O(g^3)$ and replacing $e^\dagger_v e_v$ by its expectation value $\langle e^\dagger_v e_v\rangle = 1$ and $g a_L$ by $\Omega_L \exp(-i\omega_L t)$ one obtains the effective Hamiltonian

$$H_{\rm eff} \;=\; \omega_{\rm cav} a^\dagger_{\rm cav} a_{\rm cav} + \sum_i \left[\omega^i_{\uparrow\downarrow}\sigma^i_{\uparrow\uparrow} - \frac{g^2_{\rm cav}}{\Delta\omega^i_\uparrow}\,\sigma^i_{\downarrow\downarrow}\, a^\dagger_{\rm cav} a_{\rm cav} \;-\; \frac{(\Omega^i_{L,y})^2}{\Delta\omega^i_\downarrow}\sigma^i_{\uparrow\uparrow} \;+\; i g^i_{\rm eff}\left[a^\dagger_{\rm cav}\sigma^i_{\downarrow\uparrow} e^{-i\omega^i_{L,y}t} - h.c.\right]\right], \tag{73}$$

$$g^i_{\rm eff}(t) \;=\; \frac{g_{\rm cav}\Omega^i_{L,y}(t)}{2}\left(\frac{1}{\Delta\omega^i_\uparrow} + \frac{1}{\Delta\omega^i_\downarrow}\right), \tag{74}$$

where the sum runs over all QDs of the system, $g^i_{\rm eff}$ is the effective 2-photon coupling coefficient, $\sigma^i_{\uparrow\downarrow} = |\uparrow\rangle\langle\downarrow|$ the spin projection operator for the i-th QD, and $\omega^i_{\uparrow\downarrow} = \omega^i_\uparrow - \omega^i_\downarrow$. The exact two-photon-resonance condition would be $\Delta\omega^i_\uparrow = \omega^i_\uparrow - \omega^i_v - \omega_{\rm cav} = \Delta\omega^i_\downarrow = \omega^i_\downarrow - \omega^i_v - \omega^i_L$. The derivation of $H_{\rm eff}$ assumes $\Delta\omega^i_{\uparrow,\downarrow} \gg g_{\rm cav}$, $\omega^i_{\uparrow\downarrow} \gg k_B T$, and $\omega^{i,j}_{\uparrow\downarrow} \gg g^i_{\rm eff} > \Gamma_{\rm cav}$, where $\Gamma_{\rm cav}$ denotes the cavity decay rate (not included in Eq. (73)). The third and fourth terms of Eq. (73) describe the ac-Stark-effect caused by the cavity and laser fields, respectively.

In order to implement a CNOT quantum gate, one would turn on laser fields ω^i_L and ω^j_L to establish near two-photon resonance condition for both the control (i) and the target (j) qubits,

$$\Delta_i \;=\; \omega^i_{\uparrow\downarrow} - \omega_{cav} + \omega^i_L \;=\; \Delta_j \ll \omega^{i,j}_{\uparrow\downarrow} \quad . \tag{75}$$

If the two-photon detunings Δ_i are chosen large compared to the cavity linewidth and $g^i_{\rm eff}(t)$, the cavity modes can be eliminated with a second Schrieffer-Wolff transformation to obtain an effective two-qubit interaction Hamiltonian in the rotating frame (interaction picture with $H_0 = \sum_i \omega^i_{\uparrow\downarrow}\sigma^i_{\uparrow\uparrow}$),

$$H^{(2)}_{\rm int} \;=\; \sum_{i\neq j} \tilde{g}_{ij}(t)\left[\sigma^i_{\uparrow\downarrow}\sigma^j_{\downarrow\uparrow} e^{i\Delta_{ij}t} \;+\; \sigma^j_{\uparrow\downarrow}\sigma^i_{\downarrow\uparrow} e^{-i\Delta_{ij}t}\right] \quad , \tag{76}$$

where $\tilde{g}_{ij}(t) = g^i_{\rm eff}(t) g^j_{\rm eff}(t)/\Delta_i$ and $\Delta_{ij} = \Delta_i - \Delta_j$. The implementation of the conditional phase-flip (CPF) and the CNOT or quantum XOR gates between two spins i and j from a transversal (XY) spin coupling of the form Eq. (76) has been discussed in Sec. II.B.

The interaction Hamiltonian $H^{(2)}_{\rm int}$ describes the coupling of the QD spins via the following virtual process. One of the QDs emits a virtual photon into the cavity while absorbing a laser photon. The cavity photon is then reabsorbed by the other QD while a laser photon is emitted. Due to the spin splitting in the QD spectrum, Fig. 15 (right), this process is spin sensitive and leads to the spin-spin coupling $H^{(2)}_{\rm int}$ between the QDs.

3. Measurement

In the cavity QED scheme, measurement of a single QD spin can be achieved by applying a laser field $E_{L,y}$ to the QD to be measured, in order to realize exact two-photon resonance with the cavity mode. If the QD spin is in state $|\downarrow\rangle$, there is no Raman coupling and no photons will be detected. If on the other hand, the spin state is $|\uparrow\rangle$, the electron will exchange energy with the cavity mode and eventually a single photon will be emitted from the cavity. A single photon detection capability is thus sufficient for detecting a single spin.

4. Related proposals

A related proposal is to use optically controlled virtual excitations of delocalized excitons as mediators of RKKY type spin interaction between electrons localized in neighboring QDs (Piermarocchi *et al.*, 2002). The spin interaction in this case is isotropic, $H = J\mathbf{S}_i \cdot \mathbf{S}_j$.

F. Decoherence

The spin coherence time in semiconductors—the time over which the phase of a superposition of spin-up and spin-down states, Eq. (1), is well-defined—can be much longer than the charge coherence time (a few nanoseconds). In fact it is known from experiment that they can be orders of magnitude longer. This is of course one of the reasons for using spin as a qubit (Loss and DiVincenzo, 1998) rather than charge. In bulk GaAs and in CdSe quantum dots, the ensemble spin coherence time $T_2^\star$, being a lower bound on the single-spin decoherence time T_2, was measured using a technique called time-resolved Faraday rotation (Gupta *et al.*, 1999; Kikkawa *et al.*, 1997). For a detailed account of these experiments, we refer the reader to Chaps. 4 and 5 of (Awschalom *et al.*, 2002). The spin relaxation time T_1 in a single-electron QD in a GaAs heterostructure was probed via transport measurements and found to approach one microsecond (Hanson *et al.*, 2004, 2003). It has been proposed to also measure the single-spin T_2 in such a structure in a transport experiment by applying electron spin resonance (ESR) techniques (Engel and Loss, 2001). In this scheme, the stationary current exhibits a resonance whose line width is determined by the single-spin decoherence time T_2.

Below, a number of decoherence mechanisms for spin in semiconductor nanostructures will be listed. It Should be emphasized, though, that it is usually hard for *theory* to predict which mechanism is dominant. Nevertheless, the understanding of the underlying mechanisms for a list of possible causes can be a very valuable tool for the purpose of achieving long coherent operation in a future quantum device.

1. Phonons and the spin-orbit coupling

Phonon-assisted transitions between different discrete energy levels (or Zeeman sublevels) in GaAs quantum dots can cause spin flips and therefore spin decoherence (Khaetskii, 2001; Khaetskii and Nazarov, 2000, 2001). There are various mechanisms originating from the spin-orbit coupling which lead to such spin flip processes; the most effective mechanisms in 2D have to do with the broken inversion symmetry, either in the elementary crystal cell or at the heterointerface. The spin-orbit Hamiltonian for the electron in such a structure is given by Eq. (22). The relaxation rates $\Gamma = T_1^{-1}$ are evaluated in leading perturbation order in this coupling, with and without a magnetic field. The spin-orbit coupling $H_{\rm so}$ mixes the spin-up and spin-down states of the electron and leads to a non-vanishing matrix element of the phonon-assisted transition between two states with opposite spins. However, one of the main findings of (Khaetskii, 2001; Khaetskii and Nazarov, 2000, 2001) is that the spin relaxation of the electrons localized in the dots differs strongly from that of delocalized electrons. It turns out that in quantum dots (in contrast to extended 2D states), the contributions to the spin-flip rate proportional to β^2 are absent in general. This greatly reduces the spin-flip rates of electrons confined to dots. The finite Zeeman splitting in the energy spectrum also leads to contributions $\propto \beta^2$,

$$\Gamma \simeq \Gamma_0(B) \left(\frac{m\beta^2}{\hbar\omega_0}\right) \left(\frac{g\mu_B B}{\hbar\omega_0}\right)^2, \tag{77}$$

where $\hbar\omega_0$ is the orbital energy level splitting in the QD and $\Gamma_0(B)$ is the inelastic rate without spin flip for the transition between neighboring orbital levels.

Spin-flip transitions between Zeeman sublevels occur with a rate that is proportional to the fifth power of the Zeeman splitting,

$$\Gamma_z \simeq \frac{(g\mu_B B)^5}{\hbar(\hbar\omega_0)^4}\Lambda_p. \tag{78}$$

The dimensionless constant $\Lambda_p \propto \beta^2$ characterizes the strength of the effective spin–piezo-phonon coupling in the heterostructure and ranges from $\approx 7\cdot 10^{-3}$ to $\approx 6\cdot 10^{-2}$ depending on β. To give a number, $\Gamma_z \approx 1.5\cdot 10^3\,\mathrm{s}^{-1}$ for $\hbar\omega_0 = 10\,\mathrm{K}$ and at a magnetic field $B = 1\,\mathrm{T}$.

It can be shown that under realistic conditions, a general symmetry argument leads to the conclusion that the spin decoherence time T_2 does not have a transverse contribution (in leading order), in other words, $T_2 = 2T_1$ for spin-orbit (phonon) related processes (Golovach *et al.*, 2004).

2. Nuclear spins

The nuclear spins of the host material can cause decoherence via spin flips that are caused by the hyperfine interaction. A rough perturbative estimate of this effect (Burkard *et al.*, 1999a) suggests that the rate of such processes can be suppressed by either polarizing the nuclear spins or by applying an external magnetic field. The suppression factor is $(B_\mathrm{n}^*/B)^2/N$, where $B_\mathrm{n}^* = AI/g\mu_\mathrm{B}$ is the maximal magnitude of the effective nuclear field (Overhauser field), N the number of nuclear spins in the vicinity of the electron, and A the hyperfine coupling constant. In GaAs, the nuclear spin of both Ga and As is $I = 3/2$. The field B denotes either the external field, or, in the absence of an external field, the Overhauser field $B = pB_\mathrm{n}^*$ due to the nuclear spin polarization p, which can be obtained e.g. by optical pumping (Dobers *et al.*, 1988) or by spin-polarized currents at the edge of a 2DEG (Dixon *et al.*, 1997). In the latter case, the suppression of the spin flip rate becomes $1/p^2N$.

A more detailed analysis treats a single electron confined to an isolated QD under the influence of the hyperfine interaction with the surrounding nuclei (Khaetskii *et al.*, 2002). It turns out that the electron spin decoherence time T_2 is shorter than the nuclear spin relaxation time T_{n2} determined by the dipole-dipole interaction between nuclei, and therefore the problem can be considered in the absence of the nuclear dipole-dipole interaction. Since the hyperfine interaction depends on the position via a factor $|\psi(\mathbf{r})|^2$ where $\psi(\mathbf{r})$ is the electron wavefunction, the value of the hyperfine interaction varies spatially. It turns out that this is the relevant cause of decoherence. The analysis is complicated by the fact that in a weak external Zeeman field (smaller than a typical fluctuating Overhauser field seen by the electron, ~ 100 Gauss in a GaAs QD), the perturbative treatment of the electron spin decoherence breaks down and the decay of the spin precession amplitude is not exponential in time, but either described by a power law, $1/t^{d/2}$ (for finite Zeeman fields) or an inverse logarithm, $1/(\ln t)^{d/2}$ (for vanishing fields).

The decay rate $1/T_2$ is thus roughly given by $A/\hbar N$, where A is the hyperfine interaction constant, and N is the number of nuclei within the dot, with N typically 10^5. This time is of the order of several μs. However, it needs to be stressed that there is no simple exponential decay which, strictly speaking, means that decoherence cannot simply be characterized by the decay times T_1 and T_2 in this case. The case of a fully polarized nuclear spin state was solved exactly in (Khaetskii *et al.*, 2002). The amplitude of the precession which is approached after the decay, is of order one, while the decaying part is $1/N$, in agreement with earlier results (Burkard *et al.*, 1999a), see above. A large difference between the values of T_2 (decoherence time for a single dot) and $T_2^\star$ (dephasing time for an ensemble of dots), i.e. $T_2^\star \ll T_2$ is found and indicates that it is desirable to have direct experimental access to single spin decoherence times.

The non-Markovian dynamics of a localized electron spin interacting with an environment of nuclear spins with arbitrary polarization p was calculated in (Coish and Loss, 2004) from a perturbative analysis of the generalized master equation for the longitudinal and transverse components of the electron spin.

IV. SUPERCONDUCTING MICRO-CIRCUITS

A. Overview

Roughly speaking, three prototypes of superconducting (SC) qubits are studied experimentally. We only briefly review them here, and refer the reader to (Makhlin *et al.*, 2001) for a comprehensive review. The charge qubit (Averin, 1998; Makhlin *et al.*, 1999; Nakamura *et al.*, 1999; Pashkin *et al.*, 2003; Shnirman *et al.*, 1997; Vion *et al.*, 2002), operating in the regime $E_C \gg E_J$, and the flux qubit (Chiorescu *et al.*, 2003; Mooij *et al.*, 1999; Orlando *et al.*, 1999; van der Wal *et al.*, 2000), operating in the regime $E_J \gg E_C$, are distinguished by their Josephson junctions' relative magnitude of charging energy E_C and Josephson energy E_J. A third type, the phase qubit (Ioffe *et al.*, 1999; Martinis

et al., 2002), operates in the same regime as the flux qubit, but is represented purely in the SC phase and is not associated with any magnetic flux or circulating current. The Josephson phase qubit consists of a single Josephson junction (Martinis *et al.*, 2002). In flux qubits, the quantum state of the SC phase differences across the Josephson junctions in the circuit contain the quantum information, i.e., the state of the qubit. A micrograph of the circuit for a SC flux qubit studied in (Chiorescu *et al.*, 2003) is shown in Fig. 16. In charge qubits, the quantum state of the charge on SC islands contains the quantum information.

Both charge and flux qubits have been described by an approximate pseudo-spin Hamiltonian of the type (Makhlin *et al.*, 2001),

$$H = \frac{\Delta}{2}\sigma_x + \frac{\epsilon}{2}\sigma_z, \tag{79}$$

where Δ denotes the tunnel coupling between the two qubit states $|0\rangle$ and $|1\rangle$ (eigenstates of σ_z) and ϵ the bias (asymmetry). In Sec. IV.C, a more general model, including the full Hilbert space of a SC circuit, will be discussed.

B. Decoherence, visibility, and leakage

1. Decoherence

Decoherence within the model Eq. (79) can be understood phenomenologically as follows. If the qubit is initially prepared in state $|1\rangle$, then it will undergo free Larmor oscillations with frequency $\nu = h^{-1}\sqrt{\Delta^2 + \epsilon^2}$. Ideally, the probability for finding the qubit in state $|1\rangle$ after time t would be a perfect cosine function of t. This ideal Larmor precession is shown as a thin dotted line in Fig. 17. Such a Larmor precession experiment (also known as Ramsey fringe experiment) determines how well the qubit satisfies item I.A.3 of DiVincenzo's five criteria. Decoherence is a process in which the amplitude of the oscillations decays over time, as shown by the thick solid line in Fig. 17. This decay is often (but not always) exponential with a characteristic decoherence time T_2.

All types of SC qubits suffer from decoherence that is caused by a several sources. Decoherence in charge qubits has been investigated using the spin-boson model in (Makhlin *et al.*, 2001; Makhlin and Shnirman, 2004). In flux qubits, the Johnson-Nyquist noise from lossy circuit elements (e.g., current sources) has been identified as one important cause of decoherence (Tian *et al.*, 2000, 2002; van der Wal *et al.*, 2003; Wilhelm *et al.*, 2003). A systematic theory of decoherence of a qubit from such dissipative elements, based on the network graph analysis (Devoret, 1997) of the underlying SC circuit, was developed for SC flux qubits (Burkard *et al.*, 2004b), and applied to study the effect of asymmetries in a persistent-current qubit (Burkard *et al.*, 2004a). The circuit theory for SC qubits will be discussed further below in Sec. IV.C. For the Josephson phase qubit (Martinis *et al.*, 2002), decoherence due to bias noise and junction resonators was studied in (Martinis *et al.*, 2003; Simmonds *et al.*, 2004).

2. Visibility

A different type of imperfection that typically affects SC qubits is a limited visibility v. This effect means that the maximum range v of the read-out probability of the qubit being in state $|1\rangle$ is smaller than one. This means, e.g., that the probability $p(0)$ of measuring the qubit in state $|1\rangle$ right after preparation in this state is less than one. In the case of a symmetric reduction of the visibility, the relation is $p(0) = (1 + v)/2$. This effect is schematically shown in Fig. 17.

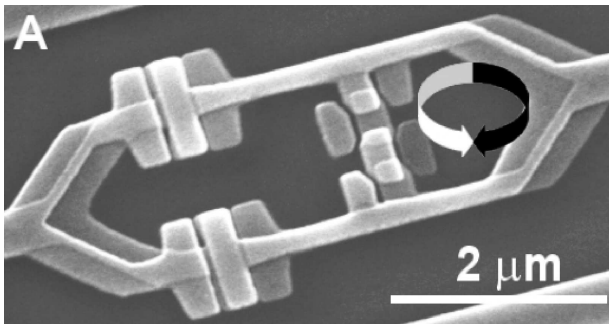


FIG. 16 Electron micrograph of the SC flux qubit circuit studied in (Chiorescu *et al.*, 2003). The logical qubit basis states correspond to circulating SC currents in the smaller loop as indicated. The bright areas are the Al wires; the double-layer structure from the shadow evaporation deposition is clearly visible. (Figure courtesy of I. Chiorescu and J. E. Mooij, TU Delft).

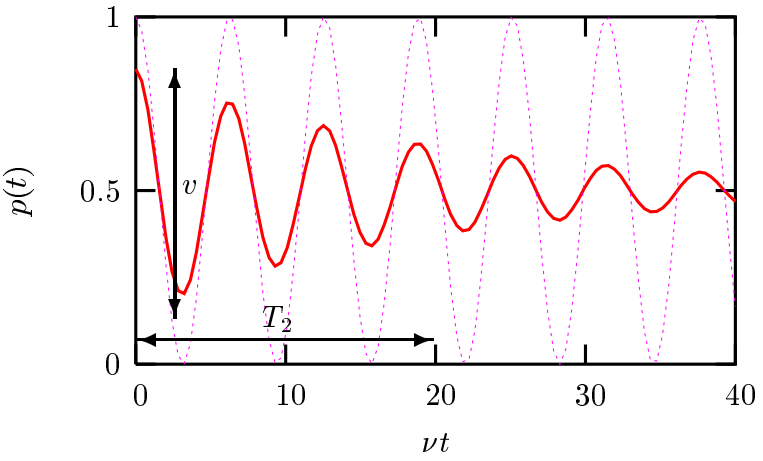


FIG. 17 Theoretical Larmor precession (Ramsey fringe) curve with decoherence time $T_2 < \infty$ and limited visibility $v < 1$ (solid thick line), compared to the ideal curve (dotted thin line). The probability $p(t)$ to find the qubit in state $|1\rangle$ is plotted as a function of the free evolution time t. The Larmor frequency of the coherent oscillations is denoted with ν. The *visibility* v is the maximum range of $p(0)$ whereas the *decoherence time* T_2 is the time over which the oscillations are damped out (in the case of an exponential decay). For this plot, we have chosen $T_2 = 20/\nu$ and $v = 70\,\%$.

3. Leakage

Limitations of the visibility are often attributed to a mechanism called leakage. Since the SC phase is a continuous variable as, e.g., the position of a particle, superconducting qubits (two-level systems) have to be obtained by truncation of an infinite-dimensional Hilbert space. This truncation is only approximate for various reasons; (i) because it may not be possible to prepare the initial state with perfect fidelity in the lowest two states, (ii) because of erroneous transitions to higher levels (leakage effects) due to imperfect gate operations on the system, and (iii) because of erroneous transitions to higher levels due to the unavoidable interaction of the system with the environment. Apparent leakage effects may occur if the read-out process is not 100% accurate. Leakage effects due to the non-adiabaticity of externally applied fields were studied in (Fazio *et al.*, 1999). Recent work (Meier and Loss, 2004) shows that leakage in microwave-driven Josephson phase qubits leading to a reduced visibility can occur, even if the microwave source is pulsed slowly.

C. Circuit theory

A recently developed method for deriving the Hamiltonian of SC circuits from their classical dynamics, combined with the theory of dissipative quantum systems, can be utilized to describe decoherence in arbitrary SC circuits (Burkard *et al.*, 2004b).

There exists a variety of theoretical models for dissipative environments in general, and dissipative electrical circuit elements (impedances) in particular. A dissipative (resistive) element can be modeled as a transmission line (Werner and Drummond, 1991; Yurke, 1987; Yurke and Denker, 1994), i.e. an infinite set of dissipation-free elements (capacitors and inductors), or, alternatively, within the widely known Caldeira-Leggett model (Caldeira and Leggett, 1983; Leggett *et al.*, 1987; Weiss, 1999) as a continuum of harmonic oscillators that is coupled to the degrees of freedom of the system (in this case, the SC circuit). In the following, the Caldeira-Legget approach will be used.

The systematic derivation of the dynamical equations for a general (classical) electric circuit is a well-known problem in electric engineering that has been tackled using the elegant and convenient network graph analysis methods (Peikari, 1974). It has been suggested early on that these methods may also be used for a description of the dissipative quantum dynamics of superconducting circuits (Devoret, 1997). We shall now explain the circuit graph analysis applied to SC qubits, both of the flux (Sec.IV.D) and charge (Sec.IV.E) type.

D. Flux qubits

In this Section, the results of the circuit theory for flux qubits are presented; for a derivation, see (Burkard *et al.*, 2004b). The IBM qubit (Koch *et al.*, 2003) will be used as a first example, and then followed by other examples. The IBM qubit is described by the electrical circuit drawn in Fig. 18.

1. The network graph

As a first step in the circuit analysis of a SC flux qubit, the *network graph* of the SC circuit is drawn and labeled. In the graph, each two-terminal element (Josephson junction, capacitor, inductor, external impedance, current source) is represented as a branch connecting two nodes. In Fig. 18 (left panel), the IBM qubit is represented as a network graph, where thick lines are used as a shorthand for resistively shunted Josephson junctions, or RSJ (see Fig. 18, right panel). A convention for the direction of all branches has to be chosen–in Fig. 18, the direction of branches is represented by an arrow.

2. The tree of the network graph

As a second step, a *tree* of the network graph needs to be specified. A tree of a graph is a set of branches connecting all nodes without containing any loops. Here, the tree is chosen such that it contains all capacitors, as few inductors as possible, and neither resistors (external impedances) nor current sources. The conditions under which such a choice can be made are discussed in (Burkard *et al.*, 2004b). The tree of Fig. 18(right) that will be used here is shown in Fig. 18(center). The branches in the tree are called *tree branches*; all other branches are called *chords*. Each chord is associated with exactly one so-called fundamental loop that is obtained when adding the chord to the tree.

3. The loop matrices

In a next step, the loop sub-matrices $\mathbf{F}_{CL}$, $\mathbf{F}_{CZ}$, $\mathbf{F}_{CB}$, $\mathbf{F}_{KL}$, $\mathbf{F}_{KZ}$, and $\mathbf{F}_{KB}$ need to be found. The loop sub-matrices $\mathbf{F}_{XY}$ have entries $+1$, -1, or 0, and hold the information about which tree branches of type X belong to which fundamental loop associated with the chords of type Y. E.g., for our example,

$$\mathbf{F}_{CL} = \begin{pmatrix} 1 & 0 \\ -1 & 1 \\ 0 & -1 \end{pmatrix}, \tag{80}$$

where the first column determines that the capacitor C_1 (part of J_1) belongs to the large loop (associated with L_1), capacitor C_2 (part of J_2) belongs to the large loop (with different orientation), while capacitor C_3 (part of J_3) does not belong to the large loop at all. Similarly, the second column of $\mathbf{F}_{CL}$ says which of the capacitors are contained in the small loop (associated with L_3).

The loop matrices have the purpose of systematically incorporating Kirchhoff's laws of current and energy conservation in the circuit,

$$\mathbf{F}^{(C)}\mathbf{I} = (\mathbb{1} \,|\, \mathbf{F})\,\mathbf{I} = 0, \tag{81}$$

$$\mathbf{F}^{(L)}\mathbf{V} = \left(-\mathbf{F}^T \,|\, \mathbb{1}\right)\mathbf{V} = \dot{\mathbf{\Phi}}, \tag{82}$$

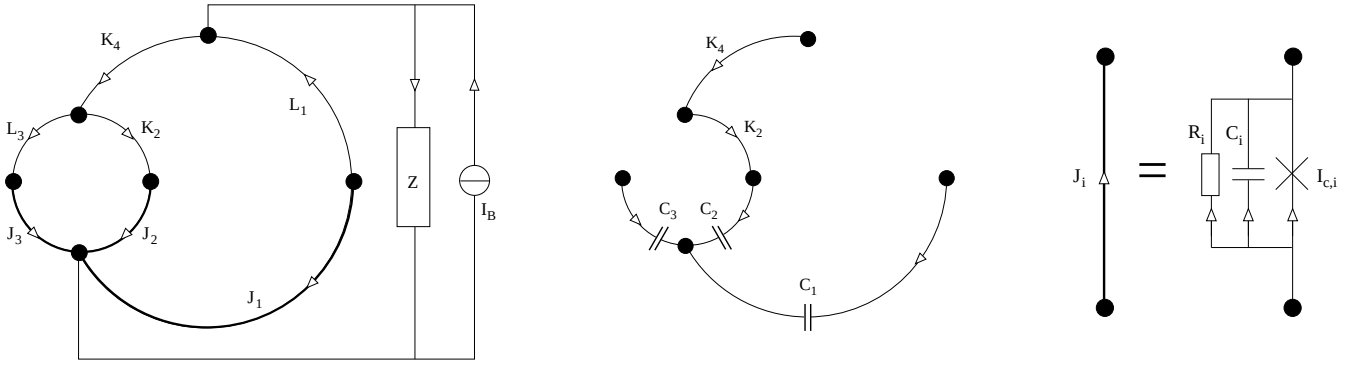


FIG. 18 Left: The IBM qubit is an example of a network graph. Each thick line represents a Josephson element, i.e. three branches in parallel, see right panel. Thin lines represent simple two-terminal elements, such as linear inductors (L, K), external impedances (Z), and current sources (I_B). Center: A Josephson subgraph (thick line) consists of three branches; a Josephson junction (cross), a shunt capacitor (C), a shunt resistor (R), and no extra nodes. Right: A tree for the circuit shown on the right. A tree is a subgraph containing all nodes and no loop. Here, a tree was chosen that contains all capacitors (C), some inductors (K), but no current sources (I_B) or external impedances (Z).

where the external magnetic fluxes are denoted with $\mathbf{\Phi}$, and where the loop sub-submatrices

$$\mathbf{F} = \begin{pmatrix} \mathbf{F}_{CJ} & \mathbf{F}_{CL} & \mathbf{F}_{CR} & \mathbf{F}_{CZ} & \mathbf{F}_{CB} \\ \mathbf{F}_{KJ} & \mathbf{F}_{KL} & \mathbf{F}_{KR} & \mathbf{F}_{KZ} & \mathbf{F}_{KB} \end{pmatrix} \tag{83}$$

are related to the full fundamental loop and cutset matrices $\mathbf{F}^{(L)}$ and $\mathbf{F}^{(C)}$ via the grouping of the branch currents and voltages into a tree and a chord part, $\mathbf{I} = (\mathbf{I}_{\rm tr}, \mathbf{I}_{\rm ch})$ and $\mathbf{V} = (\mathbf{V}_{\rm tr}, \mathbf{V}_{\rm ch})$.

4. Current-voltage relations (CVRs)

In order to derive the equations of motion and eventually, the Hamiltonian of the SC circuit, Kirchhoff's laws, Eqs. (81) and (82) need to be combined with the CVRs of the various branch elements. For this purpose, the tree and chord currents and voltages are divided up further, according to the various branch types, $\mathbf{I}_{\rm tr} = (\mathbf{I}_C, \mathbf{I}_K)$, and $\mathbf{I}_{\rm ch} = (\mathbf{I}_J, \mathbf{I}_L, \mathbf{I}_R, \mathbf{I}_Z, \mathbf{I}_B)$, and similarly for the voltages. The tree current and voltage vectors contain a capacitor (C) and tree inductor (K) part, whereas the chord current and voltage vectors consist of parts for chord inductors, both non-linear (J) and linear (L), shunt resistors (R) and other external impedances (Z), and bias current sources (B). The branch charges and fluxes ($X = C, K, J, L, R, Z, B$) are formally defined as

$$\mathbf{I}_X(t) = \dot{\mathbf{Q}}_X(t), \tag{84}$$

$$\mathbf{V}_X(t) = \dot{\mathbf{\Phi}}_X(t). \tag{85}$$

Using the second Josephson relation and Eq. (85), we identify the formal fluxes associated with the Josephson junctions as the superconducting phase differences $\boldsymbol{\varphi}$ across the junctions,

$$\frac{\mathbf{\Phi}_J}{\Phi_0} = \frac{\boldsymbol{\varphi}}{2\pi}, \tag{86}$$

where $\Phi_0 = h/2e$ is the superconducting flux quantum. Each branch type has its own current-voltage relation (CVR); e.g., the Josephson junction branches follow the first Josephson relation,

$$\mathbf{I}_J = \mathbf{I}_{\rm c}\, \mathbf{sin}\boldsymbol{\varphi}, \tag{87}$$

with the critical current matrix $\mathbf{I}_{\rm c}$, while the external impedances are described by the integral relation,

$$\mathbf{V}_Z(t) = \int_{-\infty}^{t} \mathbf{Z}(t-\tau)\mathbf{I}_Z(\tau)d\tau \equiv (\mathbf{Z} * \mathbf{I}_Z)(t). \tag{88}$$

The total inductance matrix

$$\mathbf{L}_{\rm t} = \begin{pmatrix} \mathbf{L} & \mathbf{L}_{LK} \\ \mathbf{L}_{LK}^T & \mathbf{L}_K \end{pmatrix}, \tag{89}$$

is used for the CVR of the chord (L) and tree (K) inductances,

$$\begin{pmatrix} \mathbf{\Phi}_L \\ \mathbf{\Phi}_K \end{pmatrix} = \mathbf{L}_{\rm t} \begin{pmatrix} \mathbf{I}_L \\ \mathbf{I}_K \end{pmatrix}, \tag{90}$$

where $\mathbf{L}$ and $\mathbf{L}_K$ are the self inductances of the chord and tree branch inductors, resp., off-diagonal elements describing the mutual inductances among chord inductors and tree inductors separately, and $\mathbf{L}_{LK}$ is the mutual inductance matrix between tree and chord inductors.

5. The Hamiltonian

The elements described above are sufficient to determine the Hamiltonian of the dissipation-free system,

$$\mathcal{H}_S = \frac{1}{2}\mathbf{Q}_C^T\mathbf{C}^{-1}\mathbf{Q}_C + \left(\frac{\Phi_0}{2\pi}\right)^2 U(\boldsymbol{\varphi}), \tag{91}$$

$$U(\boldsymbol{\varphi}) = -\sum_i \frac{2\pi I_{c;i}}{\Phi_0}\cos\varphi_i + \frac{1}{2}\boldsymbol{\varphi}^T\mathbf{M}_0\boldsymbol{\varphi} + \frac{2\pi}{\Phi_0}\boldsymbol{\varphi}^T\left(\mathbf{N}\mathbf{\Phi}_x + \mathbf{S}\mathbf{I}_B\right), \tag{92}$$

where $\mathbf{Q}_C$ are the charges conjugate to the fluxes $\mathbf{\Phi}_J = (\Phi_0/2\pi)\boldsymbol{\varphi}$ and $\mathbf{C}$ is the capacitance matrix of the circuit. The matrices $\mathbf{M}_0$, $\mathbf{N}$, and $\mathbf{S}$ are obtained from the inductance and loop matrices $\mathbf{L}_t$ and $\mathbf{F}$ (Burkard *et al.*, 2004b). The Hamiltonian Eq. (91) is quantized using the commutator relation

$$\left[\frac{\Phi_0}{2\pi}\varphi_i, Q_{C;j}\right] = i\hbar\delta_{ij}. \tag{93}$$

The system including dissipation can be described using the Caldeita-Legget model,

$$\mathcal{H} = \mathcal{H}_S + \mathcal{H}_B + \mathcal{H}_{SB}, \tag{94}$$

$$\mathcal{H}_B = \frac{1}{2}\sum_\alpha \left(\frac{p_\alpha^2}{m_\alpha} + m_\alpha\omega_\alpha^2 x_\alpha^2\right), \tag{95}$$

$$\mathcal{H}_{SB} = \mathbf{m}\cdot\boldsymbol{\varphi}\sum_\alpha c_\alpha x_\alpha + \Delta U(\boldsymbol{\varphi}), \tag{96}$$

where $\mathcal{H}_S$ is the quantized Hamiltonian Eq. (91), $\mathcal{H}_B$ is the Hamiltonian describing a bath of harmonic oscillators with (fictitious) position and momentum operators x_α and p_α with $[x_\alpha, p_\beta] = i\hbar\delta_{\alpha\beta}$, masses m_α, and oscillator frequencies ω_α. Finally, $\mathcal{H}_{SB}$ describes the coupling between the system and bath degrees of freedom, $\boldsymbol{\varphi}$ and x_α, where c_α is a coupling parameter and $\mathbf{m}$ are obtained from the inductance and loop matrices $\mathbf{L}_t$ and $\mathbf{F}$ (Burkard *et al.*, 2004b).

The quantum dynamics of the entire system (qubit plus bath of oscillators) is described by the Liouville equation $\dot\rho(t) = -i[\mathcal{H}, \rho(t)] \equiv -i\mathcal{L}\rho(t)$ for the density matrix ρ. The state of the system alone is described by the reduced density matrix $\rho_S(t) = \mathrm{Tr}_B\,\rho(t)$. In the Born-Markov approximation, the master equation for $\rho_S(t)$ can be written in the form of the Redfield equations (Redfield, 1957),

$$\dot\rho_{nm}(t) = -i\omega_{nm}\rho_{nm}(t) - \sum_{kl} R_{nmkl}\rho_{kl}(t), \tag{97}$$

where $\rho_{nm} = \langle n|\rho_S|m\rangle$ are the matrix elements of ρ in the eigenbasis $|n\rangle$ of $\mathcal{H}_S$ (eigenenergies ω_n), and $\omega_{nm} = \omega_n - \omega_m$, and with the Redfield tensor,

$$R_{nmkl} = \delta_{lm}\sum_r \Gamma^{(+)}_{nrrk} + \delta_{nk}\sum_r \Gamma^{(-)}_{lrrm} - \Gamma^{(+)}_{lmnk} - \Gamma^{(-)}_{lmnk}, \tag{98}$$

$$\mathrm{Re}\Gamma^{(+)}_{lmnk} = (\mathbf{m}\cdot\boldsymbol{\varphi})_{lm}(\mathbf{m}\cdot\boldsymbol{\varphi})_{nk} J(|\omega_{nk}|)\frac{e^{-\beta\omega_{nk}/2}}{\sinh\beta|\omega_{nk}|/2},$$

$$\mathrm{Im}\Gamma^{(+)}_{lmnk} = -(\mathbf{m}\cdot\boldsymbol{\varphi})_{lm}(\mathbf{m}\cdot\boldsymbol{\varphi})_{nk}\frac{2}{\pi}P\int_0^\infty d\omega \frac{J(\omega)}{\omega^2-\omega_{nk}^2}\left(\omega - \omega_{nk}\coth\frac{\beta\omega}{2}\right). \tag{99}$$

In the two-dimensional qubit subspace, the Bloch vector $\mathbf{p} = \mathrm{Tr}(\boldsymbol{\sigma}\rho)$ can be introduced where $\boldsymbol{\sigma} = (\sigma_x, \sigma_y, \sigma_z)$ are the Pauli matrices, and the Redfield equation (97) takes the form of the Bloch equation $\dot{\mathbf{p}} = \boldsymbol{\omega}\times\mathbf{p} - R\mathbf{p} + \mathbf{p}_0$, with $\boldsymbol{\omega} = (0, 0, \omega_{01})^T$, where in the secular approximation, the relaxation matrix R is diagonal, $R = \mathrm{diag}(T_2^{-1}, T_2^{-1}, T_1^{-1})$. The relaxation and decoherence times T_1 and T_2 are then given by

$$\frac{1}{T_1} = 4|\langle 0|\mathbf{m}\cdot\boldsymbol{\varphi}|1\rangle|^2 J(\omega_{01})\coth\frac{\omega_{01}}{2k_BT}, \tag{100}$$

$$\frac{1}{T_2} = \frac{1}{2T_1} + \frac{1}{T_\phi}, \tag{101}$$

$$\frac{1}{T_\phi} = |\langle 0|\mathbf{m}\cdot\boldsymbol{\varphi}|0\rangle - \langle 1|\mathbf{m}\cdot\boldsymbol{\varphi}|1\rangle|^2\,\frac{J(\omega)}{\omega}\bigg|_{\omega\to 0} 2k_BT. \tag{102}$$

In the semiclassical approximotion, T_1 and T_ϕ can be related to the parameters Δ and ϵ in the Hamiltonian Eq. (79),

$$\frac{1}{T_1} = \left(\frac{\Delta}{\omega_{01}}\right)^2 |\Delta\boldsymbol{\varphi}\cdot\mathbf{m}|^2\, J(\omega_{01})\coth\frac{\omega_{01}}{2k_BT}, \tag{103}$$

$$\frac{1}{T_\phi} = \left(\frac{\epsilon}{\omega_{01}}\right)^2 |\Delta\boldsymbol{\varphi}\cdot\mathbf{m}|^2\,\frac{J(\omega)}{\omega}\bigg|_{\omega\to 0} 2k_BT. \tag{104}$$

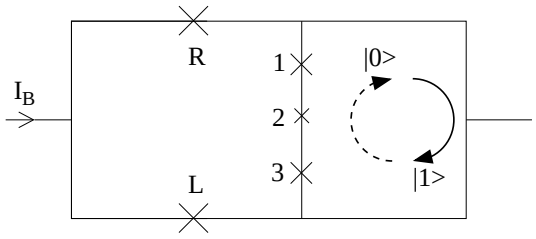


FIG. 19 Schematic of the Delft circuit, Fig. 16, where the crosses denote Josephson junctions. The outer loop with two junctions L and R forms a dc SQUID that is used to read out the qubit. The state of the qubit is determined by the orientation of the circulating current in the small loop, comprising the junctions 1, 2, and 3, one of which has a slightly smaller critical current than the others. A bias current I_B can be applied as indicated for read-out.

6. Leakage

The leakage rate from a qubit state $k = 0, 1$ into higher levels $n = 2, 3, \ldots$ outside the qubit space can be quantified from the Redfield equation Eq. (97) by the sum

$$\frac{1}{T_{L,k}} = 4 \sum_n |\langle n|\mathbf{m} \cdot \boldsymbol{\varphi}|k\rangle|^2 J(\omega_{kn}) \coth \frac{\omega_{kn}}{2k_B T}. \tag{105}$$

7. The Delft qubit

A very successful qubit design is the Delft qubit (Chiorescu *et al.*, 2003) which is depicted in Fig. 16, and which will be discussed in this Section. A schematical drawing of the SC circuit for the Delft qubit is shown in Fig. 19. This design is intended to be immune to current fluctuations in the current bias I_B due to its symmetry properties; at zero dc bias, $I_B = 0$, and independent of the applied magnetic field, a small fluctuating current $\delta I_B(t)$ caused by the finite impedance of the external control circuit (the current source) is divided equally into the two arms of the SQUID loop and no net current flows through the three-junction qubit line. Hence, in the ideal circuit (Fig. 19) the qubit is protected from decoherence due to current fluctuations in the bias current line. However, asymmetries in the SQUID loop may spoil the protection of the qubit from decoherence. In the case of an inductively coupled SQUID (Mooij *et al.*, 1999; Orlando *et al.*, 1999; van der Wal *et al.*, 2000) neither a small geometrical asymmetry (imbalance of self- and mutual inductances in the SQUID loop), nor thejunction (critical current) asymmetry of typically a few percent, would suffice to cause a relevant amount of decoherence at zero bias current $I_B = 0$ (Burkard *et al.*, 2004b). What turns out to be important here is that the circuit (Fig. 16) contains another asymmetry, caused by its *double layer structure*, being an artifact of the fabrication method used to produce SC circuits with aluminum/aluminum oxide Josephson junctions, the so-called shadow evaporation technique. Junctions produced with this technique will always connect the top layer with the bottom layer, see Fig. 20.

Thus, while circuits like Fig. 19 can be produced with this technique, strictly speaking, loops will always contain an even number of junctions. In order to analyze the implications of the double layer structure for the circuit in Fig. 19, the circuit is drawn again in Fig. 21(a) with separate upper and lower layers. Note that each piece of the upper layer is connected with the underlying piece of the lower layer via an "unintentional" Josephson junction.

These extra junctions typically have large areas and therefore large critical currents; thus, their Josephson energy can often be neglected. In order to study the lowest-order effect of the double layer structure, one can neglect all unintentional junctions in this sense and arrive at the circuit Fig. 21(b). It should be emphasized that the resulting circuit is distinct from the 'ideal' circuit Fig. 19 which does not reflect the double-layer structure. In the real circuit, Fig. 21(b), the symmetry between the two arms of the dc SQUID is broken, and thus it can be expected that bias current fluctuations cause decoherence of the qubit at zero dc bias current, $I_B = 0$.

Starting from the circuit graph of the Delft qubit, the circuit theory can be used to find the Hamiltonian of the circuit, which can subsequently be analyzed numerically. The double-well minima $\boldsymbol{\varphi}_0$ and $\boldsymbol{\varphi}_1$ was found for a range of bias currents and applied external flux. The states localized at $\boldsymbol{\varphi}_0$ and $\boldsymbol{\varphi}_1$ are encoding the logical $|0\rangle$ and $|1\rangle$ states of the qubit. Two special lines in the plane spanned by the bias currents and applied external flux can now be determined, see Fig. 23. (i) The line $f^*(I_B)$ on which a *symmetric* double well is predicted, $\epsilon \equiv U(\boldsymbol{\varphi}_0) - U(\boldsymbol{\varphi}_1) = 0$. On this line, the dephasing time T_ϕ diverges. (ii) The line on which $\mathbf{m} \cdot \Delta\boldsymbol{\varphi} = 0$, where $\Delta\boldsymbol{\varphi} = \boldsymbol{\varphi}_0\boldsymbol{\varphi}_1$ is the vector joining the two minima of the potential. On this line, the environment is *decoupled* from the system, and both the relaxation and

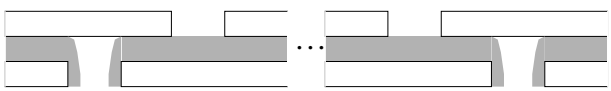


FIG. 20 Schematics of Josephson junctions produced by the shadow evaporation technique, connecting the upper with the lower aluminum layer. Shaded regions represent the aluminum oxide.

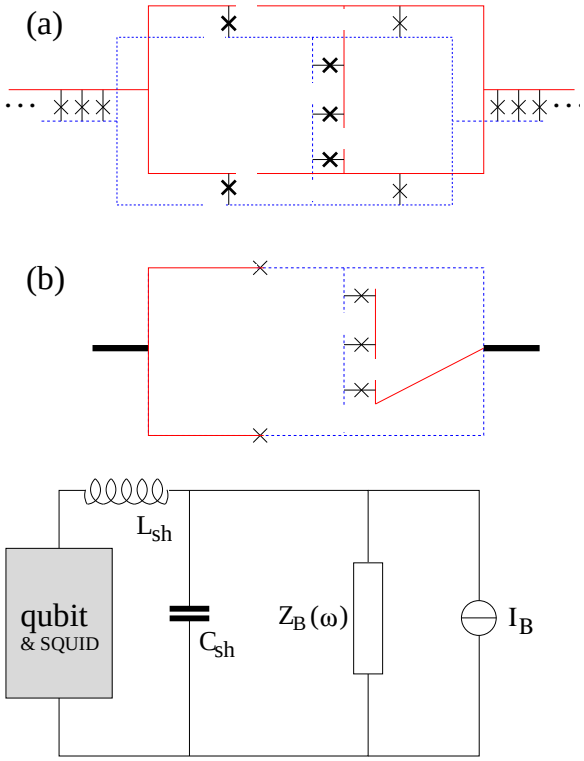


FIG. 21 (a) Double layer structure. Dashed blue lines represent the lower, solid red lines the upper SC layer, and crosses indicate Josephson junctions. The thick crosses are the intended junctions, while the thin crosses are the unintended distributed junctions due to the double-layer structure. (b) Simplest circuit model of the double layer structure. The symmetry between the upper and lower arms of the SQUID has been broken by the qubit line comprising three junctions. Thick black lines denote pieces of the SC in which the upper and lower layer are connected by large area junctions.

FIG. 22 External circuit attached to the qubit (Fig. 19) that allows the application of a bias current I_B for qubit read-out. The inductance $L_{\rm sh}$ and capacitance $C_{\rm sh}$ form the *shell circuit*, and $Z(\omega)$ is the total impedance of the current source (I_B). The case where a voltage source is used to generate a current can be reduced to this using Norton's theorem.

the decoherence times diverge, $T_{1,2,\phi} \to \infty$. The curve $f^*(I_B)$ agrees qualitatively with the experimentally measured symmetry line (Bertet *et al.*, 2004), but it underestimates the magnitude of the variation in flux f' as a function of I_B. The point where the symmetric and the decoupling lines intersect coincides with the maximum of the symmetric line, as can be understood from the following argument. Taking the total derivative with respect to I_B of the relation $\epsilon = U(\boldsymbol{\varphi}_0; f^*(I_B), I_B) - U(\boldsymbol{\varphi}_1; f^*(I_B), I_B) = 0$ on the symmetric line, and using that $\boldsymbol{\varphi}_{0,1}$ are extremal points of U, we obtain $\mathbf{n}\cdot\Delta\boldsymbol{\varphi}\,\partial f^*/\partial I_B + (2\pi/\Phi_0)\mathbf{m}\cdot\Delta\boldsymbol{\varphi} = 0$ for some constant vector $\mathbf{n}$. Therefore, $\mathbf{m}\cdot\Delta\boldsymbol{\varphi} = 0$ (decoupling line) and $\mathbf{n}\cdot\Delta\boldsymbol{\varphi} \neq 0$ implies $\partial f^*/\partial I_B = 0$.

The relaxation and decoherence times T_1 and T_2 on the symmetric line have been evaluated and are plotted (Fig. 23, right) where $\epsilon = 0$, and therefore, $E = \Delta$. The divergence in T_ϕ on the symmetric line is cut off by higher-order effects, whereas the divergence of T_1 on the decoupling line is cut off by residual impedances, e.g., due to the junctions' quasiparticle resistance (Burkard *et al.*, 2004a). A peak in the relaxation and decoherence times where predicted from

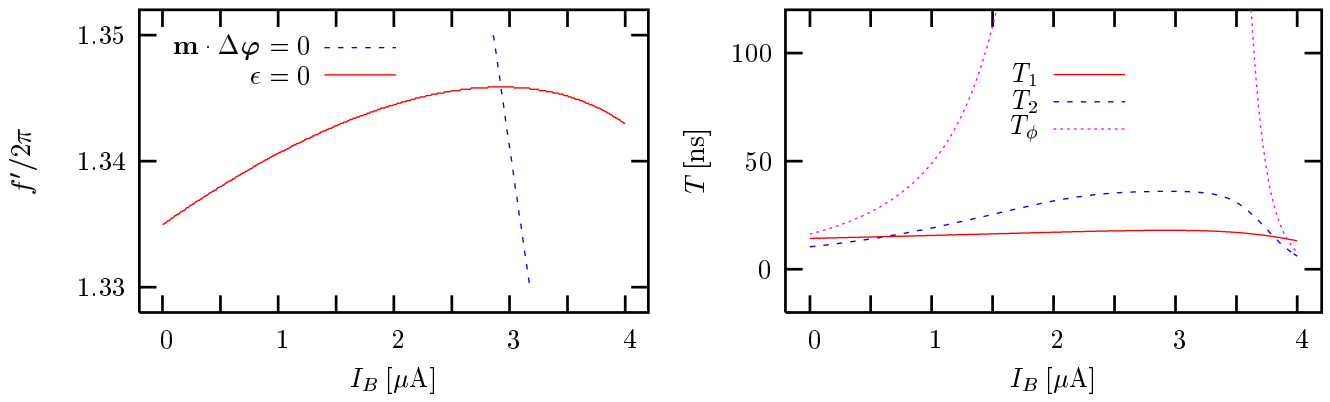


FIG. 23 Left: Decoupling (red solid) and symmetric (blue dashed) curves in the (I_B, f') plane, where I_B is the applied bias current and $f' = 2\pi\Phi'_x/\Phi_0$ is the dimensionless externally applied magnetic flux threading the SQUID loop. Both curves are obtained from the numerical minimization of the potential Eq. (92). The decoupling line is determined using the condition $\mathbf{m}\cdot\Delta\boldsymbol{\varphi} = 0$, whereas the symmetric line follows from the condiction $\epsilon = 0$. Right: Theoretical relaxation, pure dephasing, and decoherence times T_1, T_ϕ, and T_2 as a function of applied bias current I_B, along the symmetric line (Fig. 23, left).

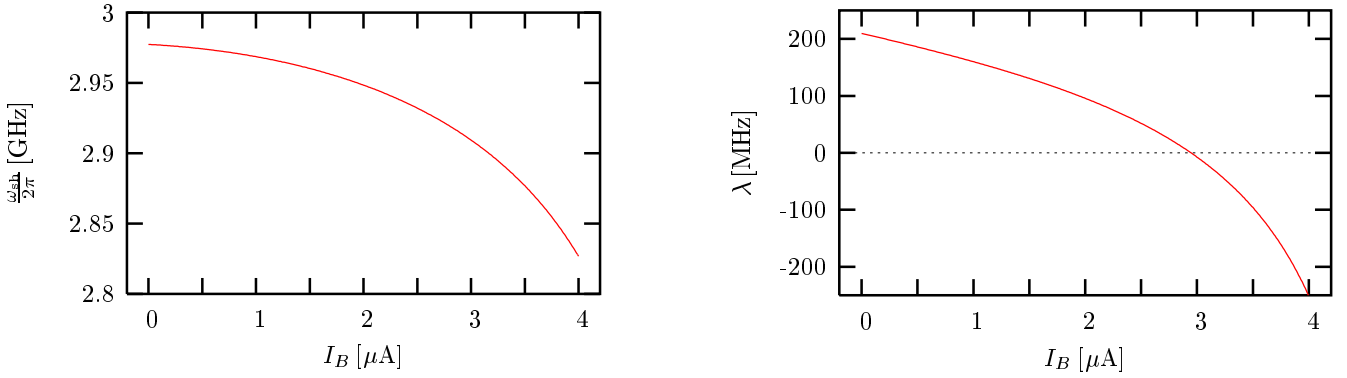


FIG. 24 Left: Plasma frequency $\omega_{\rm sh}$ as a function of the applied bias current I_B. The variation is due to the change the effective in Josephson inductances as I_B is varied. Right: Rabi frequency of the coupling between the qubit and the plasmon mode. The coupling disappears at the crossing with the decoupling line (Fig. 23), i.e., when $\mathbf{m}\cdot\Delta\boldsymbol{\varphi}=0$.

theory can be observed experimentally (Bertet *et al.*, 2004).

The symmetry breaking due to the double layer structure has another, very interesting, consequence. It causes a coupling between the qubit and an external harmonic oscillator, the plasmon mode formed by LC resonator in the SQUID (Fig. 22). This coupling can be observed as resonances in the microwave spectrum of the system. Moreover, it can be used to entangle the qubit with another degree of freedom (Chiorescu *et al.*, 2004). Here, the inductance $L_{\rm sh}$ and capacitance $C_{\rm sh}$ of the "shell" circuit (plasmon mode) are responsible for this resonator. This coupling has been studied quantitatively in the framework of the circuit theory. From the full Hamiltonian $\mathcal{H}_S$, a two-level Hamiltonian in the well-known Jaynes-Cummings form can be derived,

$$\mathcal{H}=\Delta\sigma_x+\epsilon\sigma_z+\hbar\omega_{\rm sh}\left(b^\dagger b+\frac{1}{2}\right)+\lambda\sigma_z(b+b^\dagger), \tag{106}$$

with the coupling parameter (Rabi frequency)

$$\lambda=-\sqrt{\pi}\left(\frac{\Phi_0}{2\pi}\right)^2\sqrt{\frac{Z_{\rm sh}}{R_Q}}\frac{1}{M_{\rm sh}}\mathbf{m}\cdot\Delta\boldsymbol{\varphi}. \tag{107}$$

Note that this coupling vanishes along the decoupling line (Fig. 23, left) and also rapidly with the increase of $L_{\rm sh}$. The Rabi frequency at $I_B=0$ is predicted to be $\lambda\approx 210\,$MHz. The Rabi frequency as a function of the bias current I_B, together with the plasma frequency, is plotted in Fig. 24. Strong coupling between a *charge* qubit and a quantum electromagnetic cavity formed by a SC transmission line has been observed in (Wallraff *et al.*, 2004).

E. Charge qubits

In analogy to the circuit theory for flux qubits, a general circuit theory for charge qubits will be outlined and illustrated with examples in this Section (Burkard, 2004). As in the case of the circuit theory for flux qubits, we are not restricted to a Hilbert space of the SC device which is *a priori* truncated to two levels only. The role of the self and mutual inductances in SC charge qubits have been previously studied (You *et al.*, 2001), in particular as a means of coupling two SC charge qubits (Makhlin *et al.*, 2001; Makhlin and Shnirman, 2004). Here, the self and mutual inductances in the underlying SC circuit are fully taken into account.

1. Graph theory

Note that the circuit theory for charge qubits is *dual* to that for flux qubits in the sense that the roles of chord and tree branches are interchanged,

$$\mathbf{I}_{\rm tr}=(\mathbf{I}_J,\mathbf{I}_L,\mathbf{I}_V,\mathbf{I}_Z),\quad \mathbf{I}_{\rm ch}=(\mathbf{I}_{C_J},\mathbf{I}_C,\mathbf{I}_K), \tag{108}$$

$$\mathbf{V}_{\rm tr}=(\mathbf{V}_J,\mathbf{V}_L,\mathbf{V}_V,\mathbf{V}_Z),\quad \mathbf{V}_{\rm ch}=(\mathbf{V}_{C_J},\mathbf{V}_C,\mathbf{V}_K). \tag{109}$$

The loop matrix $\mathbf{F}$ now acquires the block form,

$$\mathbf{F} = \begin{pmatrix} \mathbb{1} & \mathbf{F}_{JC} & \mathbf{F}_{JK} \\ \mathbf{0} & \mathbf{F}_{LC} & \mathbf{F}_{LK} \\ \mathbf{0} & \mathbf{F}_{VC} & \mathbf{F}_{VK} \\ \mathbf{0} & \mathbf{F}_{ZC} & \mathbf{F}_{ZK} \end{pmatrix}. \tag{110}$$

The Hamiltonian has the form

$$\mathcal{H}_S = \frac{1}{2} \left(\mathbf{Q} - \mathbf{C}_V \mathbf{V}\right)^T \mathcal{C}^{-1} \left(\mathbf{Q} - \mathbf{C}_V \mathbf{V}\right) + U(\mathbf{\Phi}), \tag{111}$$

with the potential

$$U(\mathbf{\Phi}) = -\mathbf{L}_J^{-1} \mathbf{sin}\boldsymbol{\varphi} + \frac{1}{2}\mathbf{\Phi}^T \mathbf{M}_0 \mathbf{\Phi} + \mathbf{\Phi}^T \mathbf{N} \mathbf{\Phi}_x, \tag{112}$$

where the Josephson and inductor flux variables are combined in $\mathbf{\Phi} = (\boldsymbol{\varphi}, \mathbf{\Phi}_L)$, with the vector operator of conjugate charges denoted by $\mathbf{Q}$. The coupling Hamiltonian in a Caldeira-Leggett description $\mathcal{H} = \mathcal{H}_S + \mathcal{H}_B + \mathcal{H}_{SB}$ now takes the form

$$\mathcal{H}_{SB} = \mathcal{C}^{-1} \bar{\mathbf{m}} \cdot \mathbf{Q} \sum_\alpha c_\alpha x_\alpha = \bar{\mathbf{m}} \cdot \mathcal{C}^{-1} \mathbf{Q} \sum_\alpha c_\alpha x_\alpha, \tag{113}$$

where $\mathcal{C}$ is the total capacitance matric of the circuit. The resulting Redfield equation takes the form Eq. (97) and Eq. (98), but with

$$\begin{aligned} \mathrm{Re}\Gamma^{(+)}_{lmnk} &= \frac{1}{\hbar} (\mathbf{m}\cdot\mathbf{Q})_{lm} (\mathbf{m}\cdot\mathbf{Q})_{nk} J(|\omega_{nk}|) \frac{e^{-\hbar\beta\omega_{nk}/2}}{\sinh \hbar\beta|\omega_{nk}|/2}, \\ \mathrm{Im}\Gamma^{(+)}_{lmnk} &= -\frac{1}{\hbar} (\mathbf{m}\cdot\mathbf{Q})_{lm} (\mathbf{m}\cdot\mathbf{Q})_{nk} \frac{2}{\pi} P\!\int_0^\infty \!\!d\omega \frac{J(\omega)}{\omega^2 - \omega_{nk}^2} \left(\omega - \omega_{nk} \coth \frac{\hbar\beta\omega}{2}\right), \end{aligned} \tag{114}$$

and with $\mathbf{m} = \mathcal{C}^{-1}\bar{\mathbf{m}}$. Finally, the relaxation and decoherence times in a two-level description reduce to

$$\frac{1}{T_1} = \frac{4}{\hbar} |\langle 0|\mathbf{m}\cdot\mathbf{Q}|1\rangle|^2 J(\omega_{01}) \coth \frac{\hbar\omega_{01}}{2k_B T}, \tag{115}$$

$$\frac{1}{T_2} = \frac{1}{2T_1} + \frac{1}{T_\phi}, \tag{116}$$

$$\frac{1}{T_\phi} = \frac{1}{\hbar} |\langle 0|\mathbf{m}\cdot\mathbf{Q}|0\rangle - \langle 1|\mathbf{m}\cdot\mathbf{Q}|1\rangle|^2 \left.\frac{J(\omega)}{\hbar\omega}\right|_{\omega\to 0} 2k_B T. \tag{117}$$

In the semiclassical limit, one finds

$$\frac{1}{T_1} = \frac{1}{\hbar} |\mathbf{m}\cdot\Delta\mathbf{Q}|^2 \left(\frac{\Delta}{\omega_{01}}\right)^2 J(\omega_{01}) \coth \frac{\hbar\omega_{01}}{2k_B T}, \tag{118}$$

$$\frac{1}{T_\phi} = \frac{1}{\hbar} |\mathbf{m}\cdot\Delta\mathbf{Q}|^2 \left(\frac{\epsilon}{\omega_{01}}\right)^2 \left.\frac{J(\omega)}{\hbar\omega}\right|_{\omega\to 0} 2k_B T. \tag{119}$$

The leakage rates from the logical state $k = 0, 1$ to states $n = 2, 3, \ldots$ outside the computational subspace can be estimated as

$$\frac{1}{T_L} = \frac{4}{\hbar} \sum_{n=2}^\infty |\langle k|\mathbf{m}\cdot\mathbf{Q}|n\rangle|^2 J(\omega_{nk}) \coth \frac{\hbar\omega_{nk}}{2k_B T}. \tag{120}$$

2. Single charge box

We now illustrate the circuit theory for charge qubits with some examples. The first example is the voltage-biased charge box, shown in Fig. 25. The inductance of the leads has been neglected for simplicity (no L and K branches).

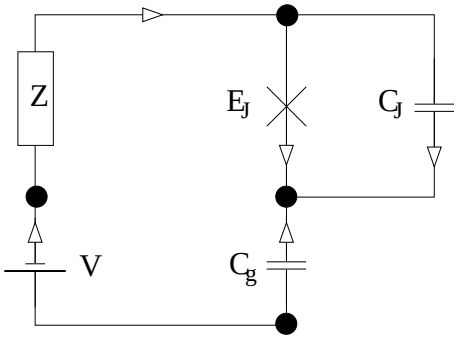


FIG. 25 Circuit graph of a single voltage-biased charge box. Branches represent a Josephson junction (E_J), capacitances (C_J and C_g), a voltage source V, and the impedance Z. The nodes are shown as black dots; the node connecting the junction (E_J) to the gate capacitance C_g represents the SC island.

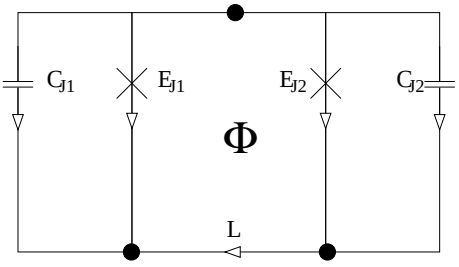


FIG. 26 A flux-controlled Josephson junction.

The tree of the graph is given by the Josephson, voltage source, and impedance branches. For the loop matrices, we simply find $\mathbf{F}_{JC} = \mathbf{F}_{VC} = \mathbf{F}_{ZC} = 1$. With the capacitances $\mathcal{C} \equiv C_{\rm tot} = C_J + C_g$ and $C_V = C_g$, we arrive at the Hamiltonian,

$$\mathcal{H}_S = \frac{(Q_J + C_g V)^2}{2C_{\rm tot}} + E_J \cos\varphi. \tag{121}$$

The coupling to the environment is characterized by $\mathbf{m} = (C_g/C_{\rm tot})$. As an example, we give here the relaxation and dephasing times, with $m = |\mathbf{m}| = C_g/C_{\rm tot}$,

$$\frac{1}{T_1} = 2\pi m^2 4|\langle 0|n|1\rangle|^2 \frac{4{\rm Re}Z(\omega_{01})}{R_Q}\omega_{01}\coth\frac{\hbar\omega_{01}}{2k_BT}, \tag{122}$$

$$\frac{1}{T_\phi} = 2\pi m^2|\langle 0|n|0\rangle - \langle 1|n|1\rangle|^2 \frac{4{\rm Re}Z(0)}{R_Q}\frac{2k_BT}{\hbar}, \tag{123}$$

where $n = Q/2e$ and $R_Q = h/e^2$. In the semiclassical limit, $\langle 0|n|1\rangle \approx (1/2)(\Delta/\omega_{01})\Delta n$ and $\langle 0|n|0\rangle - \langle 1|n|1\rangle \approx (\epsilon/\omega_{01})\Delta n$. With $\Delta n \approx 1$, we reproduce the results in (Makhlin *et al.*, 2001). Typical leakage rates are of the form of $1/T_1$, with the matrix element replaced by $|\langle 0|n|k\rangle|$ and $|\langle 1|n|k\rangle|$, where $k \geq 2$ labels a state other than the two qubit states, and with ω_{01} replaced by ω_{lk} $(l = 0, 1)$.

3. Flux-controlled Josephson junction

. A flux-controlled Josephson junction is a SC loop with two junctions which acts as an effective Josephson junction with a flux-dependent Josephson energy (Makhlin *et al.*, 1999). The circuit Fig. 26 we use to describe the the flux-controlled junction comprises a chord inductance (K) with inductance L. The tree consists of the two Josephson branches. The only relevant loop matrix is $\mathbf{F}_{JK} = \begin{pmatrix} 1 & -1 \end{pmatrix}^T$. In the limit $L \to 0$, and if $E_{J1} = E_{J2}$, we find $\mathbf{F}_{JK}^T\boldsymbol{\varphi} + \Phi_x = \varphi_1 - \varphi_2 + \Phi \to 0$, which leads us to the Hamiltonian

$$\mathcal{H}_S = \frac{Q^2}{2\bar{C}} - E_J(\Phi)\cos\varphi, \tag{124}$$

where $\varphi = \varphi_1 + \pi\Phi/\Phi_0$, $\bar{C} = C_{J1} + C_{J2}$, and $E_J(\Phi) = 2E_J\cos(2\pi\Phi/\Phi_0)$.

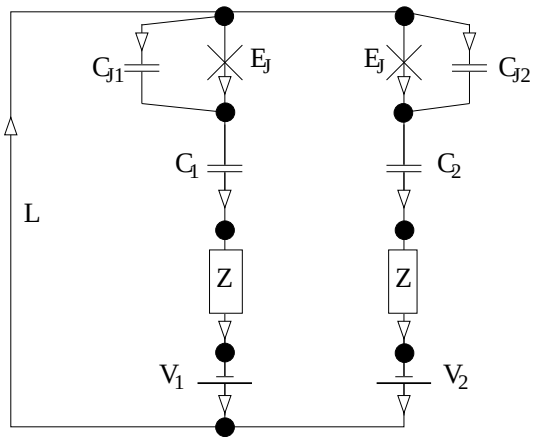


FIG. 27 Two inductively coupled charge boxes.

4. Inductively coupled charge boxes

We now turn to the case of two charge boxes of the type discussed in Sec. IV.E.2, coupled via an inductive loop (Makhlin *et al.*, 1999, 2001), as shown in Fig. 27. Here, the tree consists of all Josephson, voltage source, and impedance branches, plus the inductive branch L, and the loop matrices are

$$\mathbf{F}_{JC} = \mathbf{F}_{VC} = \mathbf{F}_{ZC} = \begin{pmatrix} 1 & 0 \\ 0 & 1 \end{pmatrix}, \; \mathbf{F}_{LC} = \begin{pmatrix} 1 & 1 \end{pmatrix}. \tag{125}$$

With the two capacitance matrices $\mathbf{C} = \mathrm{diag}(C_1, C_2)$ and $\mathbf{C}_J = \mathrm{diag}(C_{J1}, C_{J2})$, we find $\mathbf{C}_{\rm tot} = \mathbf{C} + \mathbf{C}_J$, $\mathbf{C}_{JV} = \mathbf{C}$, $\mathbf{C}_{JL} = \mathbf{C}_{LV}^T = (C_1, C_2)^T$, and $\mathbf{C}_L = C_1 + C_2$. The vector $\bar{\mathbf{m}}$ consists of the two parts $\mathbf{m}_J = C$ and $\mathbf{m}_L = \begin{pmatrix} C_1 & C_2 \end{pmatrix}$. With Eq. (111) and the inverse of the total capacitance matrix,

$$\mathcal{C}^{-1} = \frac{1}{\gamma} \begin{pmatrix} (C_1+C_2)C_{J2} - C_2^2 & C_1 C_2 & -C_1 C_{J2} \\ C_1 C_2 & (C_1+C_2)C_{J1} - C_1^2 & -C_2 C_{J1} \\ -C_1 C_{J2} & -C_2 C_{J1} & C_{J1} C_{J2} \end{pmatrix} \equiv \begin{pmatrix} C^{-1}_{\mathrm{eff},1} & C^{-1}_{\mathrm{eff},12} & C^{-1}_{\mathrm{eff},L1} \\ C^{-1}_{\mathrm{eff},12} & C^{-1}_{\mathrm{eff},2} & C^{-1}_{\mathrm{eff},L2} \\ C^{-1}_{\mathrm{eff},L1} & C^{-1}_{\mathrm{eff},L2} & C^{-1}_{\mathrm{eff},L} \end{pmatrix}, \tag{126}$$

where $\gamma = (C_1+C_2)C_{J1}C_{J2} - C_1^2 C_{J2} - C_2^2 C_{J1}$, the Hamiltonian of the coupled system can be written as,

$$\begin{aligned} \mathcal{H}_S \;=\; & \sum_{i=1,2} \left(\frac{(Q_{Ji} + C_i V_i)^2}{2C_{\mathrm{eff},i}} + E_{Ji} \cos\varphi_i \right) + \frac{(Q_L + C_1 V_1 + C_2 V_2)^2}{2C_{\mathrm{eff},L}} + \frac{\Phi_L^2}{2L} \\ & + \frac{(Q_{J1} + C_1 V_1)(Q_{J2} + C_2 V_2)}{C_{\mathrm{eff},12}} - \sum_{i=1,2} \frac{(Q_{Ji} + C_i V_i)(Q_L + C_1 V_1 + C_2 V_2)}{C_{\mathrm{eff},Li}}. \end{aligned} \tag{127}$$

While the last term in Eq. (127) couples each qubit to the LC mode associated with the inductor L, and is thus responsible for the inductive coupling of the qubits, the second last term provides a direct capacitive coupling between the qubits. In the limit $C_i \ll C_{Ji}$, we reproduce the results of (Makhlin *et al.*, 2001); however, there are additional terms of order C_i/C_{Ji}, in particular the new term $\propto 1/C_{\mathrm{eff},12}$ in the Hamiltonian that capacitively couples the qubits directly. Since the coupled system involves at least four levels (more if excited states of the LC coupling circuit or higher qubit levels are included), it can no longer be described by a two-level Bloch equation with parameters T_1 and T_2. We can however fix one of the qubits to be in a particular state, say $|0\rangle$, and then look at the "decoherence rates" of the other qubit. To lowest order in C_i/C_{Ji}, these rates due to the impedance Z_i have the form ($q_i = C_i/(C_1+C_2)$)

$$\frac{1}{T_1} \;=\; 2\pi q_i^2 4 |\langle 00|n_L|10\rangle|^2 \frac{4\mathrm{Re}Z_i(\omega_{01})}{R_Q} \omega_{01} \coth\frac{\hbar\omega_{01}}{2k_B T}, \tag{128}$$

$$\frac{1}{T_\phi} \;=\; 2\pi q_i^2 |\langle 00|n_L|00\rangle - \langle 10|n_L|10\rangle|^2 \frac{4\mathrm{Re}Z_i(0)}{R_Q} \frac{2k_B T}{\hbar}. \tag{129}$$

F. Multiple sources of decoherence

In this Section, we show that the total decoherence and relaxation rates of a quantum system in the presence of several decoherence sources are *not* necessarily the sums of the rates due to each of the mechanisms separately, and that the corrections to additivity (mixing terms) can have both signs (Burkard and Brito, 2004). To this end, we investigate the decoherence due to several sources in superconducting (SC) flux qubits; the general idea of the present analysis may however be applied to other systems as well.

1. Dissipative dynamics

As an example, the gradiometer qubit drawn in Fig. 28 with $n = 3$ junctions will be discussed. The gradiometer qubit is controlled by applying a magnetic flux Φ_c to the small loop on the left by driving a current I_{B1} in a coil next to it, and simultaneously by applying a magnetic flux Φ on one side of the gradiometer using I_{B2}. The classical equations of motion of the SC circuit have the form

$$\mathbf{C}\ddot{\boldsymbol{\varphi}} = -\frac{\partial U}{\partial \boldsymbol{\varphi}} - \mathbf{M} * \boldsymbol{\varphi}, \tag{130}$$

where $\mathbf{C}$ is the capacitance matrix, U the potential, and $\mathbf{M}(t)$ the dissipation matrix. The convolution is defined as $(f*g)(t) = \int_{-\infty}^{t} f(t-\tau)g(\tau)d\tau$. The dissipation matrix in the Fourier representation can be found from circuit theory (Burkard *et al.*, 2004b) and has the form

$$\mathbf{M}(\omega) = \bar{\mathbf{m}}\bar{\mathbf{L}}_Z(\omega)^{-1}\bar{\mathbf{m}}^T = \bar{\mathbf{m}}\left(\mathbf{L}_Z(\omega) + \mathbf{L}_c\right)^{-1}\bar{\mathbf{m}}^T, \tag{131}$$

where $\bar{\mathbf{m}}$ and $\mathbf{L}_c$ denote real matrices that can be obtained from the circuit inductances. One can assume the matrices $\mathbf{Z}$ and $\mathbf{L}_Z$ to be diagonal because the impedances Z_i are independent.

A Caldeira-Leggett Hamiltonian $\mathcal{H} = \mathcal{H}_S + \mathcal{H}_B + \mathcal{H}_{SB}$ can be constructed that reproduces the classical dissipative equation of motion, Eq. (130), and that is composed of parts for the system (S), given in Eq. (91), for $m \geq 1$ harmonic oscillator baths (B), and for the system-bath (SB) coupling,

$$\mathcal{H}_B = \sum_{j=1}^{m}\sum_{\alpha}\left(\frac{p_{\alpha j}^2}{2m_{\alpha j}} + \frac{1}{2}m_{\alpha j}\omega_{\alpha j}^2 x_{\alpha j}^2\right), \tag{132}$$

$$\mathcal{H}_{SB} = \sum_{\alpha}\boldsymbol{\varphi}^T\mathbf{c}_\alpha\mathbf{x}_\alpha, \tag{133}$$

where $\mathbf{x}_\alpha = (x_{\alpha 1}, \ldots, x_{\alpha m})$, and $\mathbf{c}_\alpha$ is a real $n \times m$ matrix. Defining the matrix spectral density $\mathbf{J}(\omega)$ of the environment, where $\boldsymbol{\delta}_{ij}(\mathbf{X}) \equiv \delta(\mathbf{X}_{ij})$, one obtains the relation

$$\mathbf{J}(\omega) \equiv \frac{\pi}{2}\sum_{\alpha}\mathbf{c}_\alpha\mathbf{m}_\alpha^{-1}\boldsymbol{\omega}_\alpha^{-1}\boldsymbol{\delta}(\omega - \boldsymbol{\omega}_\alpha)\mathbf{c}_\alpha^T, = \left(\frac{\Phi_0}{2\pi}\right)^2 \mathrm{Im}\mathbf{M}(\omega) = \sum_{j=1}^{m} J_j(\omega)\mathbf{m}_j(\omega)\mathbf{m}_j(\omega)^T, \tag{134}$$

where the spectral decomposition (with the eigenvalues $J_j(\omega) > 0$ and the real and normalized eigenvectors $\mathbf{m}_j(\omega)$) of the real, positive, and symmetric matrix $\mathrm{Im}\mathbf{M}(\omega)$ has been used. The integer $m \leq n, n_Z$ denotes the maximal rank of

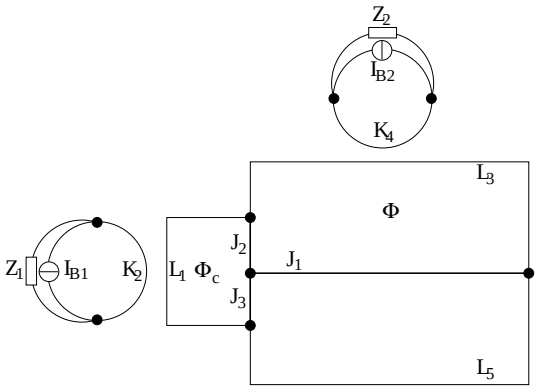


FIG. 28 Circuit graph of the gradiometer qubit (Koch *et al.*, 2004), under the influence of noise from two sources Z_1 and Z_2. Branches of the graph denote Josephson junctions J_i, inductances L_i and K_i, current sources I_{Bi}, and external impedances Z_i, and are connected by the nodes (black dots) of the graph. Inset: A resistively-shunted Josephson junction (RSJ) J_i, represented by a thick line in the circuit graph, is modeled by an ideal junction (cross) with critical current I_{ci}, shunt resistance R_i, and junction capacitance C_i.

$\mathrm{Im}\mathbf{M}(\omega)$, i.e., $m = \max_\omega\left(\mathrm{rank}\left[\mathrm{Im}\mathbf{M}(\omega)\right]\right)$. Using Eq. (134), and choosing $c_{\alpha ij} = \gamma_{\alpha j}\mathbf{m}_i(\omega_{\alpha j})$, we find that $J_j(\omega)$ is the spectral density of the j-th bath of harmonic oscillators in the environment, $J_j(\omega) = (\pi/2)\sum_\alpha(\gamma_{\alpha j}^2/m_{\alpha j}\omega_{\alpha j})\delta(\omega-\omega_{\alpha j})$.

From this model one obtains the Redfield equation, Eqs. (97), with a Redfield tensor, Eq. (98), of the form

$$\begin{aligned}\mathrm{Re}\Gamma^{(+)}_{lmnk} &= \boldsymbol{\varphi}_{lm}^T\mathbf{J}(|\omega_{nk}|)\boldsymbol{\varphi}_{nk}\frac{e^{-\beta\omega_{nk}/2}}{\sinh(\beta|\omega_{nk}|/2)},\\ \mathrm{Im}\Gamma^{(+)}_{lmnk} &= -\frac{2}{\pi}P\int_0^\infty\frac{\boldsymbol{\varphi}_{lm}^T\mathbf{J}(\omega)\boldsymbol{\varphi}_{nk}}{\omega^2-\omega_{nk}^2}\left(\omega-\omega_{nk}\coth\frac{\beta\omega}{2}\right),\end{aligned} \tag{135}$$

where $\boldsymbol{\varphi}_{nk} = \langle n|\boldsymbol{\varphi}|k\rangle$. For two levels $n = 0, 1$, and within the secular approximation, the relaxation and decoherence rates T_1^{-1} and T_2^{-1} are found to be

$$T_1^{-1} = 4\boldsymbol{\varphi}_{01}^\dagger\mathbf{J}(\omega_{01})\boldsymbol{\varphi}_{01}\coth\left(\frac{\beta\omega_{01}}{2}\right) = 4\sum_{j=1}^m|\boldsymbol{\varphi}_{01}\cdot\mathbf{m}_j(\omega_{01})|^2J_j(\omega_{01})\coth\left(\frac{\beta\omega_{01}}{2}\right), \tag{136}$$

$$T_\phi^{-1} = \frac{2}{\beta}\lim_{\omega\to0}(\boldsymbol{\varphi}_{00}-\boldsymbol{\varphi}_{11})^\dagger\frac{\mathbf{J}(\omega)}{\omega}(\boldsymbol{\varphi}_{00}-\boldsymbol{\varphi}_{11}) = \frac{2}{\beta}\sum_{j=1}^m|\mathbf{m}_j(0)\cdot(\boldsymbol{\varphi}_{00}-\boldsymbol{\varphi}_{11})|^2\left.\frac{J_j(\omega)}{\omega}\right|_{\omega\to0}, \tag{137}$$

where we have used the spectral decomposition, Eq. (134), to obtain the second equality in each line.

2. Mixing Terms

In the case where $\mathbf{L}_\mathrm{c}$ is diagonal, or if its off-diagonal elements can be neglected because they are much smaller than $\mathbf{L}_Z(\omega)$ for all frequencies ω, one finds, using Eq. (131), that the contributions due to different impedances Z_i are independent, thus $m = n_Z$ and $\mathbf{M}(\omega) = \bar{\mathbf{m}}\bar{\mathbf{L}}_Z(\omega)^{-1}\bar{\mathbf{m}}^T = \sum_j\bar{\mathbf{m}}_j\bar{\mathbf{m}}_j^T i\omega/(Z_j(\omega)+i\omega L_{jj})$, where $\mathbf{m}_j = \bar{\mathbf{m}}_j$ is simply the j-th column of the matrix $\bar{\mathbf{m}}$ and L_{jj} is the j-th diagonal entry of $\mathbf{L}_\mathrm{c}$. As a consequence, the total rates $1/T_1$ and $1/T_\phi$ are the sums of the individual rates, $1/T_1^{(j)}$ and $1/T_\phi^{(j)}$, where

$$\frac{1}{T_1^{(j)}} = 4\left(\frac{\Phi_0}{2\pi}\right)^2|\boldsymbol{\varphi}_{01}\cdot\bar{\mathbf{m}}_j|^2\mathrm{Re}\frac{\omega_{01}\coth(\beta\omega_{01}/2)}{Z_j(\omega_{01})+i\omega_{01}L_{jj}}, \tag{138}$$

$$\frac{1}{T_\phi^{(j)}} = \frac{2}{\beta}\left(\frac{\Phi_0}{2\pi}\right)^2|\bar{\mathbf{m}}_j\cdot(\boldsymbol{\varphi}_{00}-\boldsymbol{\varphi}_{11})|^2\mathrm{Re}\frac{1}{Z_j(0)}. \tag{139}$$

In general, the situation is more complicated because current fluctuations due to different impedances are mixed by the presence of the circuit. In the regime $\mathbf{L}_\mathrm{c}\ll\mathbf{L}_Z(\omega)$, $\bar{\mathbf{L}}_Z^{-1}$ can be expanded as

$$\bar{\mathbf{L}}_Z^{-1} = (\mathbf{L}_Z(\omega)+\mathbf{L}_\mathrm{c})^{-1} = \mathbf{L}_Z^{-1}-\mathbf{L}_Z^{-1}\mathbf{L}_\mathrm{c}\mathbf{L}_Z^{-1}+\mathbf{L}_Z^{-1}\mathbf{L}_\mathrm{c}\mathbf{L}_Z^{-1}\mathbf{L}_\mathrm{c}\mathbf{L}_Z^{-1}-\cdots. \tag{140}$$

The series Eq. (140) can be partially resummed,

$$\bar{\mathbf{L}}_Z^{-1}(\omega) = \mathrm{diag}\left(\frac{i\omega}{Z_j(\omega)+i\omega L_{jj}}\right)+\mathbf{L}_\mathrm{mix}^{-1}(\omega), \tag{141}$$

where the first term simply gives rise to the sum of the individual rates, as in Eqs. (138) and (139), while the second term gives rise to mixed terms in the total rates. The rates can therefore be decomposed as ($X = 1, 2, \phi$)

$$\frac{1}{T_X} = \sum_j\frac{1}{T_X^{(j)}}+\frac{1}{T_X^{(\mathrm{mix})}}. \tag{142}$$

One finds for the mixing term in the relaxation rate

$$\frac{1}{T_1^{(\mathrm{mix})}} = 4\left(\frac{\Phi_0}{2\pi}\right)^2\boldsymbol{\varphi}_{01}^\dagger\bar{\mathbf{m}}\mathrm{Im}\mathbf{L}_\mathrm{mix}^{-1}(\omega_{01})\bar{\mathbf{m}}^T\boldsymbol{\varphi}_{01}\coth\left(\frac{\beta\omega_{01}}{2}\right). \tag{143}$$

One can show that there is no mixing term in the pure dephasing rate, i.e., $1/T_\phi^{(\mathrm{mix})} = 0$, and hence $T_2^{(\mathrm{mix})} = 2T_1^{(\mathrm{mix})}$.

In the case of two external impedances, $n_Z = 2$, Eq. (140) can be completely resummed, with the result

$$\mathbf{L}_{\rm mix}^{-1}(\omega)=\frac{L_{12}}{(Z_1(\omega)/i\omega+L_{11})(Z_2(\omega)/i\omega+L_{22})-L_{12}^2}\begin{pmatrix}\frac{L_{12}}{Z_1(\omega)/i\omega+L_{11}} & -1\\ -1 & \frac{L_{12}}{Z_2(\omega)/i\omega+L_{22}}\end{pmatrix}\approx-\frac{\omega^2L_{12}}{Z_1(\omega)Z_2(\omega)}\sigma_x, \tag{144}$$

where L_{ij} are the matrix elements of $\mathbf{L}_{\rm c}$ and where the approximation in Eq. (144) holds up to $O(\mathbf{Z}^{-3})$. In lowest order in $1/Z_i$, one finds,

$$\frac{1}{T_1^{(\rm mix)}}=-\left(\frac{\Phi_0}{2\pi}\right)^2{\rm Im}\frac{8\varphi_{12}\omega_{01}^2L_{12}}{Z_1(\omega_{01})Z_2(\omega_{01})}\coth\left(\frac{\beta\omega_{01}}{2}\right). \tag{145}$$

with $\varphi_{12}=(\boldsymbol{\varphi}_{01}\cdot\bar{\mathbf{m}}_1)(\boldsymbol{\varphi}_{01}\cdot\bar{\mathbf{m}}_2)$.

If $R_i\equiv Z_i(\omega_{01})$ are real (pure resistances) then, as predicted above, the imaginary part of the second-order term in Eq. (144) vanishes, and we resort to third order,

$${\rm Im}\mathbf{L}_{\rm mix}^{-1}=\frac{\omega^3L_{12}}{R_1R_2}\begin{pmatrix}\frac{L_{12}}{R_1} & \frac{L_{11}}{R_1}+\frac{L_{22}}{R_2}\\ \frac{L_{11}}{R_1}+\frac{L_{22}}{R_2} & \frac{L_{12}}{R_2}\end{pmatrix}, \tag{146}$$

neglecting terms in $O(R_j^{-4})$. If $L_{12}\ll L_{jj}$, we obtain ${\rm Im}\mathbf{L}_{\rm mix}^{-1}\approx(\omega^3L_{12}/R_1R_2)(L_{11}/R_1+L_{22}/R_2)\sigma_x$, and

$$\frac{1}{T_1^{(\rm mix)}}=\left(\frac{\Phi_0}{2\pi}\right)^2\frac{8\omega_{01}^3L_{12}}{R_1R_2}\left(\frac{L_{11}}{R_1}+\frac{L_{22}}{R_2}\right)\varphi_{12}\coth\left(\frac{\beta\omega_{01}}{2}\right). \tag{147}$$

For the gradiometer qubit (Fig. 28), we find $L_{12}\approx M_{12}M_{13}M_{34}/L_1L_3$, $L_{11}\approx L_2$, $L_{22}\approx L_4$, where L_k denotes the self-inductance of branch X_k (X=L or K) and M_{kl} is the mutual inductance between branches X_k and X_l, and where we assume $M_{ij}\ll L_k$. The ratio between the mixing the single-impedance contribution scales as

$$\frac{1/T_1^{(\rm mix)}}{1/T_1^{(j)}}\approx\frac{\omega_{01}^2L_{12}L}{R^2}, \tag{148}$$

where we have assumed $R_1\approx R_2\equiv R$, $L_{11}\approx L_{22}\equiv L$, and $\boldsymbol{\varphi}_{01}\cdot\bar{\mathbf{m}}_1\approx\boldsymbol{\varphi}_{01}\cdot\bar{\mathbf{m}}_2$.

The relaxation time T_1 was calculated at a temperature $T\ll\hbar\omega_{01}/k_B$ for the circuit Fig. 28, for a critical current $I_c=0.3\,\mu$A for all junctions, and for the inductances $L_1=30\,$pH, $L_3=680\,$pH, $L_2=L_4=12\,$nH, $M_{12}\simeq\sqrt{L_1L_2}$, $M_{34}\simeq\sqrt{L_3L_4}$ (strong inductive coupling), $M_{35}=6\,$pH, with $\omega_{01}=2\pi\cdot30\,$GHz, and with the impedances $Z_1=R$, $Z_2=R+iR_{\rm im}$, where R and $R_{\rm im}=\pm10\,$kΩ are real ($R_{\rm im}>0$ corresponds to an inductive, $R_{\rm im}<0$ to a capacitive character of Z_i). In Fig. 29, T_1 was plotted with and without mixing for a fixed value of $M_{13}=0.5\,$pH and a range of $R={\rm Re}Z_i$. In the inset of Fig. 29, T_1 (with mixing) and $((T_1^{(1)})^{-1}+(T_1^{(2)})^{-1})^{-1}$ (without mixing) are plotted for $R=75\,\Omega$ for a range of mutual inductances M_{13}; for this plot, the double minima of the potential U and $\boldsymbol{\varphi}_{01}$ were computed numerically for each value of M_{13}. The plots (Fig. 29) clearly show that summing the decoherence rates without taking into account mixing term can both underestimate or overestimate the relaxation rate $1/T_1$, leading to either an over- or underestimate of the relaxation and decoherence times T_1 and T_2.

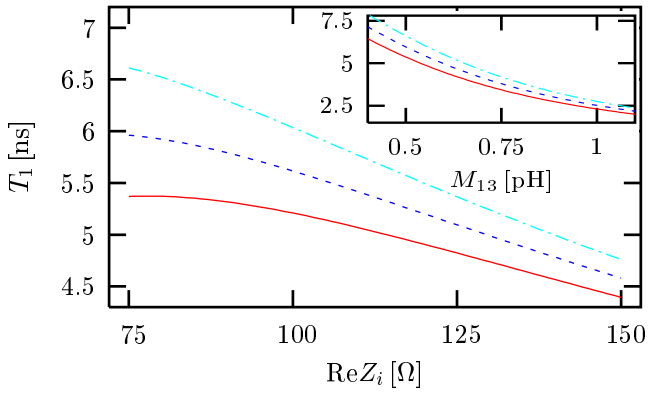


FIG. 29 The relaxation rate T_1 without the mixing term (dashed blue line), and including the mixing term for $R_{\rm im}=+10\,$kΩ (solid red line) and $R_{\rm im}=-10\,$kΩ (dot-dashed light blue line), for $M_{13}=0.5\,$pH as a function of ReZ_i. Inset: T_1 for $R={\rm Re}Z_i=75\,\Omega$ for a range of mutual inductances M_{13}.

V. ENTANGLEMENT

A composite system is entangled if its wavefunction Ψ cannot be expressed as a tensor product $\Psi_A \otimes \Psi_B$ of wavefunctions Ψ_A and Ψ_B for the parts A and B of the system (a more general, but similar, definition exists for mixed states). A variety of quantum communication scenarios (Bennett and DiVincenzo, 2000), some of which have been implemented successfully in quantum optics, require maximally entangled states of two qubits, also known as EPR pairs (Einstein *et al.*, 1935), such as the spin singlet,

$$|S\rangle = \frac{1}{\sqrt{2}} \left(|\uparrow\downarrow\rangle - |\downarrow\uparrow\rangle \right). \tag{149}$$

The triplet state $|T_0\rangle = |\uparrow\downarrow\rangle + |\downarrow\uparrow\rangle$ is another maximally entangled state, while the other two triplet states $|T_+\rangle = |\uparrow\uparrow\rangle$ and $|T_-\rangle = |\downarrow\downarrow\rangle$ are not entangled. An important feature of these states is that they are non-local, in the sense that they violate Bell's inequalities (Bell, 1966; Mermin, 1993). A universal quantum computer can, by definition, produce arbitrary quantum states, and, in particular, entangled ones such as the singlet $|S\rangle$. E.g., the square root of swap gate S, see Eq. (8), has the ability to turn the unentangled state $|\uparrow\downarrow\rangle$ into a maximally entangled one, $S|\uparrow\downarrow\rangle = (|\uparrow\downarrow\rangle - i|\downarrow\uparrow\rangle)/(1-i)$, which is equivalent (up to a single-qubit operation) to the singlet. There may be cases in which only certain entangled states are required for quantum communication, while quantum computation itself does not need to be performed. In this case, a physical device dedicated to the task of producing entangled states of some sort may be sufficient. We call devices of this sort *entanglers* (Burkard *et al.*, 2000b) and discuss a number of conceivable implementations of entanglers in solid state systems below.

Experiments with entangled photons have tested Bell's inequalities (Aspect *et al.*, 1982), and various quantum communication protocols, such as dense coding (Mattle *et al.*, 1996) and quantum teleportation (Boschi *et al.*, 1998; Bouwmeester *et al.*, 1997). However, none of these protocols been implemented so far with massive particles (such as electrons).

Unfactorizable states like Eq. (149) are very common in solid-state systems. Interacting many-particle systems possess very complicated and entangled ground states. Not all of these are necessarily useful for quantum information processing, though, because (i) it is essential that there is a physical mechanism to extract and separate a pair of entangled particles from the many-body system in such a way that they can be used for quantum communication, and (ii) for indistinguishable particles, not all states that "look entangled" really are. A measure of entanglement which excludes pure antisymmetrization was defined in (Schliemann *et al.*, 2001a,b).

A. Production of entangled electrons

1. Superconductor-normal junctions

A superconductor (SC) with s-wave pairing symmetry contains an entire "reservoir" of spin singlet states as in Eq. (149) in the form of Cooper pairs that form the SC condensate (Schrieffer, 1964). It is thus natural to think that such a system can act as a source of spin-entangled electrons. A proposed setup (Recher *et al.*, 2001) is shown in Fig. 30. The SC is held at the chemical potential μ_S, and is weakly coupled by tunnel barriers to two separate quantum dots D_1 and D_2 which are in turn weakly coupled to Fermi liquid leads L_1 and L_2, both held at the same chemical potential $\mu_1 = \mu_2$. The tunneling amplitudes between SC and dots, and dots and leads, are denoted by T_{SD} and T_{DL}.

Andreev tunneling is a process in which two electrons (one with spin up and one with spin down) can tunnel coherently through a normal barrier, while at the same time, single-particle tunneling as suppressed (Hekking *et al.*, 1993). The setup Fig. 30 with the intermediate quantum dots is designed to force two electrons from a Cooper pair to tunnel coherently into *separate* leads rather than both into the same lead. The double occupation of a quantum dot is suppressed by the Coulomb blockade mechanism (Kouwenhoven *et al.*, 1997c).

The flow of entangled electrons from the SC via the dots to the leads is controlled by applying a bias voltage $\Delta\mu = \mu_S - \mu_l > 0$. The chemical potentials ϵ_1 and ϵ_2 of the two quantum dots can be tuned by external gate voltages (Kouwenhoven *et al.*, 1997c) such that the coherent tunneling of two electrons into different leads is at resonance, while coherent tunneling of two electrons into the same lead is suppressed by the on-site Coulomb repulsion U of a quantum dot.

The relevant parameters describing the device and the desired regime of operation are discussed in (Recher *et al.*, 2001). It is required that the barriers of the dots are asymmetric, $|T_{SD}| \ll |T_{DL}|$, temperature is sufficiently small, $\Delta\mu > k_B T$, and $\Delta, U, \delta\epsilon > \Delta\mu > \gamma_l, k_B T$, and $\gamma_l > \gamma_S$, where $\delta\epsilon$ is the single-level spacing of the dots, Δ is the SC energy gap, and $\gamma_l = 2\pi\nu_l |T_{DL}|^2$ are the dot-lead tunnel rates. The figure of merit for the device is the ratio between

the desired current $I_1$of pairwise entangled electrons tunneling into *different* leads and the unwanted current I_2 of electron pairs that end up in the *same* lead (Recher *et al.*, 2001),

$$\frac{I_1}{I_2} = \frac{2\mathcal{E}^2}{\gamma^2}\left[\frac{\sin(k_F\delta r)}{k_F\delta r}\right]^2 e^{-2\delta r/\pi\xi}, \qquad \frac{1}{\mathcal{E}} = \frac{1}{\pi\Delta} + \frac{1}{U}, \tag{150}$$

where k_F denotes the Fermi wavevector, $\gamma = \gamma_1 + \gamma_2$, and ξ the SC coherence length.

The desired current I_1 decreases exponentially with increasing distance $\delta r = |\mathbf{r}_1 - \mathbf{r}_2|$ between the tunneling points on the SC, the scale given by the superconducting coherence length ξ. With ξ typically being on the order of μm, this does not pose severe restrictions for a conventional s-wave SC. In the important case $0 \leq \delta r \sim \xi$ the suppression is only polynomial $\propto 1/(k_F\delta r)^2$, with k_F being the Fermi wavevector in the SC. One also observes that the effect of the quantum dots consists in the suppression factor $(\gamma/\mathcal{E})^2$ for tunneling into the same lead. One therefore has to impose the additional condition $k_F\delta r < \mathcal{E}/\gamma$, which can be satisfied for small dots with $\mathcal{E}/\gamma \approx 100$ and $k_F^{-1} \approx 1$ Å.

As an alternative to quantum dots as a means to separate the entangled electrons from the SC, it hsa been proposed to use a Luttinger liquid (see Sec. V.A.2 below) or a resistive lead where the dynamical Coulomb blockade effect helps to separate the electron pair (Recher and Loss, 2003).

2. Superconductor–Luttinger liquid junctions

In the Andreev entangler (Sec. V.A.1), entangled electron pairs are separated by the Coulomb repulsion in quantum dots that are attached to the SC which acts as a source of entangled spin singlets. In related work (Recher and Loss, 2002a,b) and (Bena *et al.*, 2002), it was suggested that the strong Coulomb interactions in a one-dimensional conductor, forming a Luttinger liquid (Tsvelik, 2003) can play the same role. There is good experimental evidence for Luttinger liquid (LL) behavior in carbon nanotubes (Bockrath *et al.*, 1999).

The setting discussed in (Recher and Loss, 2002a,b) consists of a conventional s-wave SC tunnel-coupled to the center (bulk) of two spatially separated, for all practical purposes infinitely extended, one-dimensional wires (e.g., carbon nanotubes) each forming a separate LL. While the Coulomb interaction within each wire is essential for the separation of entangled pairs into distinct wires, it is assumed that the interaction between carriers in different wires is negligible. In the absence of backscattering, the low energy excitations of the LL are long-wavelength charge and spin density oscillations propagating with velocities $u_\rho = v_F/K_\rho$ for the charge and $u_\sigma = v_F$ for the spin (Schulz, 1990), where v_F is the Fermi velocity and $K_\rho < 1$ due to interaction. Transfer of electrons from the SC to the LL-leads is described by a tunneling Hamiltonian,

$$H_T = t_0 \sum_{ns} \psi^\dagger_{ns}\Psi_s(\mathbf{r}_n) + \text{H.c.}, \tag{151}$$

where $\Psi_s(\mathbf{r}_n)$ annihilates an electron with spin s at the point $\mathbf{r}_n$ on the SC nearest to the LL-lead $n = 1, 2$, and $\psi^\dagger_{ns}$ creates it again with same spin and amplitude t_0 at the point x_n in LL n. By applying a bias $\mu = \mu_S - \mu_l$ between the SC, with chemical potential μ_S, and the leads, held at the same chemical potential μ_l, a stationary current of pairwise spin-entangled electrons can flow from the SC to the leads.

As in the case of the Andreev entangler with attached quantum dots, the performance of this device can be quantified by the ratio between the two competing currents I_1 and I_2 (see Sec. V.A.1). From a T-matrix calculation (Recher and Loss, 2002a,b), one obtains in leading order in μ/Δ and at zero temperature,

$$I_1 = \frac{I_1^0}{\Gamma(2\gamma_\rho + 2)}\frac{v_F}{u_\rho}\left[\frac{2\Lambda\mu}{u_\rho}\right]^{2\gamma_\rho}, \quad I_1^0 = 4\pi e\gamma^2\mu\,\frac{\sin^2(k_F\delta r)}{(k_F\delta r)^2}e^{-2\delta r/\pi\xi}, \tag{152}$$

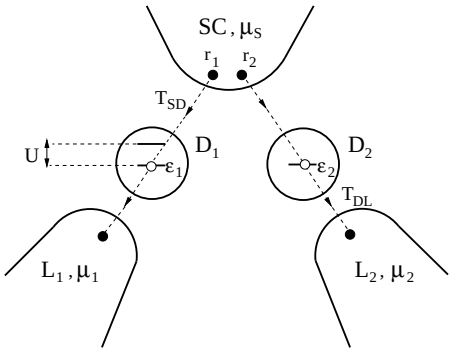


FIG. 30 The Andreev entangler. A Cooper pair is split up into two entangled electrons which hop with amplitude T_{SD} from two points $\mathbf{r}_1$, $\mathbf{r}_2$ of the superconductor, SC, (distance $\delta r = |\mathbf{r}_1 - \mathbf{r}_2|$) onto two dots $D_{1,2}$ by means of Andreev tunneling. The dots are coupled to normal leads $L_{1,2}$ with tunneling amplitude T_{DL}. In order to maximize the efficiency of the device, we require asymmetric barriers, $|T_{SD}|/|T_{DL}| \ll 1$. The chemical potentials of the SC and leads are μ_l and μ_S.

where Γ is the Gamma function, Λ a short distance cut-off on the order of the lattice spacing in the LL, $\gamma = 2\pi\nu_S\nu_l|t_0|^2$ the probability per spin to tunnel from the SC to the LL-leads, ν_S and ν_l the energy DOS per spin for the superconductor and the LL-leads at the chemical potentials μ_S and μ_l, resp., and δr the separation between the tunneling points on the SC. The current I_1 has a characteristic non-linear dependence on the voltage (electro-chemical potential μ), $I_1 \propto \mu^{2\gamma_\rho+1}$, with an interaction dependent exponent $\gamma_\rho = (K_\rho + K_\rho^{-1})/4 - 1/2 > 0$, which is the exponent for tunneling into the bulk of a single LL, i.e. $\rho(\varepsilon) \sim |\varepsilon|^{\gamma_\rho}$, where $\rho(\varepsilon)$ is the single-particle density of states (Schulz, 1990). In the non-interacting limit $\gamma_\rho = 0$ the current is given by I_1^0. As in Sec. V.A.1, the coherence length ξ of the Cooper pairs should exceed δr in order to obtain a finite measurable current. Note that the suppression of the current by $1/(k_F\delta r)^2$ can be considerably reduced with the use of lower dimensional SCs (Recher and Loss, 2002a,b). The *desired* current I_1 now has to be compared with *unwanted* current consisting of electron pairs tunneling into the same lead and having $\delta r = 0$. It is found (Recher and Loss, 2002a,b) that the current I_2 for tunneling into the same lead (1 or 2) is suppressed if $\mu < \Delta$ with the result, again in leading order in μ/Δ,

$$I_2 = I_1 \sum_{b=\pm 1} A_b \left(\frac{2\mu}{\Delta}\right)^{2\gamma_{\rho b}}, \tag{153}$$

where A_b is an interaction dependent constant of order one, and where $\gamma_{\rho+} = \gamma_\rho$, and $\gamma_{\rho-} = \gamma_{\rho+} + (1-K_\rho)/2 > \gamma_{\rho+}$. Note that in Eq. (153) the current I_1 needs to be evaluated at $\delta r = 0$. In the non-interacting limit, $I_2 = I_1 = I_1^0$ is obtained by putting $\gamma_\rho = \gamma_{\rho b} = 0$, and $u_\rho = v_F$. The expression Eq. (153) for I_2 shows that the unwanted injection of two electrons into the same lead is suppressed compared to I_1 by a factor of $(2\mu/\Delta)^{2\gamma_{\rho+}}$, where $\gamma_{\rho+} = \gamma_\rho$, if both electrons are injected into the *same* direction (left or right movers), or by $(2\mu/\Delta)^{2\gamma_{\rho-}}$ if the two electrons travel in *different* directions. It is more likely that the two electrons move in the same direction than in opposite directions, because $\gamma_{\rho-} > \gamma_{\rho+}$. The suppression of the current I_2 by $1/\Delta$ is a manifestation the two-particle correlations in the LL when the electrons tunnel into the same lead, which is similar to the Coulomb blockade effect in the case of tunneling into quantum dots in Sec. V.A.1. As the SC gap Δ becomes larger, the delay time between the arrivals of the two partner electrons of a Cooper pair becomes shorter, and the effect the first electron in the LL has on the second electron tunneling into the LL increases. Increasing the bias μ opens more available channels into which the electron can tunnel, and therefore the effect of the SC gap Δ is less pronounced. This correlation effect disappears when interactions in the LL are absent, $\gamma_\rho = \gamma_{\rho b} = 0$. Experimental systems with LL behavior are e.g. metallic carbon nanotubes with similar exponents as derived here (Egger and Gogolin, 1997; Kane *et al.*, 1997).

3. Transport through quantum dots

Entanglers with a single quantum dot attached to leads with a very narrow bandwidth (Oliver *et al.*, 2002) or with three coupled quantum dots (Saraga and Loss, 2003) have been proposed. The idea behind these proposals is the harness the singlet ground state of a single two-electron quantum dot by extracting the two electrons into two separate leads. In both proposals, the separation is enhanced due to two-particle energy conservation. A double-dot turnstile device with time-dependent barriers was proposed in (Hu and Das Sarma, 2004).

4. Coulomb scattering in a 2D electron system

Scanning probe techniques can be applied to a two-dimensional (2D) electron system formed in a semiconductor heterostructure in order to monitor and control the flow of electrons (Topinka *et al.*, 2000, 2001). It has been proposed to generate spin-entangled pairs of electrons using this technique to control Coulomb scattering in a interacting 2D electron system (Saraga *et al.*, 2004). At a scattering angle of $\pi/2$, it is expected that constructive two-particle interference leads to a enhancement of the spin-singlet scattering probability, while the triplet scattering is suppressed. The scattering amplitudes have been calculated within the Bethe-Salpeter equation for small r_s and allow an estimate of the achievable current of spin-entangled electrons (Saraga *et al.*, 2004).

5. Entangled Electrons in a Fermi Sea

A particularly appealing aspect of the electron spin as a carrier of quantum information is that it is attached to a charge, and thus it can—in principle—be transported in a conductor. One can therefore envision solid-state structures (e.g., on a microchip) where entanglement is produced in one location by one of the previously discussed methods, and subsequently conveyed through a wire to the location where entanglement is "used up" in some quantum information

protocol. While transporting qubits is quite unproblematic in the case of photons as the quantum information carriers (photons have been used in many experiments to carry quantum information, even over distances of kilometers), it is less trivial for electrons. When an electron is injected into a metallic wire, it is immersed into a sea of other electrons that (i) are indistinguishable from the injected electron, and (ii) constantly interact with all other electrons (including the injected one) via the Coulomb interaction. In this Section, the stability of spin entanglement in the Fermi sea will be discussed (Burkard *et al.*, 2000b; DiVincenzo and Loss, 1999). It turns out that (i) the indistinguishability of particles in the Fermi sea is actually not a problem for the transport of spin qubits and (ii) the Coulomb interaction does have some effect, which is however mitigated by the phenomenon of *screening* which is well-known in interacting Fermi liquids (Mahan, 1993). More precisely, when an electron in the orbital state q is added to a Fermi sea (lead), the quasiparticle weight of that state will be renormalized by $0 \leq z_q \leq 1$, i.e. some weight $1 - z_q$ to find the electron in the original state q will be distributed among all the other electrons. Such a rearrangement of the Fermi system due to the Coulomb interaction happens very quickly, on a time scale given by the inverse plasma frequency.

In order to analyze this effect quantitatively, the entangled two-electron state injected into two distinct leads 1 and 2 can be written in second quantized notation,

$$|\psi^{t/s}_{\mathbf{nn'}}\rangle = \frac{1}{\sqrt{2}} \left(a^\dagger_{\mathbf{n}\uparrow} a^\dagger_{\mathbf{n'}\downarrow} \pm a^\dagger_{\mathbf{n}\downarrow} a^\dagger_{\mathbf{n'}\uparrow}\right) |\psi_0\rangle, \tag{154}$$

where s and t stand for the singlet and triplet, $|\psi_0\rangle$ for the filled Fermi sea, and $\mathbf{n} = (\mathbf{q}, l)$, where $\mathbf{q}$ denotes the momentum and l the lead quantum number of an electron. As usual, the operator $a^\dagger_{\mathbf{n}\sigma}$ creates an electron in state $\mathbf{n}$ with spin σ. After their injection, the two electrons of interest are no longer distinguishable from the electrons of the leads, and consequently the two electrons taken out of the leads will, in general, not be the same as the ones injected.

The time evolution of the triplet or singlet states, interacting with all other electrons in the Fermi sea, is described by the 2-particle Green's function $G^{t/s}(\mathbf{12}, \mathbf{34}; t) = \langle \psi^{t/s}_{\mathbf{12}}, t | \psi^{t/s}_{\mathbf{34}} \rangle$, which is related to the standard 2-particle Green's function $G(12, 34; t)$ by

$$G^{t/s}(\mathbf{12}, \mathbf{34}; t) = -\frac{1}{2} \sum_\sigma [G(1\bar{2}, 3\bar{4}; t) \pm G(1\bar{2}, \bar{3}4; t)] \,, \tag{155}$$

where $n = (\mathbf{n}, \sigma)$ and $\bar{n} = (\mathbf{n}, -\sigma)$. Assuming that at time $t = 0$, a triplet (singlet) is prepared, then the *fidelity of transmission*

$$P(t) = |G^{t/s}(\mathbf{12}, \mathbf{12}; t)|^2 \tag{156}$$

is defined as the probability for finding a triplet (singlet) after time t.

With Eq. (155), the problem reduces to that of evaluating the standard two-particle Green's function $G(12, 34; t) = -\langle T a_1(t) a_2(t) a^\dagger_3 a^\dagger_4 \rangle$ for a time- and spin-independent Hamiltonian, $H = H_0 + \sum_{i<j} V_{ij}$, where H_0 describes the free motion of the N electrons, and V_{ij} is the bare Coulomb interaction between electrons i and j, $\langle ... \rangle$ denotes the zero-temperature expectation value, and T is the time ordering operator. One can assume that the leads are sufficiently separated, so that the mutual Coulomb interaction can be neglected, and thus the problem of finding an explicit value for $G(12, 34; t)$ is simplified since the 2-particle vertex part vanishes (i.e. the Hartree-Fock approximation is exact),

$$G(12, 34; t) = G(13, t) G(24, t) - G(14, t) G(23, t), \tag{157}$$

with the interacting single-particle Green's functions

$$G(\mathbf{n}, t) = -i \langle \psi_0 | T a_{\mathbf{n}}(t) a^\dagger_{\mathbf{n}} | \psi_0 \rangle \equiv G_l(\mathbf{q}, t), \tag{158}$$

for each lead $l = 1, 2$. Substituting this back into Eq. (155), one obtains

$$G^{t/s}(\mathbf{12}, \mathbf{34}; t) = -G(\mathbf{1}, t)\, G(\mathbf{2}, t) [\delta_{\mathbf{13}} \delta_{\mathbf{24}} \mp \delta_{\mathbf{14}} \delta_{\mathbf{23}}], \tag{159}$$

where the upper (lower) sign refers to the spin triplet (singlet). For the initial state ($t = 0$), or in the absence of interactions, one finds $G(\mathbf{n}, t) = -i$, and thus $G^{t/s}$ reduces to $\delta_{\mathbf{13}} \delta_{\mathbf{24}} \mp \delta_{\mathbf{14}} \delta_{\mathbf{23}}$, and $P = 1$. The evaluation of the (time-ordered) single-particle Green's functions $G_{1,2}$ close to the Fermi surface yields the standard result (Mahan, 1993) $G_{1,2}(\mathbf{q}, t) \approx -i z_q \theta(\epsilon_q - \epsilon_F) e^{-i\epsilon_q t - \Gamma_q t}$, which holds for $0 \leq t \lesssim 1/\Gamma_q$, where $1/\Gamma_q$ is the quasiparticle lifetime, $\epsilon_q = q^2/2m$ the quasiparticle energy (of the added electron), and ϵ_F the Fermi energy. For a two-dimensional electron system (2DES), as e.g. in GaAs heterostructures, $\Gamma_q \propto (\epsilon_q - \epsilon_F)^2 \log(\epsilon_q - \epsilon_F)$ (Giuliani and Quinn, 1982) within the random phase approximation (RPA), which accounts for screening and which is obtained by summing all polarization diagrams (Mahan, 1993). The quantity of interest here is the quasiparticle weight, $z_F = (1 - \frac{\partial}{\partial \omega} \mathrm{Re}\, \Sigma_{\mathrm{ret}}(k_F, \omega))^{-1}\big|_{\omega=0}$,

evaluated at the Fermi surface, where $\Sigma_{\rm ret}(q,\omega)$ is the retarded irreducible self-energy. For momenta $\mathbf{q}$ close to the Fermi surface and for identical leads ($G_1 = G_2$) we find $|G^{t/s}(\mathbf{12},\mathbf{34};t)|^2 = z_F^4\,|\,\delta_{\mathbf{13}}\delta_{\mathbf{24}} \mp \delta_{\mathbf{14}}\delta_{\mathbf{23}}|^2$, for times satisfying $0 < t \lesssim 1/\Gamma_q$. The fidelity therefore turns out to be

$$P = z_F^4 \tag{160}$$

.

The irreducible self-energy $\Sigma_{\rm ret}$ and from it the quasiparticle weight factor in two dimensions were evaluated explicitly (Burkard *et al.*, 2000b), with the final result

$$z_F = \frac{1}{1 + r_s\,(1/2 + 1/\pi)}, \tag{161}$$

in leading order of the interaction parameter $r_s = 1/k_F a_B$, where $a_B = \epsilon_0\hbar^2/me^2$ is the Bohr radius. In particular, in a GaAs 2DES we have $a_B = 10.3$ nm, and $r_s = 0.614$, and thus we obtain $z_F = 0.665$. The expansion in powers of r_s for the exact RPA self-energy can be summed up and evaluated numerically, with the (more accurate) result $z_F = 0.691155$ for GaAs. The fidelity of transmission of the injected singlet in this case is around $P \approx 0.2$. However, for large electron density (small r_s), P is closer to unity. Note the fidelity of the ("postselected") singlet pairs which can successfully be removed from the Fermi sea, is equal to 1, provided that (as assumed here) the spin-scattering effects are negligible. That this is indeed the case in GaAs 2DEGs is supported by experiments where the electron spin has been transported phase-coherently over distances of up to $100\,\mu$m (Awschalom and Kikkawa, 1999; Kikkawa and Awschalom, 1998; Kikkawa *et al.*, 1997).

B. Detection of spin entanglement

Efforts are being made to produce spin entanglement in solid-state structures; therefore, it is only natural to ask how one can *test* for the presence of entanglement in such a setting. Here, a variety of tests for spin entanglement are described. This investigation touches on fundamental issues such as the non-locality of quantum mechanics, especially for massive particles, and genuine two-particle Aharonov-Bohm effects which are fascinating topics in their own right. The main idea in all of the following detection schemes is to exploit the unique relation between the symmetry of the orbital state and the two-electron spin state which makes it possible to detect an electron spin state via the orbital (charge) degrees of freedom.

1. Coupled quantum dots

The first setup to be considered can be used to probe the entanglement of two electrons localized in a double-dot by measuring a transport current and its fluctuations, or current noise (Loss and Sukhorukov, 2000). It is assumed that the double-dot is weakly coupled to in- and outgoing leads (at chemical potentials $\mu_{1,\,2}$) with tunneling amplitude $\mathcal{T}$, where the dots are shunted in parallel. The regime of interest is (i) the Coulomb blockade regime (Kouwenhoven *et al.*, 1997c) where the charge on the dots is quantized and (ii) the cotunneling regime (Averin and Nazarov, 1992; König *et al.*, 1997), where single-electron tunneling is forbidden by energy conservation. The latter regime is defined by $U > |\mu_1 \pm \mu_2| > J > k_BT, 2\pi\nu\mathcal{T}^2$ where U is the single-dot charging energy, ν the lead density of states, and J the exchange coupling between the dots. The current in the cotunneling regime is generated by a coherent virtual process where one electron tunnels from a dot to, say, lead 2 and then a second electron tunnels from lead 1 to this dot. If the bias voltage is larger than the exchange coupling, $|\mu_1 - \mu_2| > J$, elastic as well as inelastic cotunneling will occur. It will be assumed that $\mathcal{T}$ is small enough for the double-dot to return to its equilibrium state after each tunneling event. An electron can either pass through the upper or lower dot, therefore a closed loop is formed by these two paths. A magnetic flux then gives rise to an Aharonov-Bohm phase $\phi = ABe/\hbar$ (A being the loop area) between the upper and the lower paths leading to quantum interference effects. This transport setting is sensitive to the spin symmetry of the two-electron state on the double dot; if the two electrons on the double-dot are in the *singlet state*, then the tunneling current acquires an additional phase of π leading to a sign reversal of the coherent contribution compared to that for triplets. In cotunneling current, this additional phase manifests itself in the sign of an interference term (Loss and Sukhorukov, 2000)

$$I = e\pi\nu^2\mathcal{T}^4\,\frac{\mu_1 - \mu_2}{\mu_1\mu_2}\,(2 \pm \cos\phi)\,, \tag{162}$$

where the upper sign refers to the triplet states in the double-dot and the lower sign to the singlet state. The shot noise is Poissonian with power $S(0) = -e|I|$, hence it has the same dependence on the state on the double dot.

The shot noise has also been calculated for finite frequencies in (Loss and Sukhorukov, 2000), and it was found that again $S(\omega) \propto (2 \pm \cos\phi)$, and that the odd part of $S(\omega)$ leads to slowly decaying oscillations of the noise in real time, $S(t) \propto \sin(\mu t)/\mu t$, $\mu = (\mu_1 + \mu_2)/2$, which can be ascribed to a charge imbalance on the double dot during an uncertainty time μ^{-1}.

Note that while the scheme described above is able to distinguish the states $|S\rangle$ and $|T_0\rangle$ on the dots, the three triplets $|T_0\rangle$, $|T_+\rangle$, and $|T_-\rangle$, can be further distinguished by an orientationally inhomogeneous magnetic field which results in a spin-Berry phase (Loss and Goldbart, 1992; Loss and Sukhorukov, 2000) that leads to left, right or no phase-shift in the Aharonov-Bohm oscillations of the current (noise).

2. Coupled dots with SC leads

A related scenario of double-dots (DD) has been considered in (Choi *et al.*, 2000), where two quantum dots are again shunted in parallel between the leads, but without any direct coupling between them. The two dots are assumed to be coupled via tunneling (with amplitude $\mathcal{T}$) to two superconducting leads. It turns out that the s-wave SC energetically favors an entangled singlet-state on the dots. In addition to this, the coupling to the SC provides a mechanism for detecting the spin state via the Josephson current through the double dot system. In leading order $\propto \mathcal{T}^4$, the spin coupling is described by a Heisenberg Hamiltonian (Choi *et al.*, 2000)

$$H_{\rm eff} \approx J\,(1+\cos\varphi)\,\left(\mathbf{S}_a \cdot \mathbf{S}_b - \frac{1}{4}\right), \tag{163}$$

where $J \approx 2\mathcal{T}^2/\epsilon$, ϵ is the energy difference from the dot state to the Fermi level, and φ is the average phase difference across the SC-DD-SC junction. The exchange coupling between the spins can be controlled by tuning the external parameters $\mathcal{T}$ and φ, thus providing another implementation of a two-qubit quantum gate (Sec. I.A.4) or entangler (Sec. V.A). The spin state (singlet or triplet) on the dot can be probed if the SC leads are joined with one additional (ordinary) Josephson junction with coupling J' and phase difference θ into a SQUID. The SC current I_S flowing in this ring is given by (Choi *et al.*, 2000)

$$I_S/I_J = \begin{cases} \sin(\theta - 2\pi f) + (J'/J)\sin\theta\,, & \text{singlet,} \\ (J'/J)\sin\theta\,, & \text{triplets,} \end{cases} \tag{164}$$

where $I_J = 2eJ/\hbar$. The spin state of the DD is now probed by measuring the spin- and flux-dependent critical current $I_c = \max_\theta\{|I_S|\}$ by biasing the system with a dc current I until a finite voltage V appears for $|I| > I_c$ (the SC goes into the normal state). Another interesting effect is long-distance coupling between spins residing in dots separated by δr which is induced by the presence of the SC. The resulting exchange coupling is

$$J(\delta r) = J(0)\left[\frac{\sin(k_F\delta r)}{k_F\delta r}\right]^2 e^{-2\delta r/\xi}. \tag{165}$$

3. Beam splitter shot noise

Pairwise spin entanglement between electrons in two mesoscopic wires can be detected from a charge current measurement after transmission through an electronic beam splitter (Burkard *et al.*, 2000b). In this scheme, the singlet EPR pair Eq. (149) gives rise to an enhancement of the shot noise power ("bunching" behavior), whereas the triplet EPR pair $|T_0\rangle$ leads to a suppression of noise ("antibunching"). This behavior can be anticipated from a textbook example: the scattering theory of two identical particles in vacuum (Ballentine, 1990; Feynman *et al.*, 1965). There, the differential scattering cross-section σ in the center-of-mass frame can be expressed in terms of the scattering amplitude $f(\theta)$ and scattering angle θ as

$$\sigma(\theta) = |f(\theta) \pm f(\pi-\theta)|^2 = |f(\theta)|^2 + |f(\pi-\theta)|^2 \pm 2Re f^*(\theta) f(\pi-\theta), \tag{166}$$

the first two terms on the right being the contributions which would be obtained if the particles were distinguishable, and the third (exchange) term the contribution due to the particles' indistinguishability. This last term gives rise to genuine two-particle interference effects. Here, the plus (minus) sign applies to spin-1/2 particles in the singlet (triplet) state, described by a (anti)symmetric orbital wave function. The very same two-particle interference mechanism which is responsible for the enhancement (reduction) of the scattering cross section $\sigma(\theta)$ near $\theta = \pi/2$ also leads to an increase (decrease) of the correlations of the particle number in the output arms of a beam splitter (Loudon, 1998).

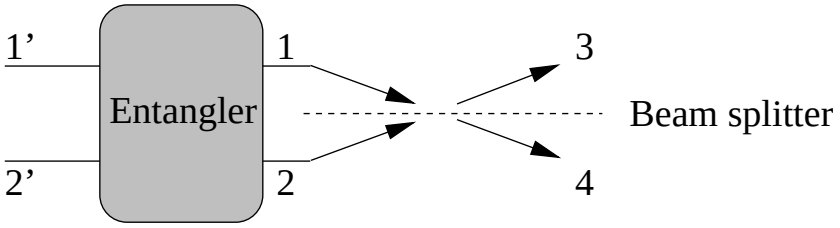


FIG. 31 Setup for measuring the noise of entangled states. Uncorrelated electrons are fed into the entangler (see text) through the Fermi leads $1'$, $2'$ and are transformed into pairs of electrons in the entangled singlet (triplet) state $|\mp\rangle$, which are injected into leads 1, 2 (one electron of undetermined spin state into each lead). The entanglement of the, say, spin singlet can then be detected in an interference experiment using a beam splitter (with no backscattering): Since the orbital wave function of the singlet is symmetric, the electrons leave the scattering region preferably in the same lead (3 or 4). This correlation ("bunching") is revealed by an enhancement of the noise by a factor of 2 in the outgoing leads.

For the detection of spin entanglement of electrons carried by two mesoscopic wires, we propose a non-equilibrium transport measurement based on the set-up shown in Fig. 31. The beam splitter ensures that the electrons leaving the entangler (see Sec. V.A) have an amplitude t to be interchanged (without mutual interaction) such that $0 < |t|^2 < 1$. In the absence of spin scattering the noise measured in the outgoing leads 3 and 4 exhibits bunching behavior for pairs of electrons with a symmetric orbital wave function (Hanbury Brown and Twiss, 1956), i.e., for spin singlets, while spin triplets induce antibunching behavior, due to their antisymmetric orbital wave function. The latter situation has been considered for electrons in the normal state both in theory (Büttiker, 1990, 1992; Martin and Landauer, 1992) and in recent experiments (Henny *et al.*, 1999; Liu *et al.*, 1998; Oliver *et al.*, 1999; Torrès and Martin, 1999). The experiments have been performed in semiconductor nanostructures with geometries that are closely related to the set-up proposed in Fig. 31 but without entangler. It should be stressed here that if bunching (enhancement of shot noise) is detected, it can be interpreted as a unique signature for entanglement of the injected electrons, since the maximally entangled singlet is the only state leading to this effect. The effect of interactions in the leads have already been assessed in Sec. V.A.5. In order to determine the shot noise of spin-entangled electrons, the standard scattering matrix approach (Büttiker, 1990, 1992), extended to a situation with entanglement, is applied.

We start by writing down the entangled incident state $|\pm\rangle \equiv |\psi^{t/s}_{\mathbf{12}}\rangle$, where we set $\mathbf{n} = (\varepsilon_n, n)$, now using the electron energies ε_n instead of the momentum as the orbital quantum number in Eq. (154) and where the operator $a^\dagger_{\alpha\sigma}(\varepsilon)$ creates an incoming electron in lead α with spin σ and energy ε. The theory for the current correlations in a multiterminal conductor (Büttiker, 1990, 1992) can easily be generalized to the case of entangled scattering states, with the important consequence that Wick's theorem does not apply. The operator for the current carried by electrons in lead α of a multiterminal conductor can be written as

$$I_\alpha(t) = \frac{e}{h\nu} \sum_{\varepsilon\varepsilon'\sigma} \left[a^\dagger_{\alpha\sigma}(\varepsilon) a_{\alpha\sigma}(\varepsilon') - b^\dagger_{\alpha\sigma}(\varepsilon) b_{\alpha\sigma}(\varepsilon')\right] \exp\left[i(\varepsilon - \varepsilon')t/\hbar\right], \tag{167}$$

where the operators $b_{\alpha\sigma}(\varepsilon)$ for the outgoing electrons are related to the operators $a_{\alpha\sigma}(\varepsilon)$ for the incident electrons via $b_{\alpha\sigma}(\varepsilon) = \sum_\beta s_{\alpha\beta} a_{\beta\sigma}(\varepsilon)$, where $s_{\alpha\beta}$ denotes the scattering matrix. The scattering matrix is assumed to be spin- and energy-independent. Note that for a discrete energy spectrum in the leads, one can normalize the operators $a_{\alpha\sigma}(\varepsilon)$ such that $\{a_{\alpha\sigma}(\varepsilon), a^\dagger_{\beta\sigma'}(\varepsilon')\} = \delta_{\sigma\sigma'}\delta_{\alpha\beta}\delta_{\varepsilon\varepsilon'}/\nu$, where the Kronecker symbol $\delta_{\varepsilon\varepsilon'}$ equals 1 if $\varepsilon = \varepsilon'$ and 0 otherwise. Here, ν stands for the density of states in the leads. Each lead is assumed to consist of only a single quantum channel; the generalization to leads with several channels is straightforward but not required here. The current Eq. (167) can be expressed in terms of the scattering matrix as

$$I_\alpha(t) = \frac{e}{h\nu} \sum_{\varepsilon\varepsilon'\sigma} \sum_{\beta\gamma} a^\dagger_{\beta\sigma}(\varepsilon) A^\alpha_{\beta\gamma} a_{\gamma\sigma}(\varepsilon') e^{i(\varepsilon-\varepsilon')t/\hbar}, \tag{168}$$

$$A^\alpha_{\beta\gamma} = \delta_{\alpha\beta}\delta_{\alpha\gamma} - s^*_{\alpha\beta} s_{\alpha\gamma}. \tag{169}$$

The correlation function between the currents $I_\alpha(t)$ and $I_\beta(t)$ in two leads $\alpha, \beta = 1, .., 4$ of the BS

$$S^\chi_{\alpha\beta}(\omega) = \lim_{\tau\to\infty} \frac{h\nu}{\tau} \int_0^\tau dt\; e^{i\omega t}\, \mathrm{Re}\,\mathrm{Tr}\left[\delta I_\alpha(t)\delta I_\beta(0)\chi\right], \tag{170}$$

where $\delta I_\alpha = I_\alpha - \langle I_\alpha\rangle$, $\langle I_\alpha\rangle = \mathrm{Tr}(I_\alpha\chi)$, ν is the density of states in the leads, and χ is the density matrix of the injected electron pair. Here, only the zero-frequency correlator $S_{\alpha\beta} \equiv S^\chi_{\alpha\beta}(0)$ will be of interest (the dependence on

χ was omitted). Further evaluation with $\chi = |\pm\rangle\langle\pm|$ yields

$$S_{\alpha\beta} = \frac{e^2}{h\nu}\Big[\sum_{\gamma\delta}{}' A^\alpha_{\gamma\delta}A^\beta_{\delta\gamma} \mp \delta_{\varepsilon_1,\varepsilon_2}\big(A^\alpha_{12}A^\beta_{21}+A^\alpha_{21}A^\beta_{12}\big)\Big], \tag{171}$$

where $\sum'_{\gamma\delta}$ denotes the sum over $\gamma = 1, 2$ and all $\delta \neq \gamma$, and where again the upper (lower) sign refers to triplets (singlets). Note that the autocorrelator $S_{\alpha\alpha}$ is the shot noise in lead α.

The result Eq. (171) can now be applied to the set-up shown in Fig. 31 involving four leads, described by the single-particle scattering matrix elements, $s_{31} = s_{42} = r$, and $s_{41} = s_{32} = t$, where r and t denote the reflection and transmission amplitudes at the beam splitter. In the absence of backscattering, $s_{12} = s_{34} = s_{\alpha\alpha} = 0$, the noise correlations for the incident state $|\pm\rangle$ are

$$S_{33} = S_{44} = -S_{34} = 2\frac{e^2}{h\nu}T\,(1-T)\,(1 \mp \delta_{\varepsilon_1\varepsilon_2})\,, \tag{172}$$

where $T = |t|^2$ denotes the transmittivity of the beam splitter. For the remaining two triplet states $|\uparrow\uparrow\rangle$ and $|\downarrow\downarrow\rangle$ one also obtains Eq. (172) with the upper sign. The mean current in lead α is, both for singlets and triplets, $|\langle I_\alpha\rangle| = e/h\nu$. The noise-to-current ratio, or Fano factor, $F = S_{\alpha\alpha}/\,|\langle I_\alpha\rangle|$ is thus found to be

$$F = 2eT(1-T)\,(1 \mp \delta_{\varepsilon_1\varepsilon_2})\,, \tag{173}$$

and correspondingly for the cross correlations. Eq. (173) implies that if electrons in the singlet state $|-\rangle$ with equal energies, $\varepsilon_1 = \varepsilon_2$, are injected pairwise into the leads 1 and 2, then the zero frequency noise is *enhanced* by a factor of two, $F = 4eT(1-T)$, compared to the shot noise of uncorrelated particles (Büttiker, 1990, 1992; Khlus, 1987; Landauer, 1989; Lesovik, 1989; Martin and Landauer, 1992), $F = 2eT(1-T)$. This noise enhancement is due to *bunching* of electrons in the outgoing leads, caused by the symmetric orbital wavefunction of the spin singlet $|-\rangle$. The triplet states $|+\rangle$, $|\uparrow\uparrow\rangle$, and $|\downarrow\downarrow\rangle$ exhibit *antibunching*, i.e. a complete suppression of the noise, $S_{\alpha\alpha} = 0$. As already mentioned above, the noise enhancement for the singlet $|-\rangle$ is a unique signature for entanglement (no unentangled state exists which can lead to this phenomenon), therefore entanglement can be observed by measuring the noise power of a mesoscopic conductor as shown in Fig. 31. The various triplet states $|+\rangle$, $|\uparrow\uparrow\rangle$, and $|\downarrow\downarrow\rangle$ cannot be distinguished by the noise measurement alone; this distinction requires a measurement of the spins of the outgoing electrons, e.g. by inserting spin-selective tunneling devices (Prinz, 1998) into leads 3 and 4. The same signature of entanglement as for the shot noise can also be seen in the full counting statistics of the charge transport (Taddei and Fazio, 2002).

4. Lower bounds for entanglement

Here, the result of the previous Section is extended by providing a quantitative *lower bound* for the *amount* E of spin entanglement carried by individual pairs of electrons, related to the zero-frequency current correlators when measured in a beam splitter setup (Fig. 32). This result (Burkard and Loss, 2003) therefore relates experimentally accessible quantities with a measure for entanglement, the entanglement of formation E (Bennett *et al.*, 1996b). Having information about E is important since it quantifies the usefulness of a bipartite state for quantum communication.

Starting form a general state, expressed in the singlet-triplet basis as $\chi = F|-\rangle\langle -| + G_0|+\rangle\langle +| + \sum_{i=\uparrow,\downarrow} G_i|ii\rangle\langle ii| + \Delta\chi$, where $\Delta\chi$ are off-diagonal terms, one can decompose the current correlators Eq. (170) as

$$S_{\alpha\beta} \equiv S^\chi_{\alpha\beta} = FS^{|\Psi_-\rangle}_{\alpha\beta} + G_0 S^{|\Psi_+\rangle}_{\alpha\beta} + \sum_{i=\uparrow,\downarrow} G_i S^{|ii\rangle}_{\alpha\beta}, \tag{174}$$

where $S^{|\Psi\rangle}_{\alpha\beta} \equiv S^{|\Psi\rangle\langle\Psi|}_{\alpha\beta}$. The off-diagonal terms in $\Delta\chi$ do not enter $S_{\alpha\beta}$ because the operators $\delta I_\alpha(t)$ conserve total spin. The coefficients F, G_0, $G_\uparrow$, and $G_\downarrow$ depend on the state preparation and therefore on the entangler. The more information about these coefficients can be gained, the better the chance to measure the entanglement of χ. In Sec. V.B.3 it was shown that the singlet state $|-\rangle$ gives rise to enhanced shot noise (and cross-correlators) at zero temperature, $S^{|-\rangle}_{33} = -S^{|-\rangle}_{34} = 2eIT(1-T)f$, with the *reduced correlator* $f = 2$, as compared to the "classical" Poissonian value $f = 1$. All triplet states are noiseless, $S^{|+\rangle}_{\alpha\beta} = S^{|\uparrow\uparrow\rangle}_{\alpha\beta} = S^{|\downarrow\downarrow\rangle}_{\alpha\beta} = 0$ $(\alpha, \beta = 3, 4)$. Therefore, both the auto- and cross-correlations are only due to the singlet component of the incident two-particle state,

$$S_{33} = -S_{34} = FS^{|\Psi_-\rangle} = 2eIT(1-T)f, \qquad f = 2F. \tag{175}$$

The entanglement of a bipartite *pure* state $|\psi\rangle \in \mathcal{H}_A \otimes \mathcal{H}_B$ can be measured by the von Neumann entropy $S_{\rm N}(|\psi\rangle) = -{\rm Tr}_B \rho_B \log \rho_B$ (log in base 2) of the reduced density matrix $\rho_B = {\rm Tr}_A|\psi\rangle\langle\psi|$, where $0 \leq S_{\rm N} \leq 1$, $S_{\rm N}(|\Psi_\pm\rangle) =$

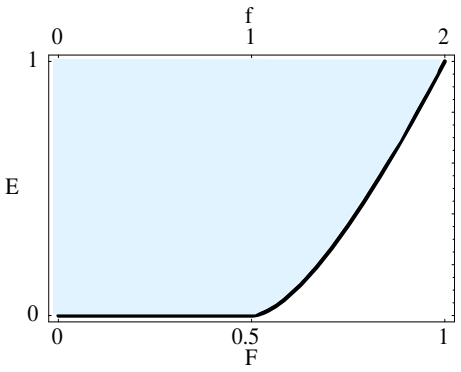


FIG. 32 Entanglement of formation E of the electron spins versus singlet fidelity F and the reduced correlator $f = S_{33}/2eIT(1-T)$. The curve illustrates the exact relation for Werner states. For general states, the curve is a lower bound for E; allowed values for E and f (or F) are in the shaded region.

$S_{\rm N}(|\Phi_\pm\rangle) = 1$, and $S_{\rm N}(|\psi\rangle) = 0 \Leftrightarrow |\psi\rangle = |\psi\rangle_A \otimes |\psi\rangle_B$. Physically, if $S_{\rm N}(|\psi\rangle) \simeq N/M$ then $M \geq N$ copies of $|\psi\rangle$ are sufficient to perform, e.g., quantum teleportation of N qubits for $N, M \gg 1$ (similarly for other quantum communication protocols). Generally, for a bipartite *mixed* state χ the entanglement of formation (Bennett *et al.*, 1996b) is $E(\chi) = \min_{\{(|\chi_i\rangle, p_i)\} \in \mathcal{E}(\chi)} \sum_i p_i S_{\rm N}(|\chi_i\rangle)$, where $\mathcal{E}(\chi) = \{(|\chi_i\rangle, p_i) | \sum_i p_i |\chi_i\rangle\langle\chi_i| = \chi\}$, i.e., the least expected entanglement of any ensemble of pure states realizing χ. A state with $E > 0$ ($E = 1$) is (maximally) entangled, and neither local operations nor classical communication (LOCC) between A and B can increase E.

For an arbitrary mixed state of two qubits χ, $E(\chi)$ is not a function of only the singlet fidelity $F = \langle -|\chi|-\rangle$. However, $E(\chi) = E(F)$ for the Werner states (Werner, 1989)

$$\rho_F = F|-\rangle\langle -| + \frac{1-F}{3}\left(|+\rangle\langle +| + \sum_{i=\pm} |\Phi_i\rangle\langle\Phi_i|\right), \tag{176}$$

the unique rotationally invariant states with singlet fidelity F, where $|\Phi_\pm\rangle = (|\uparrow\uparrow\rangle \pm |\downarrow\downarrow\rangle)/\sqrt{2}$. The entanglement of formation of the Werner states is known (Bennett *et al.*, 1996b) as $E(F) \equiv E(\rho_F) = H_2(1/2 + \sqrt{F(1-F)})$ if $1/2 < F \leq 1$ and $E(F) \equiv E(\rho_F) = 0$ if $0 \leq F < 1/2$, with the dyadic Shannon entropy $H_2(x) = -x\log x - (1-x)\log(1-x)$. With Eq. (175), one can now express $E(\rho_F)$ in terms of the reduced correlator f (Fig. 32).

This result can be generalized to arbitrary mixed states χ of two spins (qubits) using the following trick. Any state χ can be transformed into ρ_F with $F = \langle\Psi_-|\chi|\Psi_-\rangle$ by a random bipartite rotation ("twirl") (Bennett *et al.*, 1996a,b), i.e. by applying $U \otimes U$ with a random $U \in SU(2)$. Entanglement can only decrease (or remain constant) under the twirl operation because it involves only LOCC,

$$E(F) \leq E(\chi). \tag{177}$$

Thus, the entanglement of formation $E(F)$ of the corresponding Werner state represents a *lower bound* on $E(\chi)$ (Fig. 32). A noise power exceeding $f = 2F > 1$ in the BS setup Fig. 31 can therefore be interpreted as a sign of entanglement, $E(F) > 0$, between the electron spins injected into leads 1 and 2.

The lower bounds that have been discussed so far are only useful if one is assessing a source that aims at producing spin spinglet entanglement. However, it is possible in principle to extend this result to arbitrary entangled states if a means of rotating the spin of the carriers in one of the ingoing arms of the BS is available; such spin rotators could, e.g., be implemented by making use of the Rashba spin orbit effect (Egues *et al.*, 2002).

The relation between the shot noise f and the entanglement E has also been explored in a number of non-ideal situations, in the presence of decoherence, backscattering, and thermally mixed input states (Burkard and Loss, 2003).

5. Proposed tests of Bell's inequalities

There have been a number of proposals to test Bell's inequalities (Bell, 1966; Mermin, 1993) with *spin*-entangled electrons directly with a spin-sensitive detection scheme (Kawabata, 2001; Lesovik *et al.*, 2001; Maître *et al.*, 2000) in contrast to the detection scheme in Secs. V.B.3 and V.B.4 which only involves the measurement of a charge current. Combinations of the Andreev entangler setup with a Bell test were studied in (Chtchelkatchev *et al.*, 2002; Samuelsson *et al.*, 2004a).

Bell tests for *orbital* entanglement with electron charge qubits in ballistic conductors have also been proposed (Ionicioiu *et al.*, 2001). A scheme to generate two-particle orbital entanglement in a mesoscopic normal-superconductor

system and to detect it via a violation of a Bell inequality was analyzed in (Samuelsson *et al.*, 2003). A violation of a Bell inequality due to orbital entanglement in a Hanbury Brown–Twiss setting was also proposed (Samuelsson *et al.*, 2004b).

C. Production of entangled photons

The use of entangled photons from parametric down-conversion in non-linear crystals (Kwiat *et al.*, 1995, 1999) has become a routine process (Boschi *et al.*, 1998; Bouwmeester *et al.*, 1997; Mattle *et al.*, 1996). However, two disadvantages of these sources are (i) that they are quite inefficient (between 10^6 and 10^{10} pump photons per yield photon) and (ii) that they are stochastic, i.e., although the rate (mean number of entangled pairs per second) is known, the precise instant of the emission cannot be controlled. It would be desirable to have a source of entangled photons that is both *deterministic* and *efficient*. The use of electron-hole recombination in a single QD was suggested in (Benson *et al.*, 2000; Moreau *et al.*, 2001). Non-resonant excitation of a QD is expected to produce pairs of entangled photons with an efficiency (production rate/pump rate) that is about four orders of magnitude bigger than for parametric down-conversion (Moreau *et al.*, 2001). Ultraviolet entangled photons have recently been generated in the semiconductor CuCl in a process called resonant hyper-parametric scattering (RHPS) which involves the creation of a virtual biexciton state in the crystal (Edamatsu *et al.*, 2004). Although this is still a stochastic source, RHPS is a very efficient process.

The production of polarization-entangled photons using the biexcitonic ground state has been investigated in *two tunnel-coupled* QDs (Gywat *et al.*, 2002). Biexcitons are bound states of two excitons in a semiconductor, where each exciton is the bound state of a negatively charged conduction-band electron and a positively charged valence-band hole. Excitonic absorption in single QDs has been studied theoretically (Efros and Efros, 1982), and biexcitonic states in single QDs have been investigated (Banyai *et al.*, 1988; Bryant, 1990; Hawrylak, 1999; Hu *et al.*, 1990; Kiraz *et al.*, 2002; Nair and Takagahara, 1996; Santori *et al.*, 2002; Takagahara, 1989). Single excitons in coupled QDs have been observed in experiment (Bayer *et al.*, 2001; Schedelbeck *et al.*, 1997) and spin spectroscopy of excitons in QDs was performed using polarization-resolved magnetophotoluminenscence (Johnston-Halperin *et al.*, 2001). When discussing confined excitons, one needs to distinguish two regimes (Efros and Efros, 1982): (i) The *weak confinement* limit $a_X \ll a_e, a_h$, where a_X is the radius of the free exciton and a_e, a_h the electron and hole effective Bohr radii in the QD. In this regime, an exciton can be considered (as in the bulk material) as a boson in an external confinement potential. (ii) The *strong confinement* limit $a_X \gg a_e, a_h$, where electrons and holes are separately confined in the QD. In this regime, electron-hole pairs cannot be considered as bosons anymore. In bulk GaAs $a_X \approx 10$ nm, one is often in an intermediate regime $a_X \approx a_e, a_h$ for typical QD radii.

Starting from a strong confinement ansatz and using the Heitler-London (HL) approximation, the low-energy (spin-resolved) biexciton spectrum (in which the electrons and holes each form either a spin singlet or triplet) and the oscillator strengths Fig. 33, being a measure for the optical transition rates, have been calculated (Gywat *et al.*, 2002). The HL ansatz is similar to the one used for electrons in Sec. III.B.1 with the Hamiltonian

$$H = \sum_{\alpha=e,h} \sum_{i=1}^{2} h_{\alpha i} + H_C + H_Z + H_E, \tag{178}$$

where $h_{\alpha i} = (\mathbf{p}_{\alpha i} + q_\alpha \mathbf{A}(\mathbf{r}_{\alpha i})/c)^2/2m_\alpha + V_\alpha(\mathbf{r}_{\alpha i})$ is the single-particle Hamiltonian for the i-th electron ($\alpha = e$, $q_e = -e$) or hole ($\alpha = h$, $q_h = +e$). The Coulomb interaction is included by $H_C = (1/2)\sum_{(\alpha,i)\neq(\beta,j)} q_\alpha q_\beta/\kappa|\mathbf{r}_{\alpha i} - \mathbf{r}_{\beta j}|$, with a dielectric constant κ (for bulk GaAs, $\kappa = 13.18$). A magnetic field $\mathbf{B}$ in z direction leads to orbital effects via the vector potential (in the symmetric gauge) $\mathbf{A} = B(-y, x, 0)/2$ and to the Zeeman term $H_Z = \sum_{\alpha,i} g_\alpha \mu_B B S_z^{\alpha i}$, where g_α is the effective g-factor of the electron (hole) and μ_B is the Bohr magneton.

Two-particle wave functions for electrons and for holes separately are constructed according to the HL method, i.e. a symmetric ($|s\rangle^\alpha \equiv |I=0\rangle^\alpha$, spin singlet) and an antisymmetric ($|t\rangle^\alpha \equiv |I=1\rangle^\alpha$, spin triplet) linear combination of two-particle states $|DD'\rangle_\alpha = |D\rangle_\alpha \otimes |D'\rangle_\alpha$,

$$|I\rangle^\alpha = N_{\alpha I}(|12\rangle_\alpha + (-1)^I |21\rangle_\alpha), \tag{179}$$

where $N_{\alpha I} = 1/\sqrt{2(1+(-1)^I|S_\alpha|^2)}$ and $S_\alpha = {}_\alpha\langle 1|2\rangle_\alpha$ denotes the overlap between the two orbital wave functions $|1\rangle_\alpha$ and $|2\rangle_\alpha$. From the electron and hole singlet and triplet, the four biexciton states $|IJ\rangle = |I\rangle^e \otimes |J\rangle^h$ can be formed, where $I = 0$ (1) for the electron singlet (triplet) and $J = 0$ (1) for the hole singlet (triplet). The biexciton energies

$$E_{IJ} = \langle IJ|H|IJ\rangle = E^0 + E^Z + E^W_{IJ} + E^C_{IJ}, \tag{180}$$

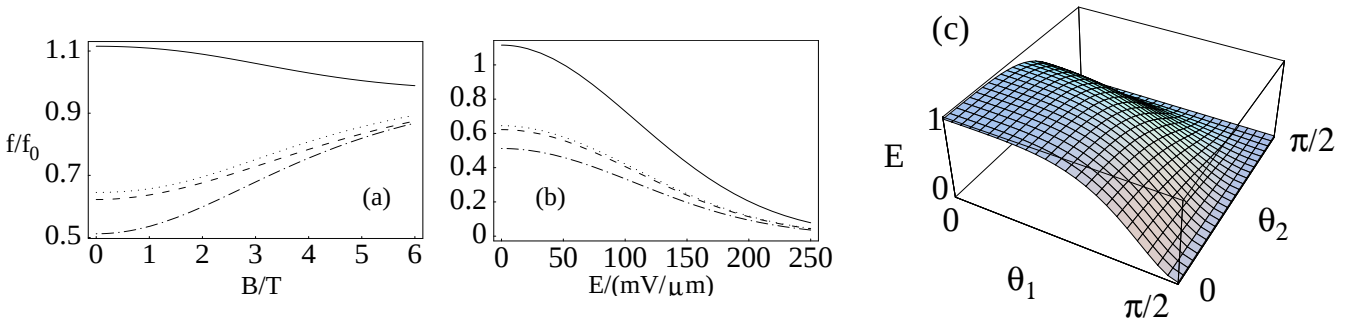


FIG. 33 (a) and (b): Oscillator strengths $f_{XX,X}$ for transitions between the biexciton states $|XX\rangle = |IJ\rangle$ and a single remaining exciton on one QD in units of f_0 as a function of (a) the magnetic field B (in Tesla) at $E = 0$ and (b) the electric field E (in mV/μm) at $B = 0$. The plotted HL energies E_{IJ} are E_{ss} (solid line), E_{st} (short-dashed), E_{ts} (dot-dashed), and E_{tt} (dotted), neglecting the Zeeman energy. The parameters were chosen for GaAs with $\eta = \omega_e/\omega_h = 1/2$. (c) Entanglement of formation E as a function of the emission angles θ_1 and θ_2 of the two photons. Only if both photons are emitted perpendicular to the plane ($\theta_1 = \theta_2 = 0$), the entanglement is maximal ($E = 1$). If at least one of them is emitted in-plane ($\theta_i = \pi/2$), then the two photons are not entangled ($E = 0$).

with $E^A_{IJ} \equiv \langle IJ|H_A|IJ\rangle$, can be calculated analytically within HL (Gywat *et al.*, 2002).

The exciton and biexciton recombination rates are determined by the oscillator strength f which is a measure for the coupling between the dipole moment of the exciton states and the electromagnetic field. For a transition between the $N+1$ and N exciton states $|N+1\rangle$ and $|N\rangle$, the oscillator strength is defined as

$$f_{N+1,N} = \frac{2|p_{N\mathbf{k}\lambda}|^2}{m_0\hbar\omega_{N+1,N}}, \tag{181}$$

where m_0 is the bare electron mass, $\hbar\omega_{N+1,N} = E_{N+1} - E_N$, and $p_{N\mathbf{k}\lambda} = \langle N+1|\mathbf{e}_{\mathbf{k}\lambda}\cdot\mathbf{p}|N\rangle$, where $\mathbf{e}_{\mathbf{k}\lambda}$ is the unit polarization vector for a photon with momentum $\mathbf{k}$ and helicity $\lambda = \pm 1$, and $\mathbf{p}$ is the electron momentum operator. The inter-band momentum matrix element for a cubic crystal symmetry is given by $M_{\sigma\lambda}(\theta) = \mathbf{e}_{\mathbf{k}\lambda}\cdot\mathbf{p}_{cv}(\sigma) = p_{cv}(\cos(\theta) - \sigma\lambda)/2 \equiv p_{cv}m_{\sigma\lambda}(\theta)$, where θ is the angle between $\mathbf{k}$ and the normal to the plane of the 2D electron system (assuming that the latter coincides with one of the main axes of the cubic crystal), and $E_p = 2p^2_{cv}/m_0$ (= 25.7 eV for GaAs).

The orbital momentum matrix element for the recombination of an exciton to the vacuum and for transitions from a biexciton state $|XX\rangle$ to a single exciton state $|X\rangle$ are given in (Gywat *et al.*, 2002); we give here our result for a transition between the HL biexciton states $|XX\rangle = |IJ\rangle$ with one exciton on each QD and a single exciton in the final state $|X\rangle$,

$$|\langle IJ|\mathbf{e}_{\mathbf{k}\lambda}\cdot\mathbf{p}|X\rangle| = 2M_{\sigma\lambda}(\theta)\sqrt{N_{IJ}}\left(C_{eh}\left[(-1)^{I+J} + S_eS_h\right] + S_{eh}\left[(-1)^J S_e + (-1)^I S_h\right]\right). \tag{182}$$

The corresponding oscillator strength f is plotted in Figs. 33a and 33b, in the approximation $\hbar\omega_{XX,X} \approx E_g$. The effect of an electric field is to spatially separate the electrons from the holes, which leads to a reduction of the oscillator strengths. Hence, the optical transition rate can be efficiently switched off and on, thus allowing the deterministic emission of one photon pair.

The HL biexciton state $|IJ\rangle$ can be written as a superposition of dark ($S_z = \pm 2$) and bright ($S_z = \pm 1$) exciton states. Upon recombination of the biexciton, the emitted photon states are (up to normalization)

$$|\chi_{IJ}\rangle \propto |+1,\theta_1\rangle|-1,\theta_2\rangle + (-1)^{I+J}|-1,\theta_1\rangle|+1,\theta_2\rangle, \tag{183}$$

where $|\sigma,\theta\rangle = N(\theta)(m_{\sigma,+1}(\theta)|\sigma_+\rangle + m_{\sigma,-1}(\theta)|\sigma_-\rangle)$ is the state of a photon emitted from the recombination of an electron with spin $S_z = \sigma/2 = \pm 1/2$ and a heavy hole with spin $S_z = 3\sigma/2$ in a direction which encloses the angle θ with the normal to the plane of the 2D electron and hole motion. The states of right and left circular polarization are denoted $|\sigma_\pm\rangle$. The entanglement between the two photon polarizations in the state Eq. (183) can be quantified by the von Neumann entropy E. For $|ss\rangle$ or $|tt\rangle$ and emission of the two photons enclosing an azimuthal angle $\phi = 0$ or π, we obtain

$$E = \log_2(1 + x_1x_2) - \frac{x_1x_2\log_2(x_1x_2)}{1 + x_1x_2}, \tag{184}$$

where $x_i = \cos^2(\theta_i)$. We plot $E(\theta_1, \theta_2)$ in Fig. 33c. Only the emission of both photons perpendicular to the plane ($\theta_1 = \theta_2 = 0$) results in maximal entanglement ($E = 1$). The two photons are not entangled ($E = 0$) if at least one of them is emitted in-plane ($\theta_i = \pi/2$). In order to observe the proposed effect, the relaxation rate to the biexciton ground state needs to be larger the biexciton recombination rate. The existence of such a regime is suggested by experiments with low excitation densities, see e.g. (Dekel *et al.*, 2000; Ohnesorge *et al.*, 1996). An upper limit for the pair production rate is then given by $(\tau_X + \tau_{XX})^{-1}$, where τ_X is the exciton and τ_{XX} the biexciton lifetime.

References

Aspect, A., J. Dalibard, and G. Roger, 1982, Phys. Rev. Lett. **49**, 1804.

Austing, D. G., T. Honda, K. Muraki, Y. Tokura, and S. Tarucha, 1998, Physica B **249-251**, 206.

Averin, D. V., 1998, Solid State Commun. **105**, 659.

Averin, D. V., and Y. V. Nazarov, 1992 (Plenum Press, New York), volume 294 of *NATO ASI Series B: Physics*.

Awschalom, D. D., and J. M. Kikkawa, 1999, Phys. Today **52**(6), 33.

Awschalom, D. D., D. Loss, and N. Samarth (eds.), 2002, *Semiconductor Spintronics and Quantum Computation*, Nanoscience and Technology (Springer, Berlin).

Bacon, D., K. R. Brown, and K. B. Whaley, 2001, Phys. Rev. Lett. **87**, 247902.

Bacon, D., J. Kempe, D. A. Lidar, and K. B. Whaley, 2000, Phys. Rev. Lett. **85**, 1758.

Ballentine, L. E., 1990, *Quantum Mechanics* (Prentice Hall, New Jersey), p. 352.

Banyai, L., Y. Z. Hu, M. Lindberg, and S. W. Koch, 1988, Phys. Rev. B .

Bao, J., A. V. Bragas, J. K. Furdyna, and R. Merlin, 2003, Nature Materials **2**, 175.

Barenco, A., C. H. Bennett, R. Cleve, D. P. DiVincenzo, N. Margolus, P. Shor, T. Sleator, J. Smolin, and H. Weinfurter, 1995a, Phys. Rev. A **52**, 3457.

Barenco, A., D. Deutsch, A. Ekert, and R. Josza, 1995b, Phys. Rev. Lett. **74**(20), 4083.

Barnes, C. H. W., J. M. Shilton, and A. M. Robinson, 2000, Phys. Rev. B **62**, 8410.

Bayer, M., P. Hawrylak, K. Hinzer, S. Fafard, M. Korkusinski, Z. R. Wasilewski, O. Stern, and A. Forchel, 2001, Science **291**, 451.

Beenakker, C. W. J., D. P. DiVincenzo, C. Emary, and M. Kindermann, 2004, Phys. Rev. Lett. **93**, 020501.

Bell, J. S., 1966, Rev. Mod. Phys. **38**, 447.

Bena, C., S. Vishveshwara, L. Balents, and M. P. A. Fisher, 2002, Phys. Rev. Lett. **89**, 037901.

Bennett, C. H., G. Brassard, S. Popescu, B. Schumacher, J. A. Smolin, and W. K. Wootters, 1996a, Phys. Rev. Lett. **76**, 722.

Bennett, C. H., and D. P. DiVincenzo, 2000, Nature **404**, 247.

Bennett, C. H., D. P. DiVincenzo, J. A. Smolin, and W. K. Wootters, 1996b, Phys. Rev. A **54**, 3824.

Benson, O., C. Santori, M. Pelton, and Y. Yamamoto, 2000, Phys. Rev. Lett. **84**, 2513.

Bertet, P., I. Chiorescu, G. Burkard, K. Semba, C. J. P. M. Harmans, D. P. DiVincenzo, and J. E. Mooij, 2004, Relaxation and dephasing in a persistent-current qubit, manuscript in preparation.

Biolatti, E., R. C. Iotti, P. Zanardi, and F. Rossi, 2000, Phys. Rev. Lett. **85**, 5647.

Bockrath, M., D. H. Cobden, J. Lu, A. G. Rinzler, R. E. Smalley, L. Balents, and P. L. McEuen, 1999, Nature **397**, 598.

Bonesteel, N. E., D. Stepanenko, and D. P. DiVincenzo, 2001, Phys. Rev. Lett. **87**, 207901.

Boschi, D., S. Branca, F. De Martini, L. Hardy, and S. Popescu, 1998, Phys. Rev. Lett. **80**, 1121.

Bouwmeester, D., J.-W. Pan, K. Mattle, M. Eibl, H. Weinfurter, and A. Zeilinger, 1997, Nature **390**, 575.

Braunstein, S., and H.-K. Lo (eds.), 2000, *Experimental Proposals for Quantum Computation*, volume 48 (Wiley, Berlin), Special Focus Issue of Fortschritte der Physik.

Brum, J. A., and P. Hawrylak, 1997, Superlattices and Microstructures **22**, 431.

Bryant, G. W., 1990, Phys. Rev. B **41**, 1243.

Bryant, G. W., 1993, Phys. Rev. B **48**, 8024.

Burkard, G., 2004, Circuit theory for decoherence in superconducting charge qubits, cond-mat/0408588.

Burkard, G., and F. Brito, 2004, Non-additivity of decoherence rates in superconducting qubits, cond-mat/0408001.

Burkard, G., D. P. DiVincenzo, P. Bertet, I. Chiorescu, , and J. E. Mooij, 2004a, Asymmetry and decoherence in a double-layer persistent-current qubit, cond-mat/0405273.

Burkard, G., H.-A. Engel, and D. Loss, 2000a, Fortsch. Physik **48**, 965, cond-mat/0004182.

Burkard, G., R. H. Koch, and D. P. DiVincenzo, 2004b, Phys. Rev. B **69**, 064503.

Burkard, G., and D. Loss, 2002, Phys. Rev. Lett. **88**, 047903.

Burkard, G., and D. Loss, 2003, Phys. Rev. Letters **91**, 087903.

Burkard, G., D. Loss, and D. P. DiVincenzo, 1999a, Phys. Rev. B **59**, 2070.

Burkard, G., D. Loss, D. P. DiVincenzo, and J. A. Smolin, 1999b, Phys. Rev. B **60**, 11404.

Burkard, G., D. Loss, and E. V. Sukhorukov, 2000b, Phys. Rev. B **61**, R16303, cond-mat/9906071.

Burkard, G., G. Seelig, and D. Loss, 2000c, Phys. Rev. B **62**, 2581.

Büttiker, M., 1990, Phys. Rev. Lett. **65**, 2901.

Büttiker, M., 1992, Phys. Rev. B **46**, 12485.

Caldeira, A. O., and A. J. Leggett, 1983, Ann. Phys. (N.Y.) **143**, 374.

Chen, P., C. Piermarocchi, and L. J. Sham, 2001, Phys. Rev. Lett. **87**, 067401.

Chiorescu, I., P. Bertet, K. Semba, Y. Nakamura, C. J. P. M. Harmans, and J. E. Mooij, 2004, Nature **431**, 159.
Chiorescu, I., Y. Nakamura, C. J. P. M. Harmans, and J. E. Mooij, 2003, Science **299**, 1869.
Choi, M.-S., C. Bruder, and D. Loss, 2000, Phys. Rev. B **62**, 13569.
Chtchelkatchev, N. M., G. Blatter, G. B. Lesovik, and T. Martin, 2002, Phys. Rev. B **66**, 161320.
Ciorga, M., A. S. Sachrajda, P. Hawrylak, C. Gould, P. Zawadzki, S. Jullian, Y. Feng, and Z. Wasilewski, 2000, Phys. Rev. B **61**, R16315.
Coish, W. A., and D. Loss, 2004, Hyperfine interaction in a quantum dot: Non-markovian electron spin dynamics, cond-mat/0405676 (to appear in Phys. Rev. B).
Darwin, C. G., 1930, Math. Proc. Cambridge Phil. Soc. **27**, 86.
Dekel, E., D. Gershoni, E. Ehrenfreund, J. M. Garcia, and P. M. Petroff, 2000, Phys. Rev. B **61**, 11009.
Devoret, M. H., 1997, in *Quantum fluctuations, lecture notes of the 1995 Les Houches summer school*, edited by S. Reynaud, E. Giacobino, and J. Zinn-Justin (Elsevier, The Netherlands), p. 351.
DiVincenzo, D. P., 1995, Phys. Rev. A **51**(2), 1015.
DiVincenzo, D. P., 1997, *Mesoscopic Electron Transport* (Kluwer Academic Publishers, Dordrecht), volume 345 of *NATO ASI Series E*, p. 657, cond-mat/9612126.
DiVincenzo, D. P., 2000, Fortschr. Phys. **48**, 771, quant-ph/0002077.
DiVincenzo, D. P., D. Bacon, J. Kempe, G. Burkard, and K. B. Whaley, 2000, Nature **408**, 339.
DiVincenzo, D. P., G. Burkard, D. Loss, and E. V. Sukhorukov, 1999, in *Quantum Mesoscopic Phenomena and Mesoscopic Devices in Microelectronics*, edited by I. O. Kulik and R. Ellialtioglu (Kluwer, Dordrecht), volume 559 of *NATO ASI Series C: Mathematical and Physical Sciences*, pp. 399–428.
DiVincenzo, D. P., and D. Loss, 1999, J. Mag. Magn. Matl. **200**, 202.
Dixon, D. C., K. R. Wald, P. L. McEuen, and M. R. Melloch, 1997, Phys. Rev. B **56**, 4743.
Dobers, M., K. v. Klitzing, J. Schneider, G. Weimann, and K. Ploog, 1988, Phys. Rev. Lett. **61**, 1650.
Edamatsu, K., G. Oohata, R. Shimizu, and T. Itoh, 2004, Nature **431**, 167.
Efros, A. L., and A. L. Efros, 1982, Sov. Phys. Semicond. **16**, 772.
Egger, R., and A. Gogolin, 1997, Phys. Rev. Lett. **79**, 5082.
Egues, J. C., G. Burkard, and D. Loss, 2002, Phys. Rev. Lett. **89**, 176401.
Einstein, A., B. Podolsky, and N. Rosen, 1935, Phys. Rev. **47**, 777.
Elzerman, J. M., R. Hanson, J. S. Greidanus, L. H. Willems van Beveren, S. De Franceschi, L. M. K. Vandersypen, S. Tarucha, and L. P. Kouwenhoven, 2003, Phys. Rev. B **67**, 161308.
Engel, H.-A., L. P. Kouwenhoven, D. Loss, and C. M. Marcus, 2004, Controlling spin qubits in quantum dots, cond-mat/0409294.
Engel, H.-A., and D. Loss, 2001, Phys. Rev. Lett. **86**, 4648.
Fafard, S., Z. R. Wasilewski, C. N. Allen, D. Picard, M. Spanner, J. P. McCaffrey, and P. G. Piva, 1999, Phys. Rev. B **59**, 15368.
Fazio, R., G. M. Palma, and J. Siewert, 1999, Phys. Rev. Lett. **83**, 5385.
Feynman, R. P., R. B. Leighton, and M. Sands, 1965, *The Feynman Lectures*, volume 3 (Addison-Wesley, Reading).
Fock, V., 1928, Z. Phys. **47**, 446.
Fradkin, E., 1991, *Field Theories of Condensed Matter Systems* (Addison-Wesley, Reading, MA).
Fricke, M., A. Lorke, J. P. Kotthaus, G. Medeiros-Ribeiro, and M. P. Petroff, 1996, Europhys. Lett. **36**, 197.
Gantmakher, V. F., and Y. B. Levinson, 1987, *Carrier scattering in metals and semiconductors* (North-Holland, Amsterdam), chapter 1.
Gerard, J.-M., and B. Gayral, 1999, in *QED phenomena and applications of microcavities and photonic crystals* (Springer-Verlag, Berlin).
Giuliani, G. F., and J. J. Quinn, 1982, Phys. Rev. B **26**, 4421.
Golovach, V. N., A. Khaetskii, and D. Loss, 2004, Phys. Rev. Lett. **93**, 016601.
Gupta, J. A., D. D. Awschalom, X. Peng, and A. P. Alivisatos, 1999, Phys. Rev. B **59**, R10421.
Gywat, O., G. Burkard, and D. Loss, 2002, Phys. Rev. B **65**, 205329.
Hanbury Brown, R., and R. Q. Twiss, 1956, Nature **177**, 27.
Hanson, R., J. M. Elzerman, L. H. W. van Beveren, L. M. K. Vandersypen, and L. P. Kouwenhoven, 2004, in *Controlling Decoherence*, 330. WE-Heraeus Seminar, Bad Honnef, Germany.
Hanson, R., B. Witkamp, L. M. K. Vandersypen, L. H. W. van Beveren, J. M. Elzerman, and L. P. Kouwenhoven, 2003, Phys. Rev. Lett. **91**, 196802.
Hawrylak, P., 1999, Phys. Rev. B **60**, 5597.
Hekking, F. W. J., L. I. Glazman, K. A. Matveev, and R. I. Shekhter, 1993, Phys. Rev. Lett. **70**, 4138.
Henny, M., S. Oberholzer, C. Strunk, T. Heinzel, K. Ensslin, M. Holland, and C. Schönenberger, 1999, Science **284**, 296.
Hu, X., and S. Das Sarma, 2000, Phys. Rev. A **61**, 062301.
Hu, X., and S. Das Sarma, 2001, Phys. Rev. A **64**, 042312.
Hu, X., and S. Das Sarma, 2003, Phys. Rev. A **68**, 052310.
Hu, X., and S. Das Sarma, 2004, Phys. Rev. B **69**, 115312.
Hu, Y. Z., S. W. Koch, M. Lindberg, N. Peyghambarian, E. L. Pollock, , and F. F. Abraham, 1990, Phys. Rev. Lett. **64**, 1805.
Imamoğlu, A., D. D. Awschalom, G. Burkard, D. P. DiVincenzo, D. Loss, M. Sherwin, and A. Small, 1999, Phys. Rev. Lett. **83**, 4204.
Imamura, H., H. Aoki, and P. A. Maksym, 1998, Phys. Rev. B **57**, R4257.
Imamura, H., P. A. Maksym, and H. Aoki, 1996, Phys. Rev. B **53**, 12613.

Imamura, H., P. A. Maksym, and H. Aoki, 1999, Phys. Rev. B **59**, 5817.
Ioffe, L. B., V. B. Geshkenbein, M. V. Feigel'man, A. L. Fauchère, and G. Blatter, 1999, Nature **398**, 679.
Ionicioiu, R., P. Zanardi, and F. Rossi, 2001, Phys. Rev. A **63**, 050101.
Ivchenko, E. L., A. A. Kiselev, and M. Willander, 1997, Solid State Comm. **102**, 375.
Johnston-Halperin, E., D. D. Awschalom, S. A. Crooker, A. L. Efros, M. Rosen, X. Peng, and A. P. Alivisatos, 2001, Phys. Rev. B **63**, 205309.
Kane, B. E., 1998, Nature **393**(6681), 133.
Kane, C., L. Balents, and M. Fisher, 1997, Phys. Rev. Lett. **79**, 5086.
Kavokin, K. V., 2001, Phys. Rev. B **64**, 075305.
Kawabata, S., 2001, J. Phys. Soc. Jpn. **70**, 1210.
Kempe, J., D. Bacon, D. A. Lidar, and K. B. Whaley, 2001, Phys. Rev. A **63**, 042307.
Kempe, J., and K. B. Whaley, 2002, Phys. Rev. A **65**, 052330.
Khaetskii, A. V., 2001, Physica E **10**, 27.
Khaetskii, A. V., D. Loss, and L. Glazman, 2002, Phys. Rev. Lett. **88**, 186802.
Khaetskii, A. V., and Y. V. Nazarov, 2000, Phys. Rev. B **61**, 12639.
Khaetskii, A. V., and Y. V. Nazarov, 2001, Phys. Rev. B **64**, 125316.
Khaneja, N., R. Brockett, and S. J. Glaser, 2001, Phys. Rev. A **63**, 032308.
Khlus, V. A., 1987, Zh. Eksp. Teor. Fiz. **93**, 2179.
Kikkawa, J. M., and D. D. Awschalom, 1998, Phys. Rev. Lett. **80**, 4313.
Kikkawa, J. M., I. P. Smorchkova, N. Samarth, and D. D. Awschalom, 1997, Science **277**, 1284.
Kiraz, A., S. Falth, C. Becher, B. Gayral, W. V. Schoenfeld, P. M. Petroff, L. Zhang, E. Hu, and A. Imamoglu, 2002, Phys. Rev. B **65**, 161303.
Kiselev, A. A., E. L. Ivchenko, and U. Rössler, 1998, Phys. Rev. B **58**, 16353.
Kitaev, A. Y., 2003, Annals Phys. **303**, 2, quant-ph/9707021.
Koch, R., J. Kirtley, J. Rozen, J. Sun, G. Keefe, F. Milliken, C. Tsuei, and D. DiVincenzo, 2003, Bull. Am. Phys. Soc. **48**, 367.
Koch, R., J. Kirtley, J. Rozen, J. Sun, G. Keefe, F. Milliken, C. Tsuei, and D. DiVincenzo, 2004, unpublished.
König, J., H. Schoeller, and G. Schön, 1997, Phys. Rev. Lett. **78**, 4482.
Kouwenhoven, L. P., D. G. Austing, and S. Tarucha, 2001, Rep. Prog. Phys. **64**, 701.
Kouwenhoven, L. P., C. M. Marcus, P. L. McEuen, S. Tarucha, R. M. Westervelt, and N. S. Wingreen, 1997a (Kluwer, Dordrecht), volume 345 of *NATO ASI Series E: Applied Sciences*, pp. 105–214.
Kouwenhoven, L. P., T. H. Oosterkamp, M. W. S. Danoesastro, M. Eto, D. G. Austing, and S. Taurcha, 1997b, Science **278**, 1788.
Kouwenhoven, L. P., G. Schön, and L. L. Sohn (eds.), 1997c, *Mesoscopic Electron Transport*, volume 345 of *NATO ASI Series E* (Kluwer Academic Publishers, Dordrecht).
Kwiat, P. G., K. Mattle, H. Weinfurter, A. Zeilinger, A. V. Sergienko, and Y. Shih, 1995, Phys. Rev. Lett. **75**, 4337.
Kwiat, P. G., E. Waks, A. G. White, I. Appelbaum, and P. H. Eberhard, 1999, Phys. Rev. A **60**, R773.
Kyriakidis, J., and S. J. Penney, 2004, Coherent rotations of a single spin-based qubit in a single quantum dot at fixed zeeman energy, cond-mat/0407139.
Kyriakidis, J., M. Pioro-Ladriere, M. Ciorga, A. S. Sachrajda, and P. Hawrylak, 2002, Phys. Rev. B **66**, 035320.
Ladd, T. D., J. R. Goldman, F. Yamaguchi, Y. Yamamoto, E. Abe, and K. M. Itoh, 2002, Phys. Rev. Lett. **89**, 017901.
Landauer, R., 1989, Physica D **38**, 226.
Landauer, R., 1991, Physics Today **44**(5), 23.
Landauer, R., 1996, Science **272**, 1914.
Leggett, A. J., S. Chakravarty, A. T. Dorsey, M. P. A. Fisher, A. Garg, and W. Zwerger, 1987, Rev. Mod. Phys. **59**, 1.
Lesovik, G., T. Martin, and G. Blatter, 2001, Eur. Phys. J. B **24**, 287.
Lesovik, G. B., 1989, Pis'ma Zh. Eksp. Teor. Fiz. **49**, 513.
Leung, D. W., 2004, Int. J. Quant. Inf. **2**, 33.
Levy, J., 2001, Phys. Rev. A **64**, 052306.
Levy, J., 2002, Phys. Rev. Lett. **89**, 147902.
Lidar, D. A., D. Bacon, and K. B. Whaley, 1999, Phys. Rev. Lett. **82**, 4556.
Lidar, D. A., I. L. Chuang, and K. B. Whaley, 1998, Phys. Rev. Lett. **81**, 2594.
Liu, R. C., B. Odom, Y. Yamamoto, and S. Tarucha, 1998, Nature **391**, 263.
Livermore, C., C. H. Crouch, R. M. Westervelt, K. L. Campman, and A. C. Gossard, 1996, Science **274**, 1332.
Loss, D., and D. P. DiVincenzo, 1998, Phys. Rev. A **57**(1), 120.
Loss, D., and P. Goldbart, 1992, Phys. Rev. B **45**, 13544.
Loss, D., and E. V. Sukhorukov, 2000, Phys. Rev. Lett. **84**, 1035.
Loudon, R., 1998, Phys. Rev. A **58**, 4904.
Luyken, R. J., A. Lorke, M. Haslinger, B. T. Miller, M. Fricke, J. P. Kotthaus, G. Medeiros-Ribiero, and P. M. Petroff, 1998, Physica E **2**, 704.
Madelung, O., 1978, *Introduction to Solid-State Theory* (Springer, Berlin), p. 110.
Mahan, G. D., 1993, *Many Particle Physics* (Plenum, New York), 2nd edition.
Maître, X., W. D. Oliver, and Y. Yamamoto, 2000, Physica E **6**, 301.
Makhlin, Y., 2002, Quant. Info. Proc. **1**, 243, quant-ph/0002045.

Makhlin, Y., G. Schön, and A. Shnirman, 1999, Nature **398**, 305.
Makhlin, Y., G. Schön, and A. Shnirman, 2001, Rev. Mod. Phys **73**, 357.
Makhlin, Y., and A. Shnirman, 2004, Phys. Rev. Lett. **92**, 178301.
Martin, T., and R. Landauer, 1992, Phys. Rev. B **45**, 1742.
Martinis, J. M., S. Nam, J. Aumentado, , K. M. Lang, and C. Urbina, 2003, Phys. Rev. B **67**, 094510.
Martinis, J. M., S. Nam, J. Aumentado, and C. Urbina, 2002, Phys. Rev. Lett. **89**, 117901.
Mattis, D. C., 1988, *The Theory of Magnetism I* (Springer, New York), volume 17 of *Springer Series in Solid-State Sciences*, chapter 4.5.
Mattle, K., H. Weinfurter, P. G. Kwiat, and A. Zeilinger, 1996, Phys. Rev. Lett. **76**, 4656.
Meier, F., J. Levy, and D. Loss, 2003a, Phys. Rev. B **68**, 134417.
Meier, F., J. Levy, and D. Loss, 2003b, Phys. Rev. Lett. **90**, 047901.
Meier, F., and D. Loss, 2004, Reduced visibility of rabi oscillations in superconducting qubits, cond-mat/0408594.
Mermin, N. D., 1993, Rev. Mod. Phys. **65**, 803.
Mermin, N. D., 2003, Am. J. Phys. **71**, 23, quant-ph/0207118.
Mooij, J. E., T. P. Orlando, L. Levitov, L. Tian, C. H. van der Wal, and S. Lloyd, 1999, Science **285**, 1036.
Moreau, E., I. Robert, L. Manin, V. Thierry-Mieg, J. M. Gerard, and I. Abram, 2001, Phys. Rev. Lett. **87**, 183601.
Nair, S. V., and T. Takagahara, 1996, Phys. Rev. B **55**, 5153.
Nakamura, Y., Y. A. Pashkin, and J. S. Tsai, 1999, Nature **398**, 786.
Nielsen, M. A., 2003, Phys. Lett. A **308**, 96.
Nielsen, M. A., and I. L. Chuang, 2000, *Quantum Computation and Quantum Information* (Cambridge University Press, Cambridge).
Oh, J. H., K. J. Chang, G. Ihm, and S. J. Lee, 1996, Phys. Rev. B **53**, R13264.
Ohnesorge, B., M. Albrecht, J. Oshinowo, A. Forchel, and Y. Arakawa, 1996, Phys. Rev. B **54**, 11532.
Oliver, W. D., J. Kim, R. C. Liu, and Y. Yamamoto, 1999, Science **284**, 299.
Oliver, W. D., F. Yamaguchi, and Y. Yamamoto, 2002, Phys. Rev. Lett. **88**, 037901.
Orlando, T. P., J. E. Mooij, L. Tian, C. H. van der Wal, L. Levitov, S. Lloyd, and J. J. Mazo, 1999, Phys. Rev. B **60**, 15398.
Pashkin, A., T. Yamamoto, O. Astafiev, Y. Nakamura, D. V. Averin, and J. S. Tsai, 2003, Nature **421**, 823.
Peikari, B., 1974, *Fundamentals of Network Analysis and Synthesis* (Prentice-Hall, Englewood Cliffs, NJ).
Pellizzari, T., S. A. Gardiner, J. I. Cirac, and P. Zoller, 1995, Phys. Rev. Lett. **75**, 3788.
Piermarocchi, C., P. Chen, L. J. Sham, and D. G. Steel, 2002, Phys. Rev. Lett. **89**, 167402.
Platzman, P. M., and M. I. Dykman, 1999, Science **284**, 1967.
Popescu, A. E., and R. Ionicioiu, 2004, Phys. Rev. B **69**, 245422.
Preskill, J., 1998a, *Fault-tolerant quantum computation* (World Scientific, Singapore), pp. 213–269.
Preskill, J., 1998b, Proc. R. Soc. London Ser. A **454**, 385.
Prinz, G. A., 1998, Science **282**, 1660.
Privman, V., I. D. Vagner, and G. Kventsel, 1998, Phys. Lett. A **239**, 141.
Raussendorf, R., and H. J. Briegel, 2001, Phys. Rev. Lett. **86**, 5188.
Recher, P., and D. Loss, 2002a, Journal of Superconductivity and Novel Magnetism **15**, 49, cond-mat/0202102.
Recher, P., and D. Loss, 2002b, Phys. Rev. B **65**, 165327.
Recher, P., and D. Loss, 2003, Phys. Rev. Lett. **91**, 267003.
Recher, P., E. V. Sukhorukov, and D. Loss, 2001, Phys. Rev. B **63**, 165314.
Redfield, A. G., 1957, IBM J. Res. Develop. **1**, 19.
Requist, R., J. Schliemann, A. G. Abanov, and D. Loss, 2004, Double occupancy errors in quantum computing operations: Corrections to adiabaticity, cond-mat/0409096.
Samuelsson, P., E. V. Sukhorukov, and M. Buttiker, 2003, Phys. Rev. Lett. **91**, 157002.
Samuelsson, P., E. V. Sukhorukov, and M. Buttiker, 2004a, Phys. Rev. B **70**, 115330.
Samuelsson, P., E. V. Sukhorukov, and M. Buttiker, 2004b, Phys. Rev. Lett. **92**, 026805.
Sanders, G. D., K. W. Kim, and W. C. Holton, 1999, Phys. Rev. A **59**, 1098.
Santori, C., G. S. Solomon, M. Pelton, and Y. Yamamoto, 2002, Phys. Rev. B **65**, 073310.
Saraga, D. S., B. L. Altshuler, D. Loss, and R. M. Westervelt, 2004, Phys. Rev. Lett. **92**, 246803.
Saraga, D. S., and D. Loss, 2003, Phys. Rev. Lett. **90**, 166803.
Schedelbeck, G., W. Wegscheider, M. Bichler, and G. Abstreiter, 1997, Science **278**, 1792.
Schliemann, J., J. I. Cirac, M. Kus, M. Lewenstein, and D. Loss, 2001a, Phys. Rev. A **64**, 022303.
Schliemann, J., D. Loss, and A. H. MacDonald, 2001b, Phys. Rev. B **63**, 085311.
Schrieffer, J. R., 1964, *Theory of Superconductivity* (Benjamin/Cummings, New York).
Schrieffer, J. R., and P. A. Wolff, 1966, Phys. Rev. **149**, 491.
Schuch, N., and J. Siewert, 2003, Phys. Rev. A **67**, 032301.
Schulz, H. J., 1990, Phys. Rev. Lett. **64**, 2831.
Seelig, G., 1999, *Spin interactions in tunneling-coupled vertical quantum dots*, Diploma thesis, University of Basel.
Shnirman, A., G. Schön, and Z. Hermon, 1997, Phys. Rev. Lett. **79**, 2371.
Simmonds, R. W., K. M. Lang, D. A. Hite, S. Nam, D. P. Pappas, and J. M. Martinis, 2004, Phys. Rev. Lett. **93**, 077003.
de Sousa, R., X. Hu, and S. Das Sarma, 2001, Phys. Rev. A **64**, 042307.
Taddei, F., and R. Fazio, 2002, Phys. Rev. B **65**, 075317.
Takagahara, T., 1989, Phys. Rev. B **39**, 10206.

Tanamoto, T., 2000, Phys. Rev. A **61**, 022305.
Tarucha, S., D. G. Austing, T. Honda, R. J. van der Hage, and L. P. Kouwenhoven, 1996, Phys. Rev. Lett. **77**(17), 3613.
Tian, L., L. S. Levitov, J. E. Mooij, T. P. Orlando, C. H. van der Wal, and S. Lloyd, 2000, *Quantum Mesoscopic Phenomena and Mesoscopic Devices in Microelectronics* (Kluwer, Dordrecht), pp. 429–438, cond-mat/9910062.
Tian, L., S. Lloyd, and T. P. Orlando, 2002, Phys. Rev. B **65**, 144516.
Tokura, Y., D. G. Austing, and S. Tarucha, 1999, J. Phys. C **11**, 6023.
Topinka, M. A., B. J. LeRoy, S. E. J. Shaw, E. J. Heller, R. M. Westervelt, K. D. Maranowski, and A. C. Gossard, 2000, Science **289**, 2323.
Topinka, M. A., B. J. Leroy, R. M. Westervelt, S. E. J. Shaw, R. Fleischmann, E. J. Heller, K. D. Maranowski, and A. C. Gossard, 2001, Nature **410**, 183.
Torrès, J., and T. Martin, 1999, Eur. Phys. J. B **12**, 319.
Troiani, F., U. Hohenester, and E. Molinari, 2000, Phys. Rev. B **62**, R2263.
Tsvelik, A. M., 2003, *Quantum Field Theory in Condensed Matter Physics* (Cambridge University Press), 2nd edition.
Vala, J., and K. B. Whaley, 2002, Phys. Rev. A **66**, 022304.
Viola, L., E. Knill, and S. Lloyd, 2000, Dynamical generation of noiseless quantum subsystems, quant-ph/0002072.
Vion, D., A. Aassime, A. Cottet, P. Joyez, H. Pothier, C. Urbina, D. Esteve, and M. H. Devoret, 2002, Science **296**, 886.
Vorojtsov, S., E. R. Mucciolo, and H. U. Baranger, 2004, Phys. Rev. B **69**, 115329.
Vrijen, R., E. Yablonovitch, K. Wang, H. W. Jiang, A. Balandin, V. Roychowdhury, T. Mor, and D. DiVincenzo, 2000, Phys. Rev. A **62**, 012306.
Wagner, M., U. Merkt, and A. V. Chaplik, 1992, Phys. Rev. B **45**, 1951.
van der Wal, C. H., A. C. J. ter Har, F. K. Wilhelm, R. N. Schouten, C. J. P. M. Harmans, T. P. Orlando, S. Lloyd, and J. E. Mooij, 2000, Science **290**, 773.
van der Wal, C. H., F. K. Wilhelm, C. J. P. M. Harmans, and J. E. Mooij, 2003, Eur. Phys. J. B **31**, 111.
Wallraff, A., D. I. Schuster, A. Blais, L. Frunzio, R.-S. Huang, J. Majer, S. Kumar, S. M. Girvin, and R. J. Schoelkopf, 2004, Nature **431**, 162.
Waugh, F. R., M. J. Berry, D. J. Mar, R. M. Westervelt, K. L. Campman, and A. C. Gossard, 1995, Phys. Rev. Lett. **75**(4), 705.
Weinstein, Y. S., and C. S. Hellberg, 2004, Energetic suppression of decoherence in exchange-only quantum computation, quant-ph/0408037.
Weiss, U., 1999, *Quantum Dissipative Systems* (World Scientific, Singapore), 2nd edition.
Werner, M. J., and P. D. Drummond, 1991, Phys. Rev. A **43**, 6414.
Werner, R. F., 1989, Phys. Rev. A **40**, 4277.
van der Wiel, W. G., S. D. Franceschi, J. M. Elzerman, T. Fujisawa, S. Tarucha, and L. P. Kouwenhoven, 2003, Rev. Mod. Phys. **75**, 1.
Wilhelm, F. K., M. J. Storcz, C. H. van der Wal, C. J. P. M. Harmans, and J. E. Mooij, 2003, Adv. Solid State Phys. **43**, 763.
Wojs, A., P. Hawrylak, S. Fafard, and L. Jacak, 1996, Phys. Rev. B **54**, 5604.
Wu, L.-A., and D. A. Lidar, 2002a, Phys. Rev. A **65**, 042318.
Wu, L.-A., and D. A. Lidar, 2002b, Phys. Rev. A **66**, 062314.
Wu, L.-A., D. A. Lidar, and M. Friesen, 2004, Phys. Rev. Lett. **93**, 030501.
Yang, S.-R. E., J. Schliemann, and A. H. MacDonald, 2002, Phys. Rev. B **66**, 153302.
You, J. Q., C.-H. Lam, and H. Z. Zheng, 2001, Phys. Rev. B **63**, 180501(R).
Yurke, B., 1987, J. Opt. Soc. Am. B **4**, 1557.
Yurke, B., and J. S. Denker, 1994, Phys. Rev. A **29**, 1419.
Zanardi, P., and M. Rasetti, 1997, Mod. Phys. Lett. B **11**, 1085.
Zanardi, P., and F. Rossi, 1998, Phys. Rev. Lett. **81**, 4752.
Zumbühl, D. M., C. M. Marcus, M. P. Hanson, and A. C. Gossard, 2004, Cotunneling spectroscopy in few-electron quantum dots, cond-mat/0408276.